

UC San Diego

UC San Diego Electronic Theses and Dissertations

Title

Mathematical Modeling and Computational Methods for Electrostatic Interactions with Application to Biological Molecules

Permalink

<https://escholarship.org/uc/item/6b0398p9>

Author

Wen, Jiayi

Publication Date

2015

Peer reviewed|Thesis/dissertation

UNIVERSITY OF CALIFORNIA, SAN DIEGO

**Mathematical Modeling and Computational Methods for Electrostatic
Interactions with Application to Biological Molecules**

A dissertation submitted in partial satisfaction of the
requirements for the degree
Doctor of Philosophy

in

Mathematics

by

Jiayi Wen

Committee in charge:

Professor Bo Li, Chair
Professor Chung-Kuan Cheng
Professor Li-Tien Cheng
Professor Philip Gill
Professor Xun Jia

2015

Copyright
Jiayi Wen, 2015
All rights reserved.

The dissertation of Jiayi Wen is approved, and it is acceptable in quality and form for publication on microfilm and electronically:

Chair

University of California, San Diego

2015

TABLE OF CONTENTS

Signature Page	iii
Table of Contents	iv
List of Figures	vi
List of Tables	viii
Acknowledgements	ix
Vita	x
Abstract of the Dissertation	xi
Chapter 1	Introduction	1
	1.1 Background	2
	1.2 Models and Methods	4
	1.2.1 Monte Carlo simulations	4
	1.2.2 The Poisson–Boltzmann theory	5
	1.2.3 Phase-field models	8
	1.3 Summary of the Dissertation Work	9
	1.3.1 Monte Carlo simulations of ionic size effects	10
	1.3.2 Theory and computation of electrostatics with ionic concentration dependent dielectrics	11
	1.3.3 Phase-field modeling and computation of charged molecules	12
	1.4 Outline for the Rest of Dissertation	13
Chapter 2	Theory and Computation of Ionic Size Effects	14
	2.1 Introduction	14
	2.2 Mean-Field Theory and Method	17
	2.2.1 A mean-field theory with nonuniform size effects	18
	2.2.2 A constrained optimization method	20
	2.3 Monte Carlo Simulations	23
	2.4 Results and Discussions	26
	2.4.1 Crucial factors in the competition between coun- terions	28
	2.4.2 Systems with both counterions and coions	33
	2.5 Remarks	36

Chapter 3	Mean-Field Theory and Computation of Electrostatics with Ionic Concentration Dependent Dielectrics	39
3.1	Introduction	39
3.2	First Variations and Generalized Boltzmann Distributions	43
3.2.1	First variations	44
3.2.2	Generalized Boltzmann distributions	48
3.3	Second Variations	48
3.4	Non-Convexity of the Free-Energy Functional	53
3.5	Numerical Study of a Model System	57
3.5.1	Comparison of different dielectric relations: counterion depletion	59
3.5.2	Effect of surface charges and bulk concentrations: non-monotonicity of counterion concentrations . .	62
3.6	Remarks	64
Chapter 4	Phase-Field Model with Poisson–Boltzmann Electrostatics . .	67
4.1	Introduction	67
4.2	A Variational Formulation	71
4.3	Numerical Methods	76
4.3.1	Discretization	76
4.3.2	Algorithm	78
4.3.3	Convergence test	79
4.4	Remarks	81
Chapter 5	Conclusions and Discussions	84
5.1	Summary	84
5.2	Discussion and Future Work	85
Bibliography	88

LIST OF FIGURES

Figure 1.1:	A typical charged molecular system in aqueous solvent.	2
Figure 1.2:	Computer simulated different conformations of the protein BphC. The color indicates curvature.	3
Figure 1.3:	The phase-field function.	9
Figure 1.4:	The dielectric coefficient for NaCl solution.	11
Figure 2.1:	Typical Monte Carlo simulations of ions surrounding a highly charged macroion.	27
Figure 2.2:	The histograms of radial particle density functions for three species of counterions in Group 1: $\alpha_{+1} : \alpha_{+2} : \alpha_{+3} = 1 : 3.5 :$ 1.9	30
Figure 2.3:	The histograms of radial particle density functions for three species of counterions in Group 2: $\alpha_{+1} : \alpha_{+2} : \alpha_{+3} = 1.4 : 1 :$ 2.4	30
Figure 2.4:	The histograms of radial particle density functions for three species of counterions in Group 2: $\alpha_{+1} : \alpha_{+2} : \alpha_{+3} = 2.7 : 1.6 :$ 1	30
Figure 2.5:	Mean-field predictions of concentrations of counterions in Group 1: $\alpha_{+1} : \alpha_{+2} : \alpha_{+3} = 1 : 3.5 : 1.9$	31
Figure 2.6:	The layering structure of ionic densities is very sensitive to the variation of the ionic radius of one ionic species.	32
Figure 2.7:	Results of varying the ionic radii of the three species with a common factor.	33
Figure 2.8:	Counterion and coion distributions from MC simulations. Top: monovalent coions. Bottom: divalent coions.	34
Figure 2.9:	Counterion and coion concentrations from numerical computa- tions based on the mean-field theory with the ionic size effect. Top: monovalent coions. Bottom: divalent coions.	35
Figure 2.10:	MC simulations of the total charge distribution for the system with monovalent coions (marked -1) and that with divalent coions (marked -2).	36
Figure 3.1:	A schematic view of an ionic solution. The solvent occupies the grey region Ω	42
Figure 3.2:	Top: $G(c)$ vs. c for different values of ϕ and $ \nabla\phi $. Bottom: Zeros of $G(c)$ vs. ϕ and $ \nabla\phi $. The three dots on the verticle line indicate the three zeros of $G(c)$	55
Figure 3.3:	Graph of the function $F[c]$ defined in (3.24).	56
Figure 3.4:	Left: Graph of the function $\varepsilon = \varepsilon(c)$ defined in (3.26). Right: Graph of the function $F[c]$ defined in (3.27).	58

Figure 3.5:	The concentrations vs. radial distance to the charged surface for System I with the surface charge density $\sigma = -0.005 \text{ e}/\text{\AA}^2$. Inset: the graph of function $\varepsilon_i(\bar{c}(r))$ for $i = 1, \dots, 4$	61
Figure 3.6:	The concentrations vs. radial distance to the charged surface for System I with the surface charge density $\sigma = -0.012 \text{ e}/\text{\AA}^2$. Inset: the graph of function $\varepsilon_i(\bar{c}(r))$ for $i = 1, \dots, 4$	61
Figure 3.7:	System I with $\varepsilon = \varepsilon_4(\bar{c})$. Left: The ionic concentrations vs. the radial distance to the charged surface. Right: The electrostatic potentials vs. the radial distance to the charged surface for different values of the surface charge density.	62
Figure 3.8:	Left: The Counterion concentration at the charged surface and the maximum value of counterion concentration vs. the surface charge density. Right: The electrostatic potential at the charged surface vs. the surface charge density.	63
Figure 3.9:	Left: Concentrations vs. radial distance to the charged surface with different ionic concentrations. Right: The counterion concentration at the charged surface and the maximal value of counterion concentration vs. bulk ionic concentration.	64
Figure 3.10:	Ionic concentrations vs. radial distance to the charge surface with different values of surface charge density σ . Upper left: $\sigma = -0.005\text{e}/\text{\AA}^2$. Upper right: $\sigma = -0.01\text{e}/\text{\AA}^2$. Lower left: $\sigma = -0.015\text{e}/\text{\AA}^2$. Lower right: $\sigma = -0.02\text{e}/\text{\AA}^2$	65
Figure 4.1:	Schematic view of a solvation system. Left: a full atomistic model. Right: an implicit-solvent model. The solute-solvent interface Γ separates the solute region Ω_m from the solvent region Ω_w	68
Figure 4.2:	A phase-field version of the dielectric coefficient (relative permittivity $\varepsilon(\phi)/\varepsilon_0$), which takes value ε_w at solvent region and ε_m at solute region.	74
Figure 4.3:	The interface of $\phi = 0.5$ is converging to the sharp interface when $Q = 0$	81
Figure 4.4:	The interface of $\phi = 0.5$ is converging to the sharp interface when $Q = 0.1$	82
Figure 4.5:	The interface of $\phi = 0.5$ is converging to the sharp interface when $Q = 0.5$	82
Figure 4.6:	The radius of ion is decreasing when it carries larger charge. Here $\xi = 0.5$	83

LIST OF TABLES

Table 4.1:	The comparison between the diffuse interface model and sharp interface model for a solute-solvent system with a single one atom centered at the origin, where $Q = 0$ and $\kappa = 0.01$	80
Table 4.2:	The comparison between the diffuse interface model and sharp interface model for a solute-solvent system with a single one atom centered at the origin, where $Q = 0.1$ and $\kappa = 0.01$	80
Table 4.3:	The comparison between the diffuse interface model and sharp interface model for a solute-solvent system with a single one atom centered at the origin, where $Q = 0.5$ and $\kappa = 0.01$	81

ACKNOWLEDGEMENTS

Chapter 2, in part is taken from the material as it appears in *Competitive adsorption and ordered packing of counterions near highly charged surfaces: From mean-field theory to Monte Carlo simulations* by J. Wen, S. Zhou, Z. Xu, and B. Li, published in Physical Review E 85 (4), 041406, 2011.

Chapter 3, in part is taken from the material as it appears in *Mean-field Theory and Computation of Electrostatics with Ionic concentration Dependent Dielectrics* by B. Li, J. Wen, and S. Zhou, accepted for publication in Communications in Mathematical Sciences.

Chapter 4, in part, is taken from material as it appears in *A Self-Consistent Diffused-Interface Approach to Implicit Solvation of Charged Molecules with Poisson-Boltzmann Electrostatics* by J. Wen, Y. Zhao, H. Sun, and B. Li, which is being prepared for submission.

VITA

2010	B. S. in Mathematics, Fudan University, Shanghai, China
2012	C. Phil in Mathematics, University of California, San Diego
2011-2014	Graduate Teaching Assistant, University of California, San Diego
2011-2015	Graduate Reserach Assistant, University of California, San Diego
2014-2015	Associate Instructor, University of California, San Diego
2015	Ph. D in Mathematics, University of California, San Diego

PUBLICATIONS

Jiayi Wen, Shenggao Zhou, Zhenli Xu, Bo Li, “Competitive adsorption and ordered packing of counterions near highly charged surfaces: From mean-field theory to Monte Carlo simulations”, *Phys. Rev. E* 85, 041406, 2012.

Bo Li, Jiayi Wen, Shenggao Zhou, “Mean-field Theory and Computation of Electrostatics with Ionic concentration Dependent Dielectrics”, *Comm. Math. Sci.*, 2015 (Accepted).

AWARDS

UC Office of President Graduate Fellowship in Computational Science (2015)

UCSD Chancellors Interdisciplinary Collaboratories Award (2012, 2013)

ABSTRACT OF THE DISSERTATION

**Mathematical Modeling and Computational Methods for Electrostatic
Interactions with Application to Biological Molecules**

by

Jiayi Wen

Doctor of Philosophy in Mathematics

University of California, San Diego, 2015

Professor Bo Li, Chair

In this dissertation, I combine physical modeling, mathematical analysis, and numerical computation to study several problems concerning electrostatic interactions in biological molecular systems. Biomolecules, such as DNAs and proteins, are highly charged. They interact with each other and with the mobile ions and the polarized solvent to generate strong forces that affect crucially many molecular processes, such as molecular conformational changes, recognition, and self-assembly. My goal is to develop rigorous theories and efficient computational tools to understand some of the principles and mechanisms underlying such complicated interactions.

Specifically, I study three closely related problems. The first one is the

effect of ionic sizes that has been experimentally observed to be significant. Using a size-modified mean-field model and extensive Monte Carlo simulations, I capture details of the competitive adsorption of counterions of multiple species to charged surfaces. The simulations confirm the crucial role of ionic valence-to-volume ratios that had been predicted by the mean-field theory.

The second problem is how the ionic concentration dependent dielectric coefficient can affect the equilibrium properties of charged system. I construct a variational model, derive rigorously the first and second variations of the free-energy functional, and prove that the functional is nonconvex. Numerical studies reveal several important features that cannot be modeled with a constant dielectric coefficient.

Finally, I study a general problem of the solvation of charged molecules, aiming at understanding how electrostatic interactions contribute to the shape of underlying molecules. I develop a phase-field implicit-solvent approach to minimize a free-energy functional that couples the interfacial energy, van der Waals solute-solvent interaction energy, and electrostatic energy. I also design numerical methods to implement this approach.

A common theme of my dissertation work is the variational approach. Many physical effects such as ionic size effects, solvent entropy, concentration dependent dielectric response can be incorporated into a mean-field free-energy functional of ionic concentrations coupled with the Poisson equation for electrostatics. The techniques of analysis developed in this work may help improve the understanding of the underlying physical properties of charged systems and provide new ways of studying analytically and numerically other problems in the calculus of variations.

Chapter 1

Introduction

Electrostatic interactions play an important role in many complex charged systems, such as biological molecules, soft matter material, nanofluids, and electrochemical devices [And95, BKN⁺05, DM90, FBM02, FPP⁺10, Lev02, McC09, SH90b]. The subject of this dissertation is to develop mathematical theories and computational methods to understand such interactions, particularly in charged biological molecular systems. The main contributions of my dissertation work include:

- (1) Theoretical studies of mean-field variational models of ionic solution and that of molecular surfaces with the Poisson–Boltzmann electrostatics;
- (2) Design and implementation of the corresponding computational algorithms, and conduct extensive Monte Carlo simulations and numerical solutions of partial differential equations for charge-charge interactions;
- (3) Discovery of various interesting properties of charged molecules, validate some experimental results, and clarify some confusion in literature.

It is hoped that the mathematical and numerical methods developed here can be used to solve other problems in the calculus of variations; and that the physical properties discovered here, relative new to the community, are of interest in application and for future investigations.

In this introductory chapter, I will first describe the background of electrostatic interactions in biological molecular systems, and indicate the importance of and challenges in studying such interactions. I will then describe the main theories and methods that have been used to study some of the electrostatics problems and

that are related to my dissertation work. In particular, I will describe the classical Poisson–Boltzmann theory, its limitations, and its modifications. Finally, I will present my main research results and describe their significance.

1.1 Background

A biological molecule such as a DNA or protein consists of many charged atoms. (When two neutral atoms share an electron, each of them is then slightly positively charged.) Such charged molecules induce an electric field that polarizes the surrounding solvent (water or salted water) by deforming the structure of each water molecule. In addition to charged molecules, there are often mobile ions, such as Sodium (Na^+) and Chlorine (Cl^-) in the solvent. See Figure 1.1 for a schematic description of a charged molecular system. In the figure, the white region is a charged molecular region and the blue region is the solvent region. Small circles represent mobile ions with + and - indicating ions of positive charge or negative charge, respectively.

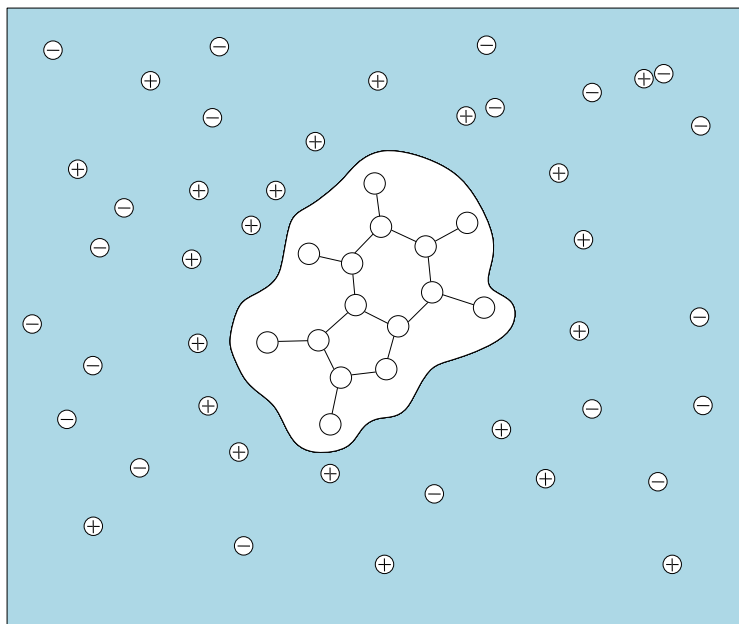


Figure 1.1: A typical charged molecular system in aqueous solvent.

The electrostatic interactions among the charged molecules, mobile ions, and polarized solvent, together with covalent bonding and dispersive van der Waals forces that are short-ranged repulsion and long-ranged attraction, generate strong molecular forces that determine the molecular conformations and dynamics, and further cellular functions. Examples of electrostatics mediated and controlled biological molecular processes include: protein folding [Dil90, LO06] where a misfold can lead a fatal disease; flow of ions through ion channels [Hil01] that maintain our immunity; protein-ligand binding [ACI⁺09, CWS⁺09, SWC⁺09] and protein association [SNH00, McC09] that are the key of drug effectiveness. Figure 1.2 shows a recent computational result of the two-domain protein BphC, indicating a strong charge effect [WCC⁺12]. Without charges (left of Figure 1.2), a dry region (a region of no water molecules) exists near the connection of the two domains. But it is gone after charges are added numerically (right of Figure 1.2).

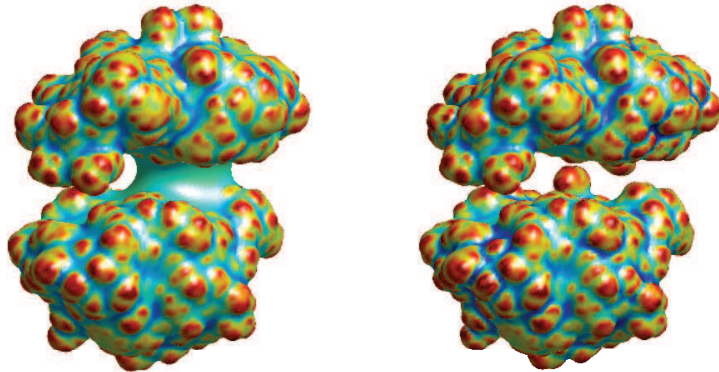


Figure 1.2: Computer simulated different conformations of the protein BphC. The color indicates curvature.

Accurate and efficient modeling and computations of electrostatic interactions in a real biological system have been challenging due to the inhomogeneity, complicated geometry, multiple scales, and the nature of many-body interaction of an underlying charged system. In recent years, there have been growing needs and interest in developing rigorous mathematical theories and efficient computational methods to study such molecular systems. My dissertation concerns mathematically problems in the calculus of variations, such as the convexity of a free-energy

functional and its first and second variations. Some of the problems involve geometrical flows. My work also concerns numerical computations, including Monte Carlo simulations and numerical solutions to partial differential equations.

1.2 Models and Methods

There are in general two types of modeling approaches to understanding electrostatic interactions in charged systems. The first one is a particle-like method, such as molecular dynamics (MD) simulations, Brownian dynamics simulations, and Monte Carlo (MC) simulations [FS02]. In such an approach, each particle (such as an atom or ion) in the system is treated as an explicit object. Simulations are usually very accurate but time consuming due to the large number of degrees of freedom. The second one is a field-like method, e.g. a mean-field model [And95] that is often in the form of differential equations. By replacing all interactions to any object in the system with an average or effective interaction, a mean-field method can efficiently provide some insight into the phenomena of the system.

In this dissertation, I will focus on the development of mean-field methods, mainly the Poisson–Boltzmann theory, and the application of Monte Carlo simulations to study the properties of charged systems.

1.2.1 Monte Carlo simulations

Monte Carlo (MC) simulations are very useful to describe the equilibrium properties of a system with many degrees of freedom. In such simulations, many different states of an underlying system are randomly sampled to provide statistical quantities, such as the averages or probability densities. MC simulations have many applications in computational physics, chemistry, and biology, particularly for strongly coupled solids, charged molecular system, and cellular structures.

The Metropolis–Hastings algorithm

In this dissertation, I use the Metropolis–Hastings algorithm to study the electrostatic interaction and ionic concentrations in charged system. The Metropolis–

Hasting algorithm is a Markov Chain Monte Carlo method. Here I briefly describe how to apply Metropolis–Hasting algorithm to study a many-particle system.

Consider a system with N particles. Denote the location of i th particle by \mathbf{x}_i , where $i = 1, \dots, N$. Let $U = U(\mathbf{x}_1, \dots, \mathbf{x}_N)$ be an interaction potential of all the particles. It is often defined as the sum of all pairwise interaction energies among all the particles. MC simulations consist of a sequence of single-particle moves with some boundary conditions (for example, periodical, or reflection, or sink). The algorithm of each move is as follows:

Step 1. Select randomly an individual particle and move it randomly.

Step 2. Compute the U_{new} , the potential of the system, where the selected particle is located at the new position.

Step 3. If $U_{new} < U_{old}$ (where U_{old} is the potential before the particle was moved), accept the move; else compute $s = e^{-\beta\Delta U}$ where β is a constant (often inversely proportional to temperature) of the system and $\Delta U = U_{new} - U_{old}$, then generate a random number t uniformly from $[0, 1]$. If $s > t$, accept the move, otherwise reject it.

After many moves, the system is considered to have reached an equilibrium when the accept rate is small enough. Then one can start to compute the ensemble average and study the property of the system. The algorithm is usually very time consuming. More details about the MC acceleration are discussed in Chapter 2.

1.2.2 The Poisson–Boltzmann theory

In recent years, many theoretical studies of electrostatic interactions have based on the classical, mean-field, Poisson–Boltzmann (PB) theory [Cha13, DH23, Fix79, Gou10]. Such a theory has been successfully applied in biomolecular modeling and colloidal science [And95, DM90, GT08, LZHM08, SH90b]. In the classical PB theory, electrolytes are treated as ideal ionic gases, and the ionic concentrations are related to the electrostatic potential by the Boltzmann distributions. This theory, often very efficient, thus works well for monovalent ions, low surface charge densities, and high solvent dielectric coefficients. The mathematical form of the PB theory is the PB equation. This is Poisson’s equation for the electrostatic potential

with the equilibrium ionic concentrations given by the Boltzmann distributions via the electrostatic potential. In a variational setting, such distributions result from the equilibrium conditions for a mean-field electrostatic free-energy functional of ionic concentrations, where the electrostatic potential is determined by Poisson's equation [CDLM08, FB97, Li09a, Li09b, RR90].

Let me briefly introduce the formulation of the classical PB theory. Consider an electrolyte (i.e., ionic solution) occupying a region $\Omega \subset \mathbb{R}^3$. Assume there are M ionic species in the solution. For the i th ionic species, denote its valence by Z_i and its charge by $q_i = z_i e$, where e is the elementary charge. Let us also denote by $c_i = c_i(x)$ the concentration of the i th ionic species at $x \in \Omega$. Assume $\rho_f : \Omega \rightarrow \mathbb{R}$ to be a given function that represents the density of fixed charges. Then the total charge density is

$$\rho = \rho_f + \sum_{i=1}^M q_i c_i \quad \text{in } \Omega, \quad (1.1)$$

where the summation part is the density of charges from all the ions. Let us denote by $\psi = \psi(x)$ the electrostatic potential at $x \in \Omega$. This is the primary quantity in describing the electrostatic properties. It is governed by Poisson's equation

$$-\nabla \cdot \varepsilon \nabla \psi = \rho, \quad (1.2)$$

where $\varepsilon = \varepsilon(x)$ is the dielectric coefficient, often a known quantity. Note that other useful quantities are the electric field $\vec{E} = -\nabla \psi$ and electrostatic displacement $\vec{D} = \varepsilon \vec{E}$.

The key in the classical PB theory is the following Boltzmann distributions that connect the local ionic concentrations c_i to the electrostatic potential ψ :

$$c_i = c_i^\infty e^{\beta q_i \psi}, \quad i = 1, \dots, M. \quad (1.3)$$

Here $\beta = (k_B T)^{-1}$ with k_B the Boltzmann constant and T the absolute temperature, and c_i^∞ is the bulk concentration of i th ionic species. Combining the charge density (1.1), Poisson's equation (1.2), and the Boltzmann distributions (1.3) we then obtain the nonlinear partial differential equation

$$-\nabla \cdot \varepsilon \nabla \psi = \rho_f + \sum_{i=1}^M q_i c_i^\infty e^{\beta q_i \psi}. \quad (1.4)$$

This is the celebrated PB equation. It, together with some boundary conditions, determines the electrostatic potential ψ and in turn also determines the ionic concentration c_i by the Boltzmann distributions.

The classical PB theory is in fact variational. It is based on the following electrostatic free-energy functional:

$$F[c_1, \dots, c_M] = \int_{\Omega} \left\{ \frac{1}{2} \rho \psi + \beta^{-1} \sum_{i=1}^M c_i [\log(\Lambda^3 c_i) - 1] - \sum_{i=1}^M \mu_i c_i \right\} dx. \quad (1.5)$$

Here Λ is the thermal de Broglie wavelength and μ_i the chemical potential of i th ionic species, which is often experimentally measurable. The first part is the electrostatic potential energy, the electrostatic potential ψ is determined by Poisson's equation (1.2) together with some boundary conditions. The second part is the ideal-gas entropy of ionic concentrations. The last part is the chemical potentials of all the ionic species. Note that the concentrations c_1, \dots, c_M are the direct variables but ψ is not. Now, at equilibrium concentrations c_1, \dots, c_M , all the first variation vanish: $\delta_{c_i} F = 0$ ($i = 1, \dots, M$). These are exactly the Boltzmann distributions (1.3).

Despite the overall success of the classical PB theory made in recent two decades, it has several well-known limitations. Mostly it is caused by ignoring the ion-ion correlations and ion specific properties. Thus the theory will provide accurate descriptions of the ionic solution when the system only has monovalent ions and low-charged surfaces. But it fails to provide reasonable descriptions where ions are crowded and surfaces are highly charged. Without including the ionic size effect, the classical PB theory predicts unreasonably high ionic concentration near a charged surface. In a system with multiple species of ions, the result from classical PB indicates that all ions will stack near the surface, which is impossible in a highly charged system. Moreover, scenarios of crowded ions are often seen in a system with highly charged object. This will cause the reduction of the relative permittivity of the solvent [KD09, BYAP11]. The assumption that the relative permittivity is a constant in a mean-field theory, is not accurate for such a system. This results in another inaccurate factor in the PB mean-field description.

In this dissertation, I mainly study two modified PB mean-field models.

The first model includes finite ionic sizes and concentration of solvent molecules into the PB model. This improvement overcomes one of the major issues of PB theory, i.e., it cannot provide reasonable description near highly charged surface with multiple species of ions. The improved model has been studied theoretically by Li [Li09a], and numerically by Zhou, Wang, and Li [ZWL11]. The model with non-uniform sizes captures the counterion stratification phenomena. It is confirmed by Monte Carlo simulations in this work. The second one is a mean-field model with a self-consistent dielectric response. The constant dielectric coefficient works well in a system with low ionic concentration. But it decreases when the ionic concentration increases. This is confirmed by experiment and simulations [KD09]. Frydel [Fry11] has considered a modified effective dielectric constant and the Boltzmann distribution, and studied a polarizable PB theory. Andelman *et al.* also studied a simple system with the dielectric constant which depends linearly on the concentration [BYAP11]. Moreover, Ma and Xu proposed a self-consistent field model for inhomogeneous dielectric media [MX14]. Their modeling results agree with related simulations [FXH14]. My analysis reveals that the widely used free-energy functional is in fact nonconvex in this case. My numerical computations confirm some of the experimental observations.

1.2.3 Phase-field models

The phase-field theories and methods have been widely used in studying interface problems arising in many scientific areas, such as materials physics, complex fluids, and biomembranes, cf. e.g., [AMW98, BKM05, BWBK02, Che02, CL85, DLW04, DLRW05, Emm03, Gla03, GGHW65, KKL01, Lan86, TCC06, VvdVM01, SRL10, YFLS04] and the references therein. The idea of phase-field modeling is to represent a sharp interface by a smooth function ϕ , which takes the value 1 on one side of the interface and 0 on the other side, and transitions from 1 to 0 crossing the interface; see Figure 1.3 for an example of an one-dimensional phase-field function. To determine the phase-field function ϕ , one can solve the question

$$\frac{\partial \phi}{\partial t} = \xi \Delta \phi - \frac{1}{\xi} W'(\phi).$$

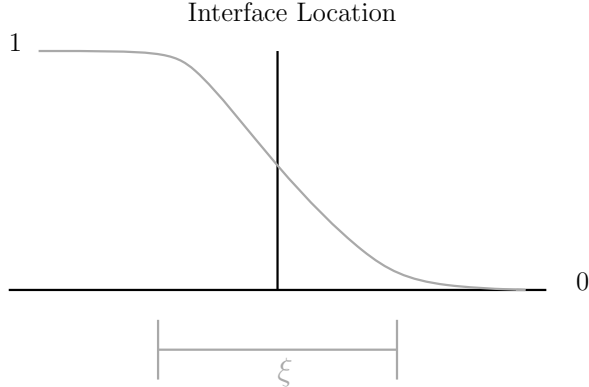


Figure 1.3: The phase-field function.

This is the gradient flow of the energy functional

$$F_\xi[\phi] = \int_\Omega \left[\frac{\xi}{2} |\nabla\phi|^2 + \frac{1}{\xi} W(\phi) \right] dx,$$

i.e., $\partial_t\phi = -\delta_\phi F_\xi[\phi]$, where $W(t) = ct^2(1-t)^2$ is a double well potential with a suitable prefactor $c > 0$ minimized at 0 and 1, $\xi > 0$ is a small numerical parameter that characterizes the width of the transition layer, and Ω is a computational domain. If $F_\xi[\phi]$ is small then the term $(1/\xi)W(\phi)$ makes that $\phi \approx 0$ or $\phi \approx 1$ in the region. When ξ becomes smaller and smaller, the transition characterized by the phase-field function becomes a sharp interface; and the corresponding integral value becomes proportional to the interracial area. The advantage of phase-field approach is the capability of handling interfacial topological changes and fluctuations, which are crucial in the transition of one equilibrium conformation to another in biomolecular systems. Existing studies have shown that interfacial fluctuations can be described in a phase-field approach [KR99,BRP05]. One can also couple the dielectric boundary PB equation into this framework by assuming the dielectric coefficient $\varepsilon = \varepsilon(\phi)$ to depend on the phase-field function ϕ . Here, $\varepsilon(0)$ and $\varepsilon(1)$ should be set as the dielectric coefficient in water and solute regions, respectively.

1.3 Summary of the Dissertation Work

This dissertation consists of three parts. In the first part, I study the modified mean-field theory with ionic size effects. I also design a MC simulation method

to investigate in depth the ionic size effect. In the second part of the work, I construct a mean-field model with ionic concentration dependent dielectric. Moreover, I analyze the governing free-energy functional. Through my computations, I also observe interesting phenomena described by this modification. In the third part, I combine the PB electrostatics with a phase-field model to study charged molecules in water.

1.3.1 Monte Carlo simulations of ionic size effects

In the first part of my dissertation work (cf. Chapter 2), I investigate the size-modified mean-field model. I summarize the theoretical results and numerical algorithms of this model. I then design a specific Monte Carlo (MC) simulation technique for a system of a mixture of crowded mobile ions with different sizes and valences. I simulate the competition of multiple species of ions near the surface. Through the extensive MC simulations and mean-field computations, I obtain the following results:

- (1) For a low surface charge density, the adsorption of counterions with a higher valence is preferable. This agrees with previous studies in existing the literature. For a highly charged surface, both of the mean-field theory and MC simulations show that the counterions bind tightly around the charged surface, forming stratification or layering of counterions of different species.
- (2) The ionic valence-to-volume ratios, instead of ionic valences alone, are the key parameters that determine the binding of counterions to the charged surface. Due to the ionic size effect, counterions with the largest valence-to-volume ratio form the first layer of stratification, while those with the second largest valence-to-volume ratio form the second layer, and so on. I shall call this the “criterion of valence-to-volume ratios” in ionic stratification. My MC simulations confirm the validity of this criterion that was discovered in the previous mean-field calculations [ZWL11].
- (3) The MC simulations predict the charge inversion for ionic systems with salt. Moreover, I find that the over-charging is more significant for a system with monovalent coions than for a system with divalent coions. The mean-field

theory, however, fails in predicting the charge inversion, since it does not include the ion-ion correlation.

1.3.2 Theory and computation of electrostatics with ionic concentration dependent dielectrics

In this part (cf. Chapter 3), I construct a mean-field variational model to study how the dependence of dielectric coefficient on local ionic concentrations affects the electrostatic interaction in an ionic solution near a charged surface. Experiment and simulations have indicated the relation between the coefficient and ionic concentration [HRC48,LZ98]. Figure 1.4 shows the experimentally measured dependence of the dielectric coefficient on the concentration of NaCl and fitted curve.

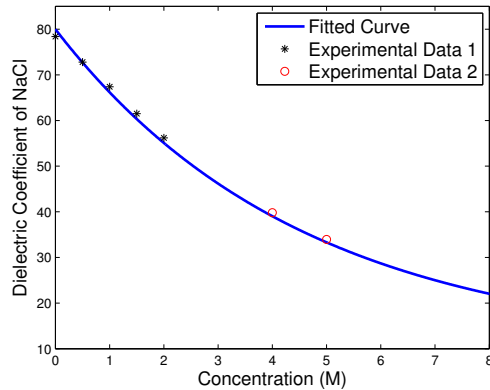


Figure 1.4: The dielectric coefficient for NaCl solution.

I study theoretically and numerically the variational problem of minimizing the free-energy functional (1.5) together with Poisson's equation (1.2). But the dielectric coefficient ε is assumed now to depend on the total concentration $\bar{c} = \sum_{i=1}^M c_i$ as in Figure 1.4. My main results are as follows:

- (1) I derive the first and second variations of the electrostatic free-energy functional (3.1). Setting the first variation to zero, I obtain the following generalized Boltzmann distributions that relate the equilibrium concentrations

c_1, \dots, c_M to the corresponding electrostatic potential ψ :

$$c_i = c_i^\infty \exp \left\{ -\beta \left[q_i \psi + \frac{1}{2} \varepsilon'(\bar{c}) \varepsilon_0 |\nabla \psi|^2 \right] \right\}, \quad i = 1, \dots, M,$$

where c_i^∞ is the bulk concentration of the i th ionic species.

- (2) I show by numerical calculations that there are possibly multiple values of concentrations $c = (c_1, \dots, c_M)$ that can depend on the same potential ψ through the generalized Boltzmann distributions. I also construct some examples to prove that the free-energy functional can be indeed nonconvex.
- (3) I minimize numerically the electrostatic free-energy functional for a radially symmetric system of both counterions and coions., and find several interesting properties of the electrostatic interactions attributed to the dependence of dielectric on ionic concentrations. These include the depletion of ions near a charged surface, the non-monotonicity of ionic concentrations near such a surface, and the shift of peaks of the ionic concentration profiles due to the increase of surface charges or bulk concentrations.

1.3.3 Phase-field modeling and computation of charged molecules

Electrostatics are crucial to determining the solvent-solute interface in biological systems. In the third part of my dissertation (cf. Chapter 4), I develop a phase-field variational implicit-solvent approach for the solvation of charged molecules. I employ the free-energy minimization framework with surface energy, van der Waals interactions, and the electrostatic interactions. The main results are as follows:

- (1) I theoretically study the phase-field model with the Poisson–Boltzmann (PB) electrostatics and the free-energy functional.
- (2) I design a semi-implicit numerical scheme coupled with a Poisson’s equation solver to obtain the minimizing phase-field function ϕ . In order to remove the singularity of the Poisson equation with point charge, I incorporate the reaction field ψ_{reac} to solve the equation.

- (3) I investigate a spherical model system numerically. The comparison of my model with sharp interface results indicates that my model is reliable and accurate. I can clearly see the convergence when $\xi \rightarrow 0$. When the point charge Q at the center is larger, the surface will be pushed in due to the strong contribution of the electrostatic energy.

1.4 Outline for the Rest of Dissertation

In Chapter 2, I summarize the mean-field theory and computation, and then investigate the counterion stratification phenomena by MC simulations. In Chapter 3, I develop a rigorous mean-field theory for electrostatics with concentration dependent dielectric. Then I study a model system using numerical computation by minimizing the free-energy functional. In Chapter 4, I study the phase-field modeling of charged molecules. Finally, in Chapter 5, I draw conclusions.

Chapter 2

Theory and Computation of Ionic Size Effects

2.1 Introduction

A common scenario of electrostatic interactions is a mixture of crowded mobile ions of multiple species with different valences and sizes in an electrolyte surrounding an external charged surface. Excluded-volume effects or size effects of such mobile ions, in particular effects of different ionic sizes, contribute significantly to the electrostatic free energy and forces, which in turn determine the structure and stability of an underlying system. For instance, the size of monovalent cations can influence the stability of RNA tertiary structures [LLSD09]; and differences in ionic sizes can also affect how mobile ions bind to nucleic acids [BTC⁺07, BAR80]. Concentrations of ions in an ion channel can reach as high as dozens of mol/L (about 30 M in calcium and sodium channels), and the ionic sizes can affect the ion transport and channel selectivity [Eis11]. The charge densities in active sites of enzymes and DNAs are also found very high, and the sizes of surrounding mobile ions can affect many biological functions of these macromolecules. In ionic liquids at room temperature, charged electrode/solution interfaces contain electric double layers (EDL) with a nominal specific capacitance of 25 $\mu\text{F}/\text{cm}^2$ [Con99]. The effect of non-uniform ionic sizes to the EDL structure can be significant. Detailed density-

functional theory calculations, Monte Carlo simulations, and integral equations calculations confirm some of these experimentally observed properties due to the non-uniformity of ionic sizes [HPP10, Kor07, QPMMHÁ04, VBG07, WYGL05].

For years, attempts have been made to include ionic size effects, particularly nonuniform ionic size effects, into a PB-like efficient approach [BAO97, BAO00, BD12, CBL⁺07, KII96, Li09a, Tre08, ZWL11]. See also [ABH05, BSK11, BKSA09, Bik42, EHL10, KBA07a, KBA07b, LZ11]. One of the key ideas has been to introduce the local concentration of solvent molecules, in addition to those of ions of multiple species, and to incorporate all the ionic and solvent molecular volumes in the entropic part of a mean-field electrostatic free-energy functional. If all linear sizes (including that of solvent molecules) are the same, such a free-energy functional can be derived using a lattice-gas model [BAO00, KII96, Tre08]. Moreover, there are explicit formulas, the generalized Boltzmann distributions, relating equilibrium ionic concentrations and the corresponding electrostatic potential. These distributions, together with Poisson's equation, lead to the generalized PB equation for the case of a uniform ionic size [Li09a, Li09b, SBHF10]. For a system of three ionic species with two different ionic sizes, Chu *et al.* [CBL⁺07] derived a different size-modified PB equation from a similar lattice-gas model and applied this equation to study the ionic size effect in the binding of ions to DNA. For a general system, Tresset [Tre08] derived an expression of the free energy with an effective volume fraction of free space, under the assumption that the ionic excluded volumes are dispersed from each other to a reasonable extent.

For the general case of multiple ionic species with different valences and sizes, Li [Li09a] proposed and analyzed a semi-phenomenological free-energy functional of ionic concentrations with Poisson's equation as a constraint for the electrostatic potential. This functional is obtained simply by using different individual ionic sizes instead of a uniform size in the previous functional derived from a lattice-gas model. Equilibrium conditions for the new and general free-energy functional are nonlinear algebraic equations for the equilibrium concentrations. It is shown that such conditions determine completely the dependence of equilibrium ionic concentrations on the corresponding electrostatic potential [Li09a]. Explicit

formulas of such dependence and hence Boltzmann-like distributions for the equilibrium concentrations, however, seem unavailable. Therefore, there is no explicit PB-like equation of the electrostatic potential in the general case.

Nevertheless, Zhou *et al.* [ZWL11] developed a robust numerical method for minimizing such a functional to obtain the equilibrium ionic concentrations and the corresponding electrostatic potential. The starting point there is to reformulate the variational problem as a constrained optimization problem [BSD09,MR02]. An augmented Lagrange multiplier method is then constructed and implemented to solve this constrained optimization problem. Extensive numerical results reported in [ZWL11] demonstrate that the new mean-field, size-effect included model can describe many detailed properties of ionic concentrations, including the stratification of concentrations, that have been predicted by other refined models but not by the classical PB theory; cf. [BD12, Tre08]. In particular, it is found that the ionic valence-to-volume ratio is the key parameter in the stratification [ZWL11].

In this part of my dissertation work, I study the ionic size or excluded volume effect to the structure of electrical double layer in the vicinity of a highly charged surface, using both the mean-field model and Monte Carlo (MC) simulations. My goal is two-fold. First, I would like to understand how counterions with different valences and sizes compete in the adsorption to the charged surface, and how the ionic valence-to-volume ratio affect the ordering of ion packing near such a surface. Second, I would like to examine the validity of the mean-field theory with nonuniform size effects by comparing it with the MC simulations.

The adsorption of counterions to a charged surface is determined by the competition between the entropic and energetic contributions of an underlying system of electrolyte. The ionic size effect is quite significant in such adsorption, since the excluded volume of crowded ions reduces the mixed entropy, and thus increases the Helmholtz free energy of the total system. The competition of entropy and energy results in a stratification of counterions of different species in the electrical double layer, as revealed in both experimental investigations [TVT06] and theoretical predictions [AGV06, TSY05, Tre08, ZWL11]. For a low surface charge density, the electrostatic interaction dominates and the ions with higher

valence are most likely to stay closest to the charged surface. For a highly charged surface, smaller counterions are stronger in competition to form the first layer of the stratification [TSYT05, VBG07]. My mean-field numerical computations and MC simulations reproduce these results. In particular, my MC simulations validate the prediction by the mean-field theory of the role of ionic valence-to-volume ratios in the counterion stratification.

My simulation system consists of a spherical macroion immersed centrally in an electrolyte system. There are counterions of multiple species in the electrolyte. The entire system is assumed to be neutral in charge. The parameters of the system include the linear size of the simulation box, the radius and constant surface charge density of the macroion, and the valence, volume, and total number of each species of (micro) mobile ions. The same set of parameters are used in my MC simulations and mean-field computations. I use unrestrictive primitive models of ionic system, treating ions as hard spheres. Based on such a model, I use canonical ensemble MC simulations with Metropolis criterion. I plot the radial particle density function for each species of mobile ions. Such functions are compared with the corresponding equilibrium ionic concentrations predicted by my mean-field theory.

The rest of this chapter is organized as follows: In Section 2.2, I introduce the mean-field theory and numerical method for nonuniform ionic size effects. In Section 2.3, I describe my MC simulations method. In Section 2.4, I present and discuss the results of my MC simulations and mean-field computations. In Section 2.5, I make several remarks.

2.2 Mean-Field Theory and Method

Let us consider an electrolyte with M species of ions. For each i ($1 \leq i \leq M$), let us denote by z_i the valence and v_i the volume of an ion of the i th species. Let us also denote by N_i the total number of ions of the i th species. The total number of all ions is $N = \sum_{i=1}^M N_i$. We assume that there is a spherical colloidal particle—a charged macroion—of radius R inside the electrolyte solution and that its charge effect is described effectively by a constant surface charge

density, denoted σ . We assume the system charge neutrality

$$ze + \sum_{i=1}^M N_i z_i e = 0, \quad (2.1)$$

where $z = 4\pi R^2 \sigma / e$ is the valence of the macroion and e is the elementary charge.

Assume that the entire system occupies the cubical region $(-L/2, L/2)^3$ with the linear size $L > 2R$ and that the macroion occupies the spherical region B_R of radius R centered at the origin. Therefore all the ions are in the region $\Omega = (-L/2, L/2)^3 \setminus B_R$. Denote by $\Gamma = \partial B_R$ the boundary of the sphere B_R , i.e., the spherical surface of the macroion.

2.2.1 A mean-field theory with nonuniform size effects

For each i ($1 \leq i \leq M$), let us denote by $c_i(\mathbf{r})$ the local concentration at a spatial point $\mathbf{r} \in \Omega$ of ions of the i th species. The charge density of solution is then given by $\sum_{i=1}^M z_i e c_i(\mathbf{r})$ ($\mathbf{r} \in \Omega$). All the concentrations $c_i(\mathbf{r})$ are constrained by

$$\int_{\Omega} c_i dV = N_i, \quad i = 1, \dots, M. \quad (2.2)$$

We also denote by v_0 the volume of a solvent molecule. The local concentration $c_0 = c_0(\mathbf{r})$ of the solvent molecules is defined by

$$c_0(\mathbf{r}) = v_0^{-1} \left[1 - \sum_{i=1}^M v_i c_i(\mathbf{r}) \right] \quad \text{for all } \mathbf{r} \in \Omega.$$

For a given set of ionic concentrations $c = (c_1, \dots, c_M)$, a mean-field approximation of the electrostatic free energy is given by

$$F[c] = F_{\text{pot}}[c] + F_{\text{ent}}[c]. \quad (2.3)$$

The first part $F_{\text{pot}}[c]$ is the electrostatic potential energy, defined by

$$F_{\text{pot}}[c] = \int_{\Omega} \frac{1}{2} \left(\sum_{i=1}^M z_i e c_i \right) \Phi dV + \int_{\Gamma} \frac{1}{2} \sigma \Phi dS, \quad (2.4)$$

where Φ is the electrostatic potential. It is determined by Poisson's equation

$$\nabla \cdot \varepsilon \varepsilon_0 \nabla \Phi = - \sum_{i=1}^M z_i e c_i \quad \text{in } \Omega, \quad (2.5)$$

together with the boundary condition

$$\varepsilon\varepsilon_0\frac{\partial\Phi}{\partial n}=\begin{cases}\sigma & \text{on } \Gamma, \\ 0 & \text{on } \Gamma_{\text{box}},\end{cases}\quad (2.6)$$

where ε_0 is the vacuum permittivity, ε is the relative permittivity or dielectric coefficient of the solution, and n is the exterior unit normal at the boundary of Ω that consists of the spherical surface Γ and the boundary, Γ_{box} , of the box $(-L/2, L/2)^3$. We shall assume that ε is a constant in the entire solution region Ω . Notice that Φ is not an independent variable of the functional $F[c]$.

The second part $F_{\text{ent}}[c]$ is the entropic contribution. It is given by [Li09a, ZWL11]

$$F_{\text{ent}}[c]=k_B T\sum_{i=0}^M\int_{\Omega}c_i[\log(v_i c_i)-1]dV,\quad (2.7)$$

where k_B is the Boltzmann constant and T is the absolute temperature. Notice that the summation index starts from $i=0$. Notice also that in the variational approach to the classical PB equation, the solvent entropy is not included and all the ionic linear sizes $v_i^{1/3}$ are replaced by the de Broglie wave length [CDLM08, FB97, Li09b]; cf. (1.5). The set of equilibrium ionic concentrations $c=(c_1, \dots, c_M)$ is defined to minimize the free-energy functional (2.3), subject to the constraint (2.2). The equilibrium electrostatic potential is determined by the corresponding equilibrium ionic concentrations through Poisson's equation (2.5) and the boundary condition (2.6).

Alternatively, we can introduce for each i the chemical potential μ_i for ions of the i th species, and add the following term

$$-\sum_{i=1}^M\int_{\Omega}\mu_i c_i dV\quad (2.8)$$

to the free energy $F[c]$ in (2.3). The chemical potentials μ_i ($i=1, \dots, M$) can be regarded as Lagrange multipliers accounting for the constraint (2.2). With these chemical potentials, one minimizes the new, total electrostatic free-energy functional that now consists of all the integral terms in (3.10), (3.11), and (2.8), without the constraint (2.2).

Taking the variational derivative with respect to each concentration field $c_i(\mathbf{r})$ of the new, total free energy and setting it to 0, we obtain with suitable boundary conditions for Poisson's equation (2.5) the conditions for equilibrium concentrations c_1, \dots, c_M [Li09a]

$$\frac{v_i}{v_0} \log(v_0 c_0(\mathbf{r})) - \log(v_i c_i(\mathbf{r})) = \frac{1}{k_B T} [z_i e \Phi(\mathbf{r}) - \mu_i] \quad \text{for all } \mathbf{r} \in \Omega, \quad i = 1, \dots, M. \quad (2.9)$$

In the special case that $v_0 = v_1 = \dots = v_M$, one can solve this system of non-linear algebraic equations to obtain explicit formulas of $c_i(\mathbf{r}) = c_i(\Phi(\mathbf{r}))$ ($i = 1, \dots, M$). These are the generalized Boltzmann distributions. For the general case, it is known that the conditions (2.9) determine uniquely $c_i(\mathbf{r}) = c_i(\Phi(\mathbf{r}))$ ($i = 1, \dots, M$); but explicit formulas for such dependence seem unavailable. See [Li09a, Li09b].

2.2.2 A constrained optimization method

By integration by parts, Poisson's equation (2.5), and the boundary conditions (2.6), we can rewrite the free-energy functional (2.3), which is the sum of $F_{\text{pot}}[c]$ given in (3.10) and $F_{\text{ent}}[c]$ given in (3.11), as

$$F[\Phi, c] = \int_{\Omega} \left\{ \frac{\varepsilon \varepsilon_0}{2} |\nabla \Phi|^2 + k_B T \sum_{i=0}^M c_i [\log(v_i c_i) - 1] \right\} dV,$$

where Φ solves the boundary-value problem of Poisson's equation (2.5) and (2.6). Notice that the dependence of F on Φ is now explicitly indicated. One can verify mathematically that the minimization of $F[c]$ defined in (2.3) over all c subject to (2.2) is equivalent to that of $F[\Phi, c]$ over all (Φ, c) subject to (2.2), (2.5), and (2.6).

Introduce the Bjerrum length $l_B = e^2 / (4\pi \varepsilon \varepsilon_0 k_B T)$. Define $\Phi' = e\Phi / (k_B T)$, $c'_i = 4\pi l_B c_i$ and $v'_i = (4\pi l_B)^{-1} v_i$ ($0 \leq i \leq M$), $N'_i = 4\pi l_B N_i$ ($1 \leq i \leq M$), $\sigma' = 4\pi l_B \sigma / e$, and $\omega' = (4\pi l_B)^{-1/3} \omega$ for $\omega = \Gamma, \Gamma_{\text{box}},$ or Ω . Then $F[\Phi, c] = \varepsilon \varepsilon_0 (k_B T / e)^2 F'[\Phi', c']$, where

$$F'[\Phi', c'] = \int_{\Omega'} \left\{ \frac{1}{2} |\nabla \Phi'|^2 + \sum_{i=0}^M c'_i [\log(v'_i c'_i) - 1] \right\} dV, \quad (2.10)$$

and c'_0 is defined similarly using the primed quantities. The constraint (2.2), Poisson's equation (2.5), and the boundary condition (2.6) become now

$$\int_{\Omega'} c'_i dV = N'_i, \quad (2.11)$$

$$\Delta\Phi' = -\sum_{i=1}^M z_i c'_i \quad \text{in } \Omega', \quad (2.12)$$

$$\frac{\partial\Phi'}{\partial n'} = \begin{cases} \sigma' & \text{on } \Gamma', \\ 0 & \text{on } \Gamma'_{\text{box}}, \end{cases} \quad (2.13)$$

respectively, where n' is the unit exterior normal at the boundary of Ω' .

For simplicity, we will drop all the primes in what follows.

We apply an augmented Lagrange multiplier method [Ber82,NW99] to numerically minimize the functional $F[\Phi, c]$ defined in (2.10) subject to (2.11)–(2.13) (with all the primes dropped). Our method is an improved version of that developed in our previous work [ZWL11] for minimizing numerically a similar functional formulated using (\mathbf{E}, c) instead of (Φ, c) , where $\mathbf{E} = -\nabla\Phi$ is the electric field. In the augmented Lagrange multiplier formulation, we solve the corresponding saddle-point problem

$$\min_{(\Phi, c)} \max_{(\Psi, \Lambda, \mathbf{s})} \hat{L}(\Phi, c, \Psi, \Lambda, \mathbf{s}), \quad (2.14)$$

where $\Lambda = (\lambda_1, \dots, \lambda_M) \in \mathbb{R}^M$, $\mathbf{s} = (s_1, \dots, s_M) \in \mathbb{R}^M$ with each $s_i \geq 0$, and

$$\begin{aligned} \hat{L}(\Phi, c, \Psi, \Lambda, \mathbf{s}) &= F[\Phi, c] + \int_{\Omega} \Psi \left(\Delta\Phi + \sum_{i=1}^M z_i c_i \right) dV \\ &\quad + \sum_{i=1}^M \lambda_i \left(\int_{\Omega} c_i dV - N_i \right) + \sum_{i=1}^M \frac{s_i}{2} \left(\int_{\Omega} c_i dV - N_i \right)^2 \\ &= \int_{\Omega} \left\{ \frac{1}{2} |\nabla\Phi|^2 + \sum_{i=0}^M c_i [\log(v_i c_i) - 1] \right\} dV \\ &\quad + \int_{\Omega} \Psi \left(\Delta\Phi + \sum_{i=1}^M z_i c_i \right) dV \\ &\quad + \sum_{i=1}^M \lambda_i \left(\int_{\Omega} c_i dV - N_i \right) + \sum_{i=1}^M \frac{s_i}{2} \left(\int_{\Omega} c_i dV - N_i \right)^2. \end{aligned}$$

The function Ψ is the Lagrange multiplier for Poisson's equation (2.5). It satisfies the same boundary conditions as for Φ , cf. (2.13) (no primes). The numbers

$\lambda_1, \dots, \lambda_M$ are the Lagrange multipliers for the constraint (2.11) (no primes). The last summation term is a penalty term. It is added to stabilize and accelerate our numerical iterations.

The solution $(\Phi, c, \Psi, \Lambda, \mathbf{s})$ to the saddle-point problem (2.14) is determined by the following equations:

$$\frac{\partial \hat{L}}{\partial \Phi} = -\Delta(\Phi - \Psi) = 0 \quad \text{in } \Omega, \quad (2.15)$$

$$\frac{\partial \hat{L}}{\partial \Psi} = \Delta \Phi + \sum_{i=1}^M z_i c_i = 0 \quad \text{in } \Omega, \quad (2.16)$$

$$\begin{aligned} \frac{\partial \hat{L}}{\partial c_i} &= \log(v_i c_i) - \frac{v_i}{v_0} \log\left(v_0 \left(1 - \sum_{j=1}^M v_j c_j\right)\right) + z_i \Psi + \lambda_i + s_i \left(\int_{\Omega} c_i dV - N_i\right) \\ &= 0 \quad \text{in } \Omega, \quad i = 1, \dots, M, \end{aligned} \quad (2.17)$$

$$\frac{\partial \hat{L}}{\partial \lambda_i} = \int_{\Omega} c_i dV - N_i = 0, \quad i = 1, \dots, M. \quad (2.18)$$

Since both Φ and Ψ satisfy the same boundary conditions, Eq. (2.15) implies that they differ by an additive constant. We may choose this constant to be 0 and assume that $\Psi = \Phi$ in Ω . Notice that Eq. (2.16) is Poisson's equation (2.12) (no primes) and Eq. (2.18) is the constraint (2.11) (no primes). As pointed out before, the nonlinear system of algebraic equations (2.17) has a unique solution $c = (c_1, \dots, c_M)$ but its explicit solution formulas seem unavailable [Li09a].

The entire system of equations is equivalent now to the three sets of equations (2.16)–(2.18) with Ψ in (2.17) replaced by Φ . We solve these equations by the following algorithm:

Algorithm.

- Step 0. Distribute the total surface charge $4\pi R^2 \sigma$ uniformly on the spherical surface by interpolation onto the nearest grids [BSD09, ZWL11]. Initialize $\Phi^{(0)}, c^{(0)} = (c_1^{(0)}, \dots, c_M^{(0)})$, $\Lambda^{(0)} = (\lambda_1^{(0)}, \dots, \lambda_M^{(0)})$, and $\mathbf{s}^{(0)} = (s_1^{(0)}, \dots, s_M^{(0)})$. Choose a parameter $\gamma > 1$. Set $l = 0$.
- Step 1. Solve Eq. (2.16) with c_i replaced by $c_i^{(l)}$, together with the boundary condition (2.13), to obtain the solution $\Phi^{(l+1)}$.
- Step 2. Use Newton's method to solve Eq. (2.17) (where Ψ is replaced by Φ) with

Φ , Λ , and \mathbf{s} replaced by $\Phi^{(l+1)}$, $\Lambda^{(l)}$, and $\mathbf{s}^{(l)}$, respectively, to obtain the solution $c^{(l+1)}$.

Step 3. Update the Lagrange multipliers

$$\lambda_i^{(l+1)} = \lambda_i^{(l)} + s_i^{(l)} \left(\int_{\Omega} c_i^{(l+1)} dV - N_i \right), \quad i = 1, \dots, M.$$

Update the penalty parameters $s_i^{(l+1)} = \gamma s_i^{(l)}$ ($i = 1, \dots, M$).

Step 4. Test convergence. If not, set $l \leftarrow l + 1$ and go to Step 1.

The parameter $\gamma > 1$ is used only for updating s_i ($i = 1, \dots, M$). Various kinds of approximations can be used to solve the boundary-value problem of Poisson's equation. For instance, we can use the periodic boundary condition instead, and apply the fast Fourier transform. In this case, we have the linear complexity in terms of the number of unknowns of resulting system of linear equations. We note that the matrix-vector multiplication can be avoided in Newton's iteration scheme for solving the system (2.17) (with Ψ replaced by Φ), since the exact formula of the inverse of related Jacobian matrix can be obtained.

2.3 Monte Carlo Simulations

We consider the same system described in the previous section: A macroion occupying the sphere B_R of radius R centered at the origin, with a constant surface charge density σ , is immersed in an electrolyte in the box $(-L/2, L/2)^3$. There are M species of (micro) ions in the region $\Omega = (-L/2, L/2)^3 \setminus B_R$. For each i ($1 \leq i \leq M$), an ion of the i th species has valence z_i and volume v_i . The number of ions of the i th species is N_i ; and the total number of all (micro) ions is $N = \sum_{i=1}^M N_i$.

We use an unrestricted primitive model for our underlying electrolyte system; and apply the canonical ensemble Monte Carlo (MC) simulations with the Metropolis criterion [AAN09, AGV06, BV92, FS02, MRR⁺53, VC80].

In a primitive model of electrolytes, the mobile ions are represented by charged hard spheres and the solvent is modeled through its dielectric permittivity ε . We label all the (micro) ions by $k = 1, \dots, N$. We denote by \hat{z}_k and \hat{R}_k the

valence and radius of the k th ion. If the k th ion is of the i th type ($1 \leq i \leq M$), then its valence is $\hat{z}_k = z_i$ and its volume is $4\pi\hat{R}_k^3/3 = v_i$. For convenience, we label the spherical macroion by 0 and denote $\hat{R}_0 = R$, the radius of the macroion. We also denote its valence by $\hat{z}_0 = z = 4\pi R^2\sigma/e$.

For a given configuration of the system, the Hamiltonian is defined to be the work needed to bring all the ions from infinity to their current positions. It is the sum of all pairwise interaction energies between all the ions, including the macroion.

We only consider the hard-sphere contribution and the Coulomb interaction. Therefore, we define the total potential energy of the system to be

$$U = \sum_{0 \leq j < k \leq N} u_{jk},$$

where

$$\beta u_{jk} = \begin{cases} \frac{l_B \hat{z}_j \hat{z}_k}{r_{jk}} & \text{if } r_{jk} \geq \hat{R}_j + \hat{R}_k, \\ \infty & \text{if } r_{jk} < \hat{R}_j + \hat{R}_k. \end{cases} \quad (2.19)$$

Here, $\beta = (k_B T)^{-1}$, $l_B = e^2\beta/(4\pi\epsilon\epsilon_0)$ is the Bjerrum length, and r_{jk} is the center-center distance between the j th and k th ions. Notice that, in the case $r_{jk} \geq \hat{R}_j + \hat{R}_k$, u_{jk} is just the Coulomb interaction energy between the j th and k th ions in the solvent with the relative dielectric permittivity ϵ . We shall consider the water solvent at room-temperature and thus take $l_B = 7 \text{ \AA}$.

Our MC simulations consist of a sequence of single-particle moves with the periodical boundary condition. In each move, we randomly select an individual particle (i.e., mobile ion). Let us assume that the selected particle is centered at \mathbf{p} . We then randomly generate a positive number, denoted a , from the interval $[0, \Delta_{\max}]$ for some parameter $\Delta_{\max} > 0$. We finally place the (center of) selected particle randomly on the sphere of radius a centered at \mathbf{p} . We use the L -periodical boundary condition in each direction, so that all the ions remain in the region Ω of electrolyte.

The parameter Δ_{\max} can change during the MC moves. The acceptance or rejection of the move is determined by the Metropolis criterion. We calculate the difference $\Delta U = U_{\text{new}} - U_{\text{old}}$ of the energies of the previous (old) and current

(new) configurations. If $\Delta U \leq 0$, the move is accepted. Otherwise, it is accepted if $\exp(-\beta\Delta U)$ is greater than a randomly generated number in $[0, 1]$.

The entire sequence of our MC moves are divided into three parts: acceleration, equilibration, and statistics. Typically, our simulation system consists of $M = 3$ or 4 ionic species; and the number of ions in each of these species can vary from 25 to 50 and to 200. With these parameters, we usually perform $12 \times 10^5 N$ MC moves in total, with the first $10^5 N$ moves for acceleration, the next $10^5 N$ moves for equilibrating the system, and the last $10^6 N$ moves for statistics, where N is the total number of mobile ions.

We introduce a parameter \tilde{l}_B to replace l_B in the definition of interaction (2.19), and dynamically change \tilde{l}_B in the first part of moves, a total of $10^5 N$ of them, to speed up the thermal equilibration of the crowded system of particles. We generate a geometrical sequence of $10^5 N$ terms with the first and last terms being 1 and $l_B = 7 \text{ \AA}$, respectively. In the m th MC move with $m \leq 10^5 N$, the parameter \tilde{l}_B is taken to be the m th term in the geometrical sequence. After the first $10^5 N$ moves, we fix $\tilde{l}_B = l_B$ for all of the rest MC moves. We run another $10^5 N$ moves so that the system can reach an equilibrium.

Throughout the entire simulation, we keep the percentage of acceptance of MC moves between 20% and 50% by adaptively adjusting the value of the maximum length Δ_{\max} . Initially, we set $\Delta_{\max} = 2 \text{ \AA}$. We then change it after every 100 moves. If the acceptance rate is larger than 50% in current 100 moves, we increase Δ_{\max} by multiplying it by 1.05 but always keep the new value of Δ_{\max} to be less than or equal to \tilde{l}_B . If the acceptance rate is smaller than 20% in current 100 moves, we decrease Δ_{\max} by multiplying it by 0.95, and we keep the new Δ_{\max} to be greater than $0.001 \tilde{l}_B$. In the last part of MC moves, a total of $10^6 N$ of them, we calculate the bulk densities of ions of different species by deriving the production statistics for the macroion-microion radial particle density (RPD). The RPD of the i th ionic species is defined by

$$\rho_i(r) = \frac{\langle N_i(r, r + \Delta r) \rangle}{(4/3)\pi[(r + \Delta r)^3 - r^3]}, \quad (2.20)$$

where $N_i(r, r + \Delta r)$ is the number of ions of the i th species whose centers are in the spherical shell between r and $r + \Delta r$, and the bracket $\langle \cdot \rangle$ represents an

ensemble average over the shell. Notice that the denominator in the definition (2.20) is the volume of the shell. We choose Δr to be 1 Å. In our implementation, we approximate $\langle N_i(r, r + \Delta r) \rangle$ in (2.20) by the total number of ions of the i th species that move (in the last part of moves for statistics) into the shell between r and $r + \Delta r$, multiplied by the total number N_i of ions of i th species, divided by the total number of moves (in the last part of moves) in which an ion of i th species is displaced. The charge density for the i th ionic species is then defined as $\sum_{i=1}^N z_i N_i(r, r + \Delta r)$.

We remark that the use of periodic boundary condition effectively introduces a spatial cut-off of the underlying system region. In principle this can affect the accuracy of the calculation of electrostatic interactions. However, we have tried simulations on boxes with different linear sizes and found almost no differences in the results. In fact, we find that averagely only in one out of 10,000 moves an ion has to “leave” through one side of the box and “come back” to the box through the opposite side. The reason for this is that most of the ions are crowded around the charged sphere, away from the boundary of simulation box.

In Figure 2.1, we display our typical MC simulations results for a salt free system with counterions of valences and radii +1 and 3 Å (black), +2 and 2.5 Å (red), and +3 and 3.5 Å (green), and for a system of salt solvent with coions (blue), and counterions of valences and radii +1 and 2 Å (black), +2 and 3 Å (red), and +3 and 4 Å (green), respectively. Notice that the counterions with smaller valence-to-volume ratios have less possibility to be adsorbed to the charged surface.

2.4 Results and Discussions

We set the linear size of our computational box $(-L/2, L/2)^3$ to be $L = 150$ Å, and the radius of the spherical colloidal particle (the macroion) to be $R = 15$ Å. The Bjerrum length is set to be $l_B = 7$ Å. The surface charge density σ ranges from -0.05 to -0.21 $e/\text{Å}^2$. In our simulations, we investigate mixed solutions of three types of counterions, with their valences $(z_1, z_2, z_3) = (+1, +2, +3)$. We choose their radii to range from 1 Å to 4 Å. These are within the interval of physical

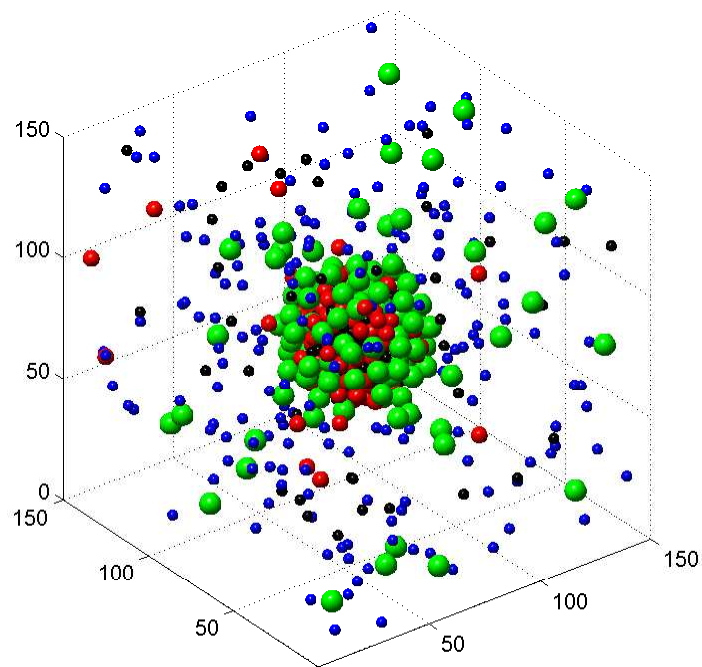
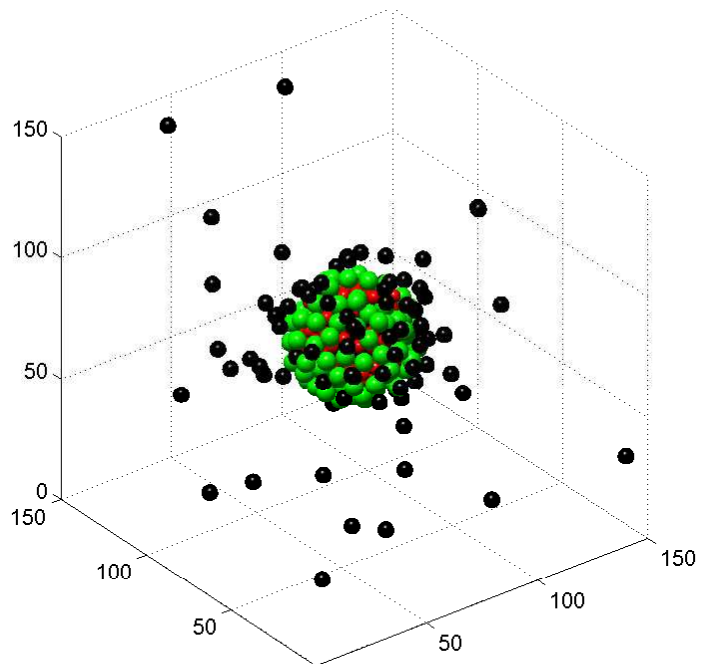


Figure 2.1: Typical Monte Carlo simulations of ions surrounding a highly charged macroion.

interest. For example, the hydrated radii of monovalent hydrogen, sodium and potassium, divalent magnesium and calcium, and trivalent aluminum ions are 4.5, 2.25, 1.5, 4.0, 3.0, and 4.5 Å, respectively [Kie37]. For salt electrolytes, we choose monovalent or divalent coions with radius 2 Å.

One of the main objectives of our study is to understand the competitive adsorption of counterions with different valences and sizes. Such property has been already investigated previously; see [AAN09, AGV06, BV92, GGGTd11, TSYT05, VBG07, WYGL05] and the references therein. Most of these studies found that the valence of counterion determines the competition in adsorption to a charged surface with a low surface charge density and that smaller ions are stronger in such competition for a high surface charge density. These conclusions result naturally from the competition between electrostatic attraction and entropic repulsion expressed in the free-energy functional (2.3), where the electrostatics dominates the free energy for the low surface charge density, and the entropy dominates otherwise. It has been recently found in our previous work [ZWL11] using the mean-field model described in the last section that the competition between different ions in adsorption to a charged surface can be in fact characterized by the ionic valence-to-volume ratios. Here, we use MC simulations to further explore this characterization and compare our results with those from mean-field calculations. In particular, we study a system with a crowded ionic population near a highly charged surface, as shown in Figure 2.1.

In what follows, for an ion of the i th species ($1 \leq i \leq M$), we denote by R_i its radius and by

$$\alpha_i = \frac{z_i}{v_i} = \frac{3z_i}{4\pi R_i^3}$$

its valence-to-volume ratio.

2.4.1 Crucial factors in the competition between counterions

We first study salt-free systems with monovalent, divalent and trivalent counterions: $z_1 = +1$, $z_2 = +2$, and $z_3 = +3$. We investigate three different

groups of such counterions with the following order of valence-to-volume ratios: $\alpha_{+2} > \alpha_{+3} > \alpha_{+1}$; $\alpha_{+3} > \alpha_{+1} > \alpha_{+2}$; and $\alpha_{+1} > \alpha_{+2} > \alpha_{+3}$. Here and below, we use α_{+i} to denote the valence-to-volume ratio of the counterion with valence $+i$. We use the parameters:

$$\begin{aligned} \text{Group 1: } & (R_1, R_2, R_3) = (3.0, 2.5, 3.5) \text{ in } \text{\AA}, \quad \alpha_{+1} : \alpha_{+2} : \alpha_{+3} = 1 : 3.5 : 1.9; \\ \text{Group 2: } & (R_1, R_2, R_3) = (2.5, 3.5, 3.0) \text{ in } \text{\AA}, \quad \alpha_{+1} : \alpha_{+2} : \alpha_{+3} = 1.4 : 1 : 2.4; \\ \text{Group 3: } & (R_1, R_2, R_3) = (2.0, 3.0, 4.0) \text{ in } \text{\AA}, \quad \alpha_{+1} : \alpha_{+2} : \alpha_{+3} = 2.7 : 1.6 : 1. \end{aligned}$$

For each group, we choose the same number of ions for each of the three different species: $N_1 = N_2 = N_3$. Moreover, we select three different surface charge densities by setting $N_1 = N_2 = N_3 = 100, 50,$ and $25,$ respectively, and by using the charge neutrality (2.1). The corresponding surface charge densities of the macroions are $-0.212, -0.106,$ and $-0.053 e/\text{\AA}^2,$ all in the regime of strong surface charge.

The quantitative results are illustrated in Figures 2.2–2.4 with bar plots, where each bar represents the averaged particle density in a spherical shell of thickness $1 \text{ \AA},$ converted to the units mol/L. In the systems in Figures 2.2–2.4, all three species have the same number of ions. This number is 100 (left), 50 (middle), and 25 (right), respectively. Hence the constant surface charge density decreases from left to right. From the figure, we observe clearly that counterions are adsorbed tightly to the highly charged surface, and near the surface layers of counterions of different species form, leading to the remarkable structure of stratification. Moreover, we find that the order of layering depends on the valence-to-volume ratio, instead of the valence or the size independently. Counterions with the largest valence-to-volume ratio forms the first layer closest to the charged surface, those with the second largest such ratio forms the second layer, and so on. When the surface charge density σ becomes smaller, the role of valence is more important in determining which ionic species form a layer closest to the surface. These results demonstrate that the selective adsorption and layer ordering in the stratification depend on the competition between energetics and entropy, and that the valence-to-volume ratio is an important parameter in such adsorption and layering for a highly charged surface.

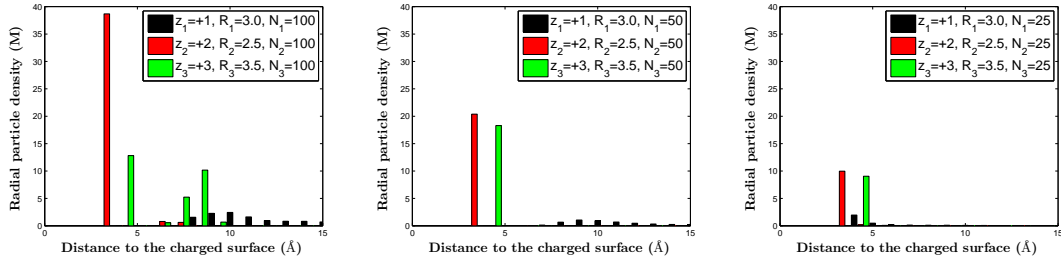


Figure 2.2: The histograms of radial particle density functions for three species of counterions in Group 1: $\alpha_{+1} : \alpha_{+2} : \alpha_{+3} = 1 : 3.5 : 1.9$.

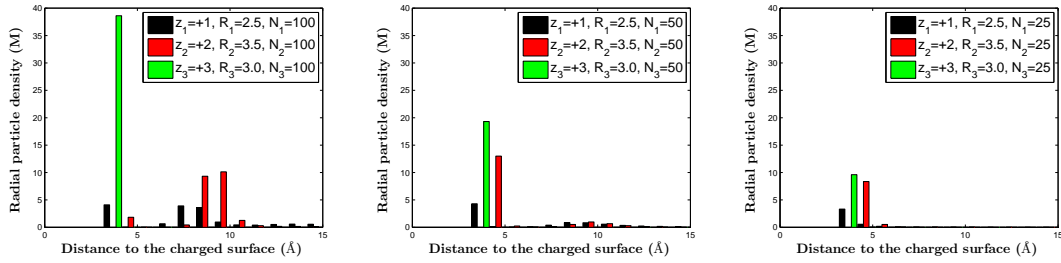


Figure 2.3: The histograms of radial particle density functions for three species of counterions in Group 2: $\alpha_{+1} : \alpha_{+2} : \alpha_{+3} = 1.4 : 1 : 2.4$.

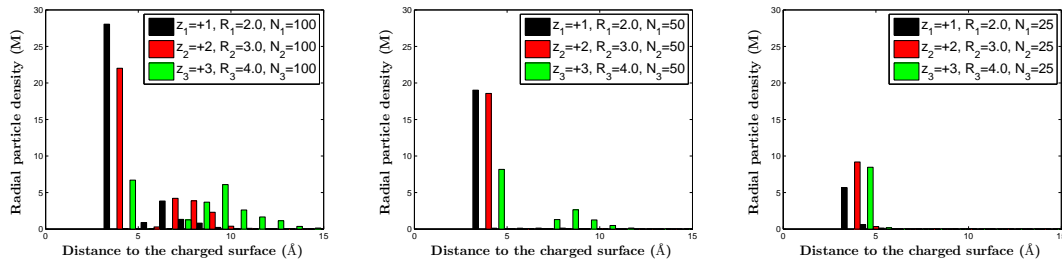


Figure 2.4: The histograms of radial particle density functions for three species of counterions in Group 2: $\alpha_{+1} : \alpha_{+2} : \alpha_{+3} = 2.7 : 1.6 : 1$.

In Figure 2.5, we plot the concentrations of the three counterion species with parameters in Group 1 predicted by our mean-field theory with the nonuniform size effect and our constrained optimization methods. The number of ions in each system are $N_1 = N_2 = N_3 = 100$ (left), 50 (middle), and 25 (right), respectively.

Comparing these results with those in Figure 2.2, we find a qualitative agreement of our size-effect included mean-field theory with the MC simulations. We note that the peaks of ionic densities close to the surface predicted by the MC simulations have a larger magnitude and are closer to the surface than those predicted by the mean-field theory.

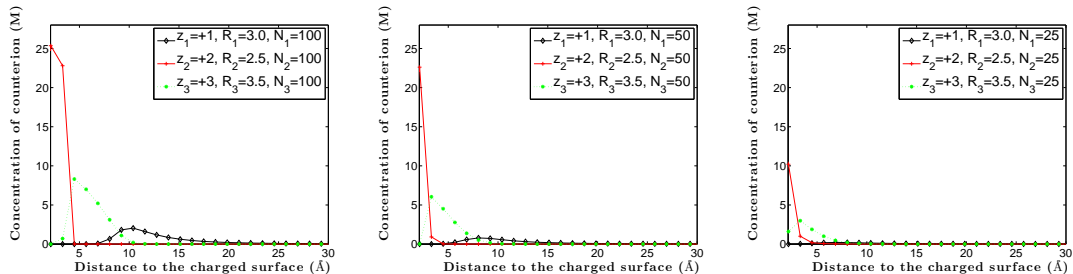


Figure 2.5: Mean-field predictions of concentrations of counterions in Group 1: $\alpha_{+1} : \alpha_{+2} : \alpha_{+3} = 1 : 3.5 : 1.9$.

We now investigate the sensitivity of the ionic sizes with respect to the ionic structure in the vicinity of charged surface. We fix the surface charge density to be $\sigma = -0.22e/\text{\AA}^2$. We consider three species of counterions with valences $z_i = +i$ ($i = 1, 2, 3$) and number of ions $N_1 = N_2 = N_3 = 100$. In Figure 2.6, we plot the ionic densities for various combinations of the ionic radii R_1 , R_2 , and R_3 . The radius of the trivalent counterion is decreased from 4 Å in Figure 2.6 (left) to 3.5 Å in Figure 2.6 (middle) so that the divalent and trivalent species have almost the same valence-to-volume ratio. The radius of the monovalent ion is decreased from 2 Å in Figure 2.6 (middle) to 1.5 Å in Figure 2.6 (right). In both cases, the species with the highest valence-to-volume ratio, i.e. the monovalent ionic species, remains the strongest in the competition to form the first layer closest to the charged surface. This indicates that the ionic competitive ability in adsorption is greatly improved by a slight decrease of its radius, which weakens the ionic entropic repulsion. From Figure 2.6 (middle), we also find that when two species of counterions have close values of valence-to-volume ratios, the species with a higher valence will have a stronger ability of adsorption. The valence-to-volume ratios in the three systems in Figure 2.6 are: (Left) $\alpha_{+1} : \alpha_{+2} : \alpha_{+3} = 2.7 : 1.6 : 1$;

(Middle) $\alpha_{+1} : \alpha_{+2} : \alpha_{+3} = 1.8 : 1.1 : 1$; (Right) $\alpha_{+1} : \alpha_{+2} : \alpha_{+3} = 6.3 : 1.6 : 1$.

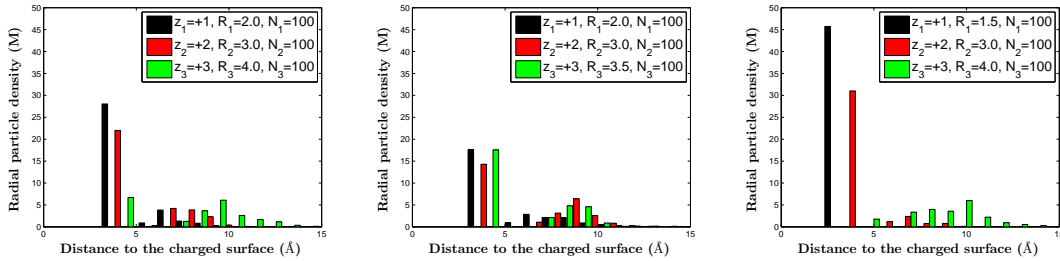


Figure 2.6: The layering structure of ionic densities is very sensitive to the variation of the ionic radius of one ionic species.

Figure 2.6 (right) also illustrates an interesting phenomenon. With the decrease of the radius of monovalent ions, the concentration of the divalent ions, which have the second largest of the three valence-to-volume ratios, is increased. The trivalent ions which have the smallest valence-to-volume ratio are depleted in the vicinity of the surface. This can be interpreted that the more tightly binding of the monovalent ions to the surface decreases more the electrostatic energy contributed by divalent and trivalent ions. The effect of the valence-to-volume ratio is strengthened in the competition between the latter two species. This result demonstrates that the nonuniform ionic size effect plays a very important role in determining the properties of electrolyte solutions.

We now fix the numbers of ions $N_1 = N_2 = N_3 = 100$, the surface charge density $\sigma = -0.21e/\text{\AA}^2$, the ratios of radii $R_1 : R_2 : R_3 = 2 : 3 : 4$, and the order of valence-to-volume ratios $\alpha_{+1} > \alpha_{+2} > \alpha_{+3}$. We vary simultaneously the ionic radii of the three species of counterions by changing a common multiplier. We use three different sets with the radii of monovalent ions being 1.2, 2.0, and 2.4 Å, respectively. We study how the different ionic sizes affect the layering structure of counterions and how the competition in ionic adsorption is changed with the change of entropy. The corresponding results are plotted in Figure 2.7. It can be found that, with the increase of the ionic radii, the entropic contribution to the electrostatic free energy is increased, leading to the enhancement of the counterion repulsion. Moreover, the particle numbers of all the three ionic species in the

layers closest to the surface are diminished. In the meantime, when ionic sizes are increased from small to large, the entropic contribution to the free energy becomes more significant. Hence, the valence-to-volume ratios give a clear characterization of stratification. In fact, the monovalent counterions, which has the smallest value of valence but largest valence-to-volume ratio, always forms the first layer closest to the surface. It is a further evidence that the competition between electrostatic energetics and entropy leads to the following limits: at the limit of the electrostatics domination the valence is the main indicator of the ordering of layers, while at the limit of the entropy domination the valence-to-volume ratio is the main indicator of layer ordering.

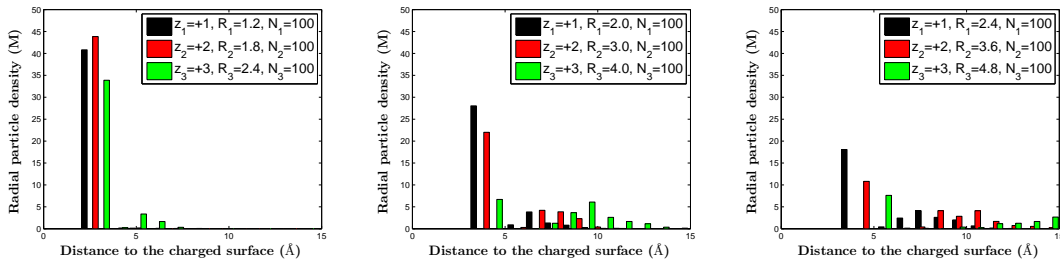


Figure 2.7: Results of varying the ionic radii of the three species with a common factor.

2.4.2 Systems with both counterions and coions

We now add coions in the system and study the effect of coions to the competitive adsorption and order of packing of counterions, in comparison with the salt-free systems. We consider two cases. In the first case, we add monovalent coions to the system. We assume that the radius of such a coion is $R_4 = 2 \text{ \AA}$ and that the total number of coions is $N_4 = 204$. In the second case, we add divalent coions to the system. We assume that the radius of such a divalent coion is $R_4 = 2 \text{ \AA}$ and that the total number of such coions is $N_4 = 102$. In both cases, we still have the monovalent, divalent, and trivalent counterions, with now their radii 2, 3, and 4 \AA , respectively, and their total numbers $N_1 = N_2 = N_3 = 134$. We also assume a high surface charge density $\sigma = -0.21 e/\text{\AA}^2$. The charge neutrality

(2.1) is now satisfied with $M = 4$ species of counterions and coions. The system will have an averaged 100 mM concentration of monovalent coions in the first case and 50 mM concentration of divalent coions in the second case.

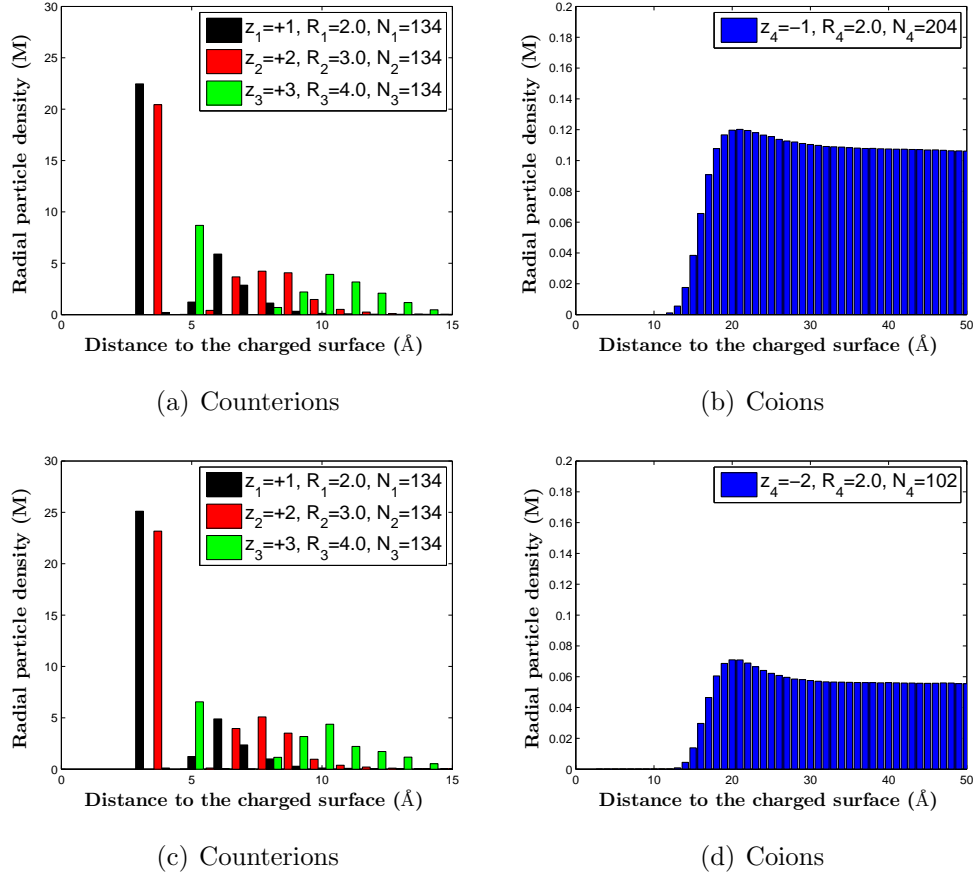


Figure 2.8: Counterion and coion distributions from MC simulations. Top: monovalent coions. Bottom: divalent coions.

For these two systems with coions, we plot in Figure 2.8 the radial particle density functions of counterions and coions obtained by our MC simulations. We also plot the concentrations of counterions and coions obtained by our mean-field numerical computations in Figure 2.9. In comparison with those salt free systems, we find that the addition of coions slightly enhances the layering effect. The concentrations of all three counterions are increased. This has a minor influence to their layering order. It is clear that a qualitative agreement between mean-field calculations and MC simulations is reached on the competition of counterion

adsorption.

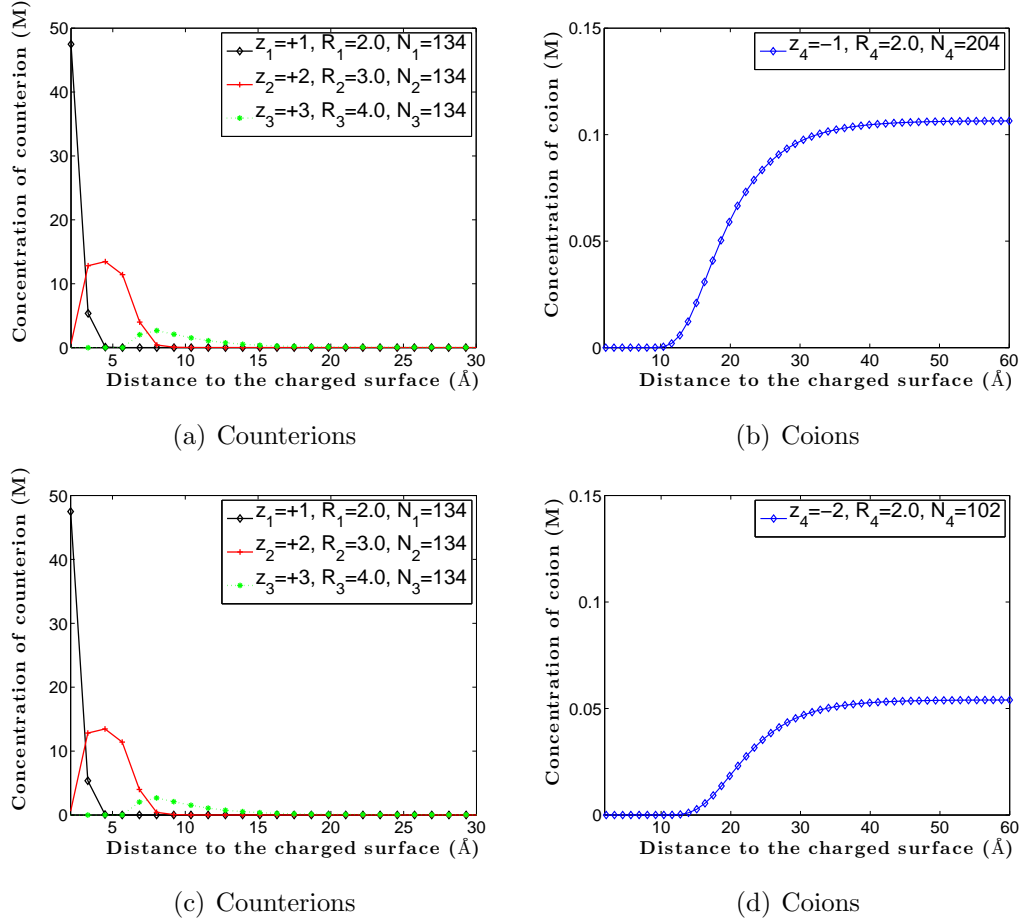


Figure 2.9: Counterion and coion concentrations from numerical computations based on the mean-field theory with the ionic size effect. Top: monovalent coions. Bottom: divalent coions.

We observe from Figure 2.8 (b) and (d) that the coion distribution predicted by MC simulations is non-monotonic, while from Figure 2.9 (b) and (d) that the coion distributions predicted by the mean-field theory is monotonic. In Figure 2.10, we plot the total ionic charge distribution for each of the two systems obtained by our MC simulations. We find the over-charging of the system, i.e., the total charge distribution is above zero that corresponds to the charge neutrality [GNS02, QPGTMM⁺03]. Interestingly, the over-charging of the monovalent-coion system is stronger than that in the divalent-coion system: the inverted

charges of the monovalent-coion system and divalent-coion system are 1.86 e and 0.15 e, respectively. This is mainly due to the fact that it is easier to form anion-cation binding pairs in the divalent-coion system than in the monovalent-coion system. Thus the concentration of free counterions is decreased. In contrast, the mean-field theory can only produce a monotonic profile of the total charge distribution as proved mathematically in [Li09a]. Therefore, the mean-field theory with the nonuniform size effect still fails in predicting the charge inversion.

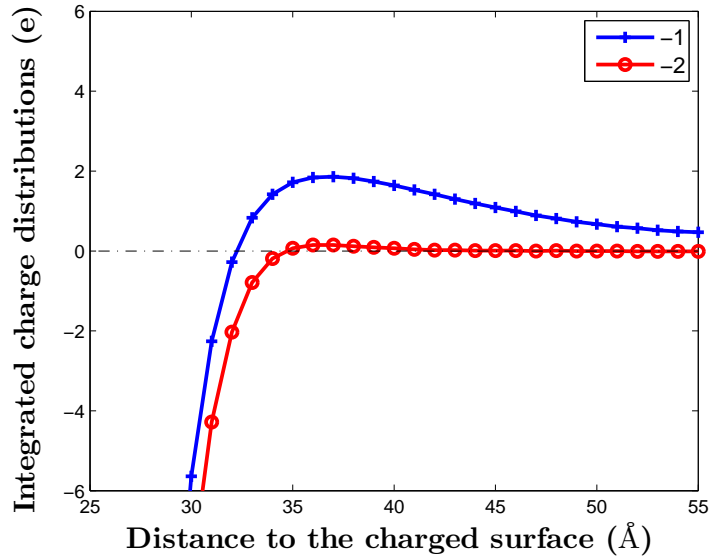


Figure 2.10: MC simulations of the total charge distribution for the system with monovalent coions (marked -1) and that with divalent coions (marked -2).

2.5 Remarks

In this part, we study the competition of multiple counterions of different valences and different sizes in binding to the surface of a spherical colloidal particle by both a mean-field theory and Monte Carlo (MC) simulations.

Based on our MC simulations and mean-field computations, we have found that the major factor which will effect the counterion stratification phenomena are surface charge density, difference of ionic valence-to-volume ratios and ionic size. Additionally, our MC simulations predict the charge inversion for ionic systems

with salt, but mean-field theory fails in predicting this phenomenon.

In our mean-field computations, we have never found a case where our criterion of valence-to-volume ratios fails for the prediction of stratification of multiple counterions. For MC simulations, we sometimes find the criterion does not work, when those ratios are too close and the surface charge is too low. In fact, the MC simulation reported in Figure 6 (b) of [TSYT05] for a low surface charge density contradicts our criterion.

While our mean-field theory and Monte Carlo simulations have both predicted the stratification of counterions near a highly charged surface and the crucial role of the ionic valence-to-volume ratios in such stratification, we have neglected several effects in our theory and methods.

First, in our MC simulations, we treat ions as hard spheres to describe the short-range repulsion in the van der Waals interactions between different kinds of ions of multiple valences and different sizes, and between the ions and the charged macroion. We have neglected the long-range attraction in such interactions that can contribute largely to the ion-ion correlations. For a highly charged surfaces, counterions are crowded near the surface; and the van der Waals attraction may not be as strong as the corresponding repulsion. While we have taken a rather common approach in MC simulations, we understand that including the attraction part of the van der Waals interactions is practically quite possible. We shall include such interaction in our subsequent works.

Second, in both of our mean-field treatment and MC simulations, we use a uniform dielectric coefficient for the ionic solution. This is only an approximation in the description of the dielectric properties of solvent, as the water in the proximity of a highly charged surface is not expected to behave like bulk solvent. In fact, the dielectric coefficient can depend on the ionic concentrations [EW54, HPP10, KSD11]. Such dependence is experimentally known to be continuous and linear; cf. Eq. (1) and Table 1 in [BYAP11]. Near the charged surface the dielectric coefficient is locally close to a constant; and the ion-ion interactions in such a region can be still modeled well by our interaction energy (2.19) but with a dielectric coefficient different from that in the bulk. We thus do not expect that this will significantly

affect the competition of different counterions in the stratification. To further explore the detailed consequences of the concentration dependent dielectrics, we are currently extending our work to such dielectric systems.

Third, the size effect of solvent molecules is not directly included in our MC simulations. This makes our comparison between the mean-field theory and MC simulations only qualitative. There is clearly a need to develop models and algorithms to include the solvent molecular size effect in MC simulations of electrolyte systems.

Acknowledgements

Chapter 2, in part is taken from the material as it appears in *Competitive adsorption and ordered packing of counterions near highly charged surfaces: From mean-field theory to Monte Carlo simulations* by J. Wen, S. Zhou, Z. Xu, and B. Li, published in Physical Review E 85 (4), 041406, 2011.

Chapter 3

Mean-Field Theory and Computation of Electrostatics with Ionic Concentration Dependent Dielectrics

3.1 Introduction

A basic hypothesis in the continuum modeling of electrostatic interactions in charged molecular systems is that such a system can be treated as a dielectric medium characterized by its dielectric coefficient that can vary spatially. Under normal conditions, the dielectric coefficient for water is close to 80, while that for proteins can be as low as 1 – 4 [Has73, HRC48]. Experiment and molecular dynamics (MD) simulations have indicated that the dielectric coefficient can depend on the local ionic concentrations [Has73, RDZ⁺14, WS90, WCS92, KD09, SGM10, HRC48, Sch27, Lat21, DN84, LZ98, NHK97, BHB94, BHM99]. In this part of the dissertation, I use a mean-field variational approach to study how such dependence affects the equilibrium properties of electrostatic interactions in an ionic solution.

Consider an ionic solution near a charged surface. Assume there are M ionic species in the solution. (Typically $1 \leq M \leq 4$.) Denote by $c_i = c_i(x)$ the

local ionic concentration of the i th species at a spatial point x . The key modeling assumption is that the dielectric coefficient ε depends on the sum of local ionic concentrations of all individual ionic (either cationic or anionic) species: $\varepsilon = \varepsilon(\bar{c}(x))$, where $\bar{c} = \sum_{i=1}^M c_i$. This dependence is qualitatively the same as that on the salt concentration. The latter can be constructed by fitting experimental or MD simulations data. The dependence of the dielectric coefficient on the concentration of NaCl [HRC48,LZ98] and the fitted analytic form of such dependence are shown in Figure 1.4. We use $\varepsilon(\bar{c}) = 70e^{-0.22\bar{c}} + 10$ to fit the experimental data in this figure, and the maximum relative error at data points is 2%. In general, we assume that the function $\varepsilon = \varepsilon(\bar{c})$ is monotonically decreasing, convex, and is bounded below by a positive constant. Examples of such a function $\varepsilon = \varepsilon(\bar{c})$ are

$$\varepsilon(\bar{c}) = \frac{\alpha_0 - \alpha_1}{1 + \xi \bar{c}} + \alpha_1 \quad \text{and} \quad \varepsilon(\bar{c}) = (\alpha_0 - \alpha_1)e^{-\xi \bar{c}} + \alpha_1,$$

where all α_0 , α_1 , and ξ are constant parameters fitting experimental or MD simulations data with $\alpha_0 > \alpha_1 > 0$. Note that $\varepsilon(0) = \alpha_0$ and $\varepsilon(\infty) = \alpha_1$. We remark that the choice of \bar{c} instead of salt concentration reflects our attempt in understanding the contribution of each individual ionic species through its concentration to the dielectric environment, as biological properties are often ion specific (e.g., the ion selectivity in ion channels). Using $\bar{c} = \sum_{i=1}^M c_i$ allows us to input the concentration of each individual ionic species, and also to determine the variation of the free energy with respect to such individual ionic species.

The dielectric coefficient measures the polarizability of a material exposed to an external electric field. Due to their asymmetric structures, water molecules form permanent dipoles. They orient randomly in the bulk due to thermal fluctuations. Such orientational polarization makes the bulk water a strong dielectric medium. In the proximity of charged particles such as ions (cations or anions), however, water molecules are attracted by the charges, forming a hydration shell. These dipolar water molecules in the shell are aligned to the local electric field. Such saturation of local orientational polarizability leads to a weaker dielectric response of water near charges to the external electric field. Consequently, the dielectric coefficient in a region of high ionic concentrations is expected to be smaller than that in a region of lower ionic concentrations [HRC48, WS90, BYAP11, Fry11, DDP12].

This dielectric decrement is one of the main properties of electrostatic interactions that we study here.

We now let the ionic solution occupy a bounded domain Ω in \mathbb{R}^3 with a smooth boundary $\partial\Omega$. We assume that the boundary $\partial\Omega$ of Ω is divided into two nonempty, disjoint, and smooth parts Γ_D (D for Dirichlet) and Γ_N (N for Neumann); cf. Figure 3.1. (The case that $\Gamma_D = \emptyset$, i.e., $\Gamma = \Gamma_N$, can be treated similarly.) In Figure 3.1, small circles with plus and minus signs represent cations (positively charged ions) and anions (negatively charged ions), respectively. We also assume that we are given a fixed charged density $\rho_f : \Omega \rightarrow \mathbb{R}$, a surface charge density $\sigma : \Gamma_N \rightarrow \mathbb{R}$, and a boundary value of the electrostatic potential $\psi_\infty : \Gamma_D \rightarrow \mathbb{R}$. We consider minimizing the following mean-field electrostatic free-energy functional of the ionic concentrations $c = (c_1, \dots, c_M)$ [Li09b, CDLM08, RR90, FB97, ODRY09]:

$$F[c] = \int_{\Omega} \frac{1}{2} \rho(c) \psi(c) dV + \int_{\Gamma_N} \frac{1}{2} \sigma \psi(c) dS + \beta^{-1} \sum_{i=1}^M \int_{\Omega} c_i [\log(\Lambda^3 c_i) - 1] dV - \sum_{i=1}^M \mu_i \int_{\Omega} c_i dV. \quad (3.1)$$

Here, the first two terms together represent the electrostatic potential energy. In these terms, $\rho(c)$ is the total charge density, defined by

$$\rho(c) = \rho_f + \sum_{i=1}^M q_i c_i, \quad (3.2)$$

where $q_i = z_i e$ with z_i the valence of the i th ionic species and e the elementary charge, and $\psi = \psi(c)$ is the electrostatic potential determined as the solution to the boundary-value problem of Poisson's equation [Jac99, LLP93, BYAP11]

$$\begin{cases} \nabla \cdot \varepsilon(\bar{c}) \varepsilon_0 \nabla \psi = -\rho(c) & \text{in } \Omega, \\ \varepsilon(\bar{c}) \varepsilon_0 \frac{\partial \psi}{\partial n} = \sigma & \text{on } \Gamma_N, \\ \psi = \psi_\infty & \text{on } \Gamma_D, \end{cases} \quad (3.3)$$

where ε_0 is the vacuum permittivity and $\partial\psi/\partial n$ denotes the normal derivative at Γ with n the exterior unit normal. The third term in (3.1) represents the ionic

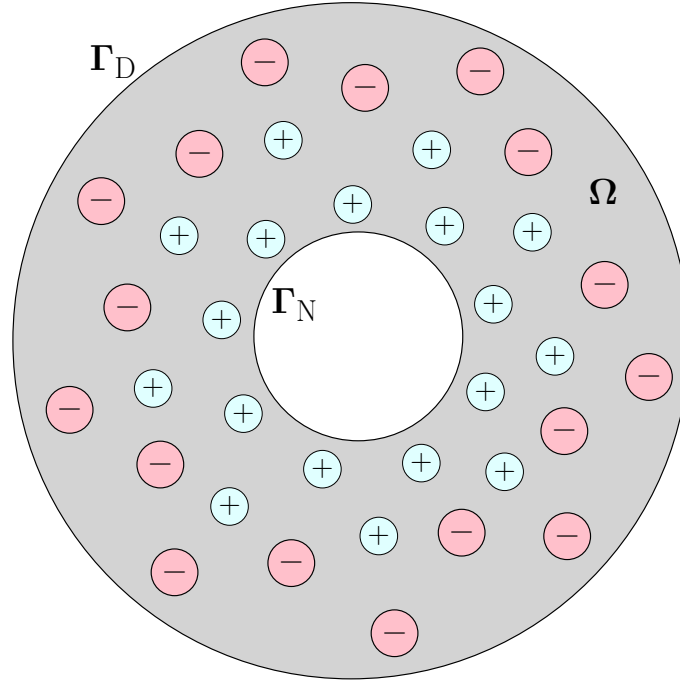


Figure 3.1: A schematic view of an ionic solution. The solvent occupies the grey region Ω .

ideal-gas entropy, where $\beta^{-1} = k_B T$ with k_B the Boltzmann constant and T the absolute temperature, \log denotes the natural logarithm, and Λ is the thermal de Broglie wavelength. The last term in (3.1), in which μ_i is the chemical potential for the i th ionic species, represents the chemical potential of the system that results from the constraint of total number of ions in each species.

The rest of the chapter is organized as follows: In Section 3.2, I derive the first variations of the free-energy functional and the generalized Boltzmann distributions. In Section 3.3, I derive the second variations of the free-energy functional. In Section 3.4, I show by numerical calculations that the generalized Boltzmann distributions can lead to multiple values of concentrations. I also show by examples that the free-energy functional is in general nonconvex. In Section 3.5, I minimize numerically the mean-field electrostatic free-energy functional for a radially symmetric system. Finally, in Section 3.6, I make several remarks.

3.2 First Variations and Generalized Boltzmann Distributions

Unless otherwise stated, we assume the following throughout the rest of the paper:

(A1) The dielectric coefficient function $\varepsilon \in C^1([0, \infty))$. It decreases monotonically and is convex. Moreover, there are two positive numbers ε_{\min} and ε_{\max} such that

$$\varepsilon_{\min} \leq \varepsilon(\bar{c}) \leq \varepsilon_{\max} \quad \forall \bar{c} \geq 0; \quad (3.4)$$

(A2) The set $\Omega \subset \mathbb{R}^3$ is bounded, open, and connected with a smooth boundary $\Gamma = \partial\Omega$ (e.g., Γ is in the class C^2). The boundary $\partial\Omega$ is divided into two disjoint, nonempty, and smooth (e.g., in the class of C^2) parts Γ_D and Γ_N ;

(A3) The functions $\rho_f : \Omega \rightarrow \mathbb{R}$, $\sigma : \Gamma_N \rightarrow \mathbb{R}$, and $\psi_\infty : \Gamma_D \rightarrow \mathbb{R}$ are all given. Moreover, $\rho_f \in L^\infty(\Omega)$, σ is the restriction of a $W^{1,\infty}(\Omega)$ -function (also denoted by σ) on Γ_N , and ψ_∞ is the restriction of a $W^{2,\infty}(\Omega)$ -function (also denoted by ψ_∞) on Γ_D .

Note that we use standard notion for Sobolev spaces [Ada75, GT98, Eva10].

We denote

$$\begin{aligned} H_{D,0}^1(\Omega) &= \{ \phi \in H^1(\Omega) : \phi = 0 \text{ on } \Gamma_D \}, \\ H_D^1(\Omega) &= \{ \phi \in H^1(\Omega) : \phi = \psi_\infty \text{ on } \Gamma_D \}. \end{aligned}$$

Let $u \in L^1(\Omega)$. Suppose

$$\|u\| := \sup_{0 \neq \phi \in L^\infty(\Omega) \cap H_{D,0}^1(\Omega)} \frac{1}{\|\phi\|_{H^1(\Omega)}} \int_{\Omega} u\phi \, dV < \infty.$$

Since $L^\infty(\Omega) \cap H_{D,0}^1(\Omega)$ is dense in $H_{D,0}^1(\Omega)$, we can identify u as an element in $H_{D,0}^{-1}(\Omega)$, the dual space of $H_{D,0}^1(\Omega)$, and write $u \in H_{D,0}^{-1}(\Omega)$. We denote

$$X = \left\{ (c_1, \dots, c_M) \in L^1(\Omega, \mathbb{R}^M) : c_i \geq 0 \text{ a.e.}, i = 1, \dots, M; \sum_{i=1}^M q_i c_i \in H_{D,0}^{-1}(\Omega) \right\}.$$

Let $c = (c_1, \dots, c_M) \in X$. It follows from the Lax–Milgram Lemma and the Poincaré inequality for functions in $H_{D,0}^1(\Omega)$ [GT98, Eva10] that the boundary-value problem of Poisson’s equation (3.3) has a unique weak solution $\psi = \psi(c)$,

defined by $\psi \in H_D^1(\Omega)$ and

$$\int_{\Omega} \varepsilon(\bar{c}) \varepsilon_0 \nabla \psi \cdot \nabla \phi \, dV = \int_{\Omega} \rho(c) \phi \, dV + \int_{\Gamma_N} \sigma \phi \, dS \quad \forall \phi \in H_{D,0}^1(\Omega). \quad (3.5)$$

Similarly, we define $\psi_D = \psi_D(c) \in H_D^1(\Omega)$ to be the unique weak solution to

$$\begin{cases} \nabla \cdot \varepsilon(\bar{c}) \varepsilon_0 \nabla \psi_D = 0 & \text{in } \Omega, \\ \varepsilon(\bar{c}) \varepsilon_0 \frac{\partial \psi_D}{\partial n} = 0 & \text{on } \Gamma_N, \\ \psi_D = \psi_{\infty} & \text{on } \Gamma_D, \end{cases} \quad (3.6)$$

defined by $\psi_D \in H_D^1(\Omega)$ and

$$\int_{\Omega} \varepsilon(\bar{c}) \varepsilon_0 \nabla \psi_D \cdot \nabla \phi \, dV = 0 \quad \forall \phi \in H_{D,0}^1(\Omega). \quad (3.7)$$

3.2.1 First variations

Let $c = (c_1, \dots, c_M) \in X$ and $d = (d_1, \dots, d_M) \in X$. We define

$$\delta F[c][d] = \lim_{t \rightarrow 0} \frac{F[c + td] - F[c]}{t}, \quad (3.8)$$

if $c + td \in X$ for $|t| \ll 1$ and the limit exists, and call it the first variation of $F[\cdot]$ at $c \in X$ in the direction d .

Theorem 3.2.1. *Let $c = (c_1, \dots, c_M) \in X$. Assume there exist positive numbers δ_1 and δ_2 such that $\delta_1 \leq c_i(x) \leq \delta_2$ for a.e. $x \in \Omega$ and $i = 1, \dots, M$. Assume also that $d = (d_1, \dots, d_M) \in L^\infty(\Omega, \mathbb{R}^M)$. Then*

$$\delta F[c][d] = \sum_{i=1}^M \int_{\Omega} d_i \delta_i F[c] \, dV,$$

where for each i ($1 \leq i \leq M$) the function $\delta_i F[c] : \Omega \rightarrow \mathbb{R}$ is given by

$$\begin{aligned} \delta_i F[c] = & q_i \left[\psi(c) - \frac{1}{2} \psi_D(c) \right] - \frac{1}{2} \varepsilon'(\bar{c}) \varepsilon_0 \nabla \psi(c) \cdot \nabla [\psi(c) - \psi_D(c)] \\ & + \beta^{-1} \log(\Lambda^3 c_i) - \mu_i. \end{aligned} \quad (3.9)$$

We shall identify $\delta_i F[c]$ defined in (3.9) as the the first variation of F at c in the i th coordinate direction. We note that our assumptions on $c_i(x)$ ($i =$

$1, \dots, M, x \in \Omega$) are expected to hold true for a local minimizer $c = (c_1, \dots, c_M)$. This can be argued using the same analysis in [Li09b, Li09a], where perturbed, lower energy concentrations are constructed for the usual PB free-energy functional, based on the observation that the entropic change is larger than the potential change. To prove the theorem, we first prove the following:

Lemma 3.2.2. *Under the assumption of Theorem 3.2.1, we have*

$$\|\psi(c + td) - \psi(c)\|_{H^1(\Omega)} \rightarrow 0 \quad \text{and} \quad \|\psi_{\text{D}}(c + td) - \psi_{\text{D}}(c)\|_{H^1(\Omega)} \rightarrow 0 \quad \text{as } t \rightarrow 0.$$

Proof. Denote $\bar{d} = \sum_{i=1}^M d_i$. By the weak formulations for $\psi(c + td)$ and $\psi(c)$ (cf. (3.5)), and the definition of $\rho(c)$ (cf. (3.2)), we have for $\phi \in H_{\text{D},0}^1(\Omega)$ that

$$\begin{aligned} & \int_{\Omega} [\varepsilon(\bar{c} + t\bar{d}) - \varepsilon(\bar{c})] \varepsilon_0 \nabla \psi(c + td) \cdot \nabla \phi \, dV \\ & + \int_{\Omega} \varepsilon(\bar{c}) \varepsilon_0 \nabla [\psi(c + td) - \psi(c)] \cdot \nabla \phi \, dV \\ & = \int_{\Omega} \varepsilon(\bar{c} + t\bar{d}) \varepsilon_0 \nabla \psi(c + td) \cdot \nabla \phi \, dV - \int_{\Omega} \varepsilon(\bar{c}) \varepsilon_0 \nabla \psi(c) \cdot \nabla \phi \, dV \\ & = \int_{\Omega} [\rho(c + td) - \rho(c)] \phi \, dV \\ & = t \sum_{i=1}^M \int_{\Omega} q_i d_i \phi \, dV. \end{aligned}$$

Setting $\phi = \phi_t := \psi(c + td) - \psi(c) \in H_{\text{D},0}^1(\Omega)$, we then have by (3.4) that

$$\begin{aligned} & \varepsilon_{\min} \varepsilon_0 \int_{\Omega} |\nabla \phi_t|^2 \, dV \\ & \leq \int_{\Omega} \varepsilon(\bar{c}) \varepsilon_0 |\nabla \phi_t|^2 \, dV \\ & = t \sum_{i=1}^M \int_{\Omega} q_i d_i \phi_t \, dV - \int_{\Omega} [\varepsilon(\bar{c} + t\bar{d}) - \varepsilon(\bar{c})] \varepsilon_0 \nabla \psi(c + td) \cdot \nabla \phi_t \, dV \\ & = t \sum_{i=1}^M \int_{\Omega} q_i d_i \phi_t \, dV - \int_{\Omega} [\varepsilon(\bar{c} + t\bar{d}) - \varepsilon(\bar{c})] \varepsilon_0 |\nabla \phi_t|^2 \, dV \\ & \quad - \int_{\Omega} [\varepsilon(\bar{c} + t\bar{d}) - \varepsilon(\bar{c})] \varepsilon_0 \nabla \psi(c) \cdot \nabla \phi_t \, dV \\ & \leq |t| \left(\sum_{i=1}^M |q_i| \|d_i\|_{L^2(\Omega)} \right) \|\phi_t\|_{L^2(\Omega)} + \varepsilon_0 \|\varepsilon(\bar{c} + t\bar{d}) - \varepsilon(\bar{c})\|_{L^\infty(\Omega)} \|\nabla \phi_t\|_{L^2(\Omega)}^2 \end{aligned}$$

$$+ \varepsilon_0 \|\varepsilon(\bar{c} + t\bar{d}) - \varepsilon(\bar{c})\|_{L^\infty(\Omega)} \|\nabla \psi(c)\|_{L^2(\Omega)} \|\nabla \phi_t\|_{L^2(\Omega)}.$$

Since $\|\varepsilon(\bar{c} + t\bar{d}) - \varepsilon(\bar{c})\|_{L^\infty(\Omega)} \rightarrow 0$ as $t \rightarrow 0$, we conclude by the Poincaré inequality applied to ϕ_t that there exists a constant $C > 0$ independent of t with $|t| \ll 1$ such that

$$\|\phi_t\|_{H^1(\Omega)} \leq C(|t| + \varepsilon_0 \|\varepsilon(\bar{c} + t\bar{d}) - \varepsilon(\bar{c})\|_{L^\infty(\Omega)}) \rightarrow 0 \quad \text{as } t \rightarrow 0.$$

This proves that $\|\psi(c + td) - \psi(c)\|_{H^1(\Omega)} \rightarrow 0$ as $t \rightarrow 0$. The proof of the convergence $\|\psi_D(c + td) - \psi_D(c)\|_{H^1(\Omega)} \rightarrow 0$ as $t \rightarrow 0$ is similar and simpler. \square

Proof of Theorem 3.2.1. Let us write $F[c] = F_{\text{pot}}[c] + F_{\text{ent}}[c]$, where

$$F_{\text{pot}}[c] = \int_{\Omega} \frac{1}{2} \rho(c) \psi(c) dV + \int_{\Gamma_N} \frac{1}{2} \sigma \psi(c) dS, \quad (3.10)$$

$$F_{\text{ent}}[c] = \sum_{i=1}^M \int_{\Omega} \{\beta^{-1} c_i [\log(\Lambda^3 c_i) - 1] - \mu_i c_i\} dV. \quad (3.11)$$

By routine calculations (cf. [Li09a, Li09b, CDLM08]), we have

$$\delta F_{\text{ent}}[c][d] = \lim_{t \rightarrow 0} \frac{F_{\text{ent}}[c + td] - F_{\text{ent}}[c]}{t} = \sum_{i=1}^M \int_{\Omega} d_i [\beta^{-1} \log(\Lambda^3 c_i) - \mu_i] dV. \quad (3.12)$$

Now we have by (3.2) that for $|t| \ll 1$

$$\begin{aligned} & \frac{F_{\text{pot}}[c + td] - F_{\text{pot}}[c]}{t} \\ &= \frac{1}{2} \int_{\Omega} \frac{\rho(c + td) \psi(c + td) - \rho(c) \psi(c)}{t} dV + \frac{1}{2} \int_{\Gamma_N} \sigma \frac{\psi(c + td) - \psi(c)}{t} dS \\ &= \frac{1}{2} \int_{\Omega} \frac{[\rho(c + td) - \rho(c)] \psi(c + td)}{t} dV + \frac{1}{2} \int_{\Omega} \rho(c) \frac{\psi(c + td) - \psi(c)}{t} dV \\ &\quad + \frac{1}{2} \int_{\Gamma_N} \sigma \frac{\psi(c + td) - \psi(c)}{t} dS \\ &= \frac{1}{2} \sum_{i=1}^M \int_{\Omega} q_i d_i \psi(c + td) dV + \frac{1}{2} \int_{\Omega} \rho(c) \frac{\psi(c + td) - \psi(c)}{t} dV \\ &\quad + \frac{1}{2} \int_{\Gamma_N} \sigma \frac{\psi(c + td) - \psi(c)}{t} dS. \end{aligned} \quad (3.13)$$

By Lemma 3.2.2, we have

$$\frac{1}{2} \sum_{i=1}^M \int_{\Omega} q_i d_i \psi(c + td) dV \rightarrow \frac{1}{2} \sum_{i=1}^M \int_{\Omega} q_i d_i \psi(c) dV \quad \text{as } t \rightarrow 0. \quad (3.14)$$

For the remaining two terms in (3.13), we have by the weak formulation (3.5) for $\psi(c)$ and (3.7) for $\psi_{\mathbb{D}}(c)$ with $\phi = [\psi(c + td) - \psi(c)]/t$ that

$$\begin{aligned} & \frac{1}{2} \int_{\Omega} \rho(c) \frac{\psi(c + td) - \psi(c)}{t} dV + \frac{1}{2} \int_{\Gamma_{\mathbb{N}}} \sigma \frac{\psi(c + td) - \psi(c)}{t} dS \\ &= \frac{1}{2} \int_{\Omega} \varepsilon(\bar{c}) \varepsilon_0 \nabla \psi(c) \cdot \nabla \left[\frac{\psi(c + td) - \psi(c)}{t} \right] dV \\ &= \frac{1}{2} \int_{\Omega} \varepsilon(\bar{c}) \varepsilon_0 \nabla [\psi(c) - \psi_{\mathbb{D}}(c)] \cdot \nabla \left[\frac{\psi(c + td) - \psi(c)}{t} \right] dV. \end{aligned} \quad (3.15)$$

It now follows from the weak formulations for $\psi(c + td)$ and $\psi(c)$ (cf. (3.5)) with $\phi = \psi(c) - \psi_{\mathbb{D}}(c)$, and Lemma 3.2.2 that

$$\begin{aligned} & \frac{1}{2} \int_{\Omega} \varepsilon(\bar{c}) \varepsilon_0 \nabla [\psi(c) - \psi_{\mathbb{D}}(c)] \cdot \nabla \left[\frac{\psi(c + td) - \psi(c)}{t} \right] dV \\ &= \frac{1}{2t} \int_{\Omega} [\varepsilon(\bar{c}) - \varepsilon(\bar{c} + t\bar{d})] \varepsilon_0 \nabla [\psi(c) - \psi_{\mathbb{D}}(c)] \cdot \nabla \psi(c + td) dV \\ &+ \frac{1}{2t} \int_{\Omega} \varepsilon(\bar{c} + t\bar{d}) \varepsilon_0 \nabla [\psi(c) - \psi_{\mathbb{D}}(c)] \cdot \nabla \psi(c + td) dV \\ &- \frac{1}{2t} \int_{\Omega} \varepsilon(\bar{c}) \varepsilon_0 \nabla [\psi(c) - \psi_{\mathbb{D}}(c)] \cdot \nabla \psi(c) dV \\ &= -\frac{1}{2} \int_{\Omega} \frac{\varepsilon(\bar{c} + t\bar{d}) - \varepsilon(\bar{c})}{t} \varepsilon_0 \nabla [\psi(c) - \psi_{\mathbb{D}}(c)] \cdot \nabla \psi(c + td) dV \\ &+ \frac{1}{2t} \int_{\Omega} \rho(c + td) [\psi(c) - \psi_{\mathbb{D}}(c)] dV - \frac{1}{2t} \int_{\Omega} \rho(c) [\psi(c) - \psi_{\mathbb{D}}(c)] dV \\ &= -\frac{1}{2} \int_{\Omega} \left[\frac{\varepsilon(\bar{c} + t\bar{d}) - \varepsilon(\bar{c})}{t} \varepsilon_0 - \sum_{i=1}^M d_i \varepsilon'(\bar{c}) \varepsilon_0 \right] \nabla [\psi(c) - \psi_{\mathbb{D}}(c)] \cdot \nabla \psi(c + td) dV \\ &- \frac{1}{2} \sum_{i=1}^M \int_{\Omega} d_i \varepsilon'(\bar{c}) \varepsilon_0 \nabla [\psi(c) - \psi_{\mathbb{D}}(c)] \cdot \nabla \psi(c + td) dV \\ &+ \frac{1}{2} \sum_{i=1}^M \int_{\Omega} d_i q_i [\psi(c) - \psi_{\mathbb{D}}(c)] dV \\ &\rightarrow -\frac{1}{2} \sum_{i=1}^M \int_{\Omega} d_i \varepsilon'(\bar{c}) \varepsilon_0 \nabla [\psi(c) - \psi_{\mathbb{D}}(c)] \cdot \nabla \psi(c) dV \\ &+ \frac{1}{2} \sum_{i=1}^M \int_{\Omega} d_i q_i [\psi(c) - \psi_{\mathbb{D}}(c)] dV \quad \text{as } t \rightarrow 0. \end{aligned}$$

This and (3.13)–(3.15) lead to

$$\delta F_{\text{pot}}[c][d] = \lim_{t \rightarrow 0} \frac{F_{\text{pot}}[c + td] - F_{\text{pot}}[c]}{t}$$

$$\begin{aligned}
&= \sum_{i=1}^M \int_{\Omega} d_i q_i \left[\psi(c) - \frac{1}{2} \psi_{\text{D}}(c) \right] dV \\
&\quad - \frac{1}{2} \sum_{i=1}^M \int_{\Omega} d_i \varepsilon'(\bar{c}) \varepsilon_0 \nabla [\psi(c) - \psi_{\text{D}}(c)] \cdot \nabla \psi(c) dV. \tag{3.16}
\end{aligned}$$

We finally combine (3.12) and (3.16) to obtain the desired first variation. \square

3.2.2 Generalized Boltzmann distributions

We call $c = (c_1, \dots, c_M) \in X$ an equilibrium if the first variation $\delta F[c][d]$ defined by (3.8) exists and is equal to 0 for any $d \in L^\infty(\Omega, \mathbb{R}^M)$. If $c = (c_1, \dots, c_M) \in X$ satisfies the assumption in Theorem 3.2.1 and is an equilibrium, then $\delta_i F[c] = 0$ ($i = 1, \dots, M$) by Theorem 3.2.1. Straightforward calculations then lead to

$$c_i = c_i^\infty \exp \left\{ -\beta \left\{ q_i \left[\psi(c) - \frac{1}{2} \psi_{\text{D}}(c) \right] - \frac{1}{2} \varepsilon'(\bar{c}) \varepsilon_0 \nabla \psi(c) \cdot \nabla [\psi(c) - \psi_{\text{D}}(c)] \right\} \right\}, \tag{3.17}$$

where $c_i^\infty = \Lambda^{-3} e^{\beta \mu_i}$ ($1 \leq i \leq M$). We call these the generalized Boltzmann distributions, as they generalize the classical Boltzmann distributions $c_i = c_i^\infty e^{-\beta q_i \psi}$ ($i = 1, \dots, M$) if ε does not depend on c , and $\psi_\infty = 0$ which implies $\psi_{\text{D}} = 0$. The effect of the boundary data was noted in [Li09b, Li09a]. Note that in general $\varepsilon'(\bar{c}) \neq 0$ and hence (3.17) does not explicitly determine how the concentrations c_i ($i = 1, \dots, M$) depend on the potential ψ .

3.3 Second Variations

Let $a, b, c \in X$. We define

$$\delta^2 F[c][a, b] = \lim_{t \rightarrow 0} \frac{\delta F[c + ta][b] - \delta F[c][b]}{t},$$

if the quotient is defined when $|t| \ll 1$ and the limit exists, and call it the second variation of the free-energy functional F at c in the directions a and b .

For $c \in X$ and $a = (a_1, \dots, a_M) \in X$, let us denote by $\Psi(c, a)$ the unique

weak solution to the boundary-value problem

$$\left\{ \begin{array}{ll} -\nabla \cdot \varepsilon(\bar{c})\varepsilon_0 \nabla \Psi(c, a) = \sum_{i=1}^M a_i [q_i + \nabla \cdot \varepsilon'(\bar{c})\varepsilon_0 \nabla \psi(c)] & \text{in } \Omega, \\ \varepsilon(\bar{c})\varepsilon_0 \frac{\partial \Psi(c, a)}{\partial n} = -\frac{\varepsilon'(\bar{c})}{\varepsilon(\bar{c})} \sigma & \text{on } \Gamma_N, \\ \Psi(c, a) = 0 & \text{on } \Gamma_D, \end{array} \right.$$

defined by $\Psi(c, a) \in H_{D,0}^1(\Omega)$ and

$$\int_{\Omega} \varepsilon(\bar{c})\varepsilon_0 \nabla \Psi(c, a) \cdot \nabla \phi \, dV = \sum_{i=1}^M \int_{\Omega} a_i [q_i \phi - \varepsilon'(\bar{c})\varepsilon_0 \nabla \psi(c) \cdot \nabla \phi] \, dV \quad \forall \phi \in H_{D,0}^1(\Omega). \quad (3.18)$$

Similarly, let us denote by $\Psi_D(c, a)$ the unique weak solution of the boundary-value problem

$$\left\{ \begin{array}{ll} -\nabla \cdot \varepsilon(\bar{c})\varepsilon_0 \nabla \Psi_D(c, a) = \sum_{i=1}^M a_i \nabla \cdot \varepsilon'(\bar{c})\varepsilon_0 \nabla \psi_D(c) & \text{in } \Omega, \\ \varepsilon(\bar{c})\varepsilon_0 \frac{\partial \Psi_D(c, a)}{\partial n} = 0 & \text{on } \Gamma_N, \\ \Psi_D(c, a) = 0 & \text{on } \Gamma_D, \end{array} \right.$$

defined by $\Psi_D(c, a) \in H_{D,0}^1(\Omega)$ and

$$\int_{\Omega} \varepsilon(\bar{c})\varepsilon_0 \nabla \Psi_D(c, a) \cdot \nabla \phi \, dV = -\sum_{i=1}^M \int_{\Omega} a_i \varepsilon'(\bar{c})\varepsilon_0 \nabla \psi_D(c) \cdot \nabla \phi \, dV \quad \forall \phi \in H_{D,0}^1(\Omega). \quad (3.19)$$

The existence and uniqueness of each of these weak solutions is guaranteed by the Lax–Milgram Lemma. Note that $\Psi(c, a)$ and $\Psi_D(c, a)$ are linear in a .

Theorem 3.3.1. *Let $\varepsilon \in C^2([0, \infty))$. Let $c = (c_1, \dots, c_M) \in X$. Assume there exist positive numbers δ_1 and δ_2 such that $\delta_1 \leq c_i(x) \leq \delta_2$ for a.e. $x \in \Omega$ and $i = 1, \dots, M$. Let $a = (a_1, \dots, a_M)$, $b = (b_1, \dots, b_M) \in L^\infty(\Omega, \mathbb{R}^M)$. We have*

$$\begin{aligned} & \delta^2 F[c][a, b] \\ &= \int_{\Omega} \left\{ \varepsilon(\bar{c})\varepsilon_0 \left[\nabla \Psi(c, b) \cdot \nabla \Psi(c, a) - \frac{1}{2} \nabla \Psi(c, b) \cdot \nabla \Psi_D(c, a) \right] \right. \end{aligned}$$

$$\left. - \frac{1}{2} \nabla \Psi_{\mathbb{D}}(c, b) \cdot \nabla \Psi(c, a) \right] - \frac{1}{2} \left(\sum_{i=1}^M b_i \right) \left(\sum_{j=1}^M a_j \right) \varepsilon''(\bar{c}) \varepsilon_0 \nabla \psi(c) \cdot \nabla [\psi(c) - \psi_{\mathbb{D}}(c)] + \sum_{i=1}^M \frac{a_i b_i}{\beta c_i} \Big\} dV.$$

Note that $\delta^2 F[c][a, b]$ is symmetric and bilinear in (a, b) . To prove this theorem, let us denote for $|t| \ll 1$

$$\Psi(c, a; t) = \frac{\psi(c + ta) - \psi(c)}{t} \quad \text{and} \quad \Psi_{\mathbb{D}}(c, a; t) = \frac{\psi_{\mathbb{D}}(c + ta) - \psi_{\mathbb{D}}(c)}{t}, \quad (3.20)$$

where $\psi(c + ta) \in H_{\mathbb{D}}^1(\Omega)$ and $\psi_{\mathbb{D}}(c + ta)$ are defined by (3.5) and (3.7), respectively, with c replaced by $c + ta$. We first prove the following:

Lemma 3.3.2. *Under the assumption of Theorem 3.3.1, we have $\Psi(c, a; t) \rightarrow \Psi(c, a)$ and $\Psi_{\mathbb{D}}(c, a; t) \rightarrow \Psi_{\mathbb{D}}(c, a)$ in $H^1(\Omega)$ as $t \rightarrow 0$.*

Proof. Consider $|t| \ll 1$. By the weak formulations for $\psi(c + ta)$ and $\psi(c)$ (cf. (3.5)) and the definition of $\rho(c + ta)$ and $\rho(c)$ (cf. (3.2)), we have for any $\phi \in H_{\mathbb{D},0}^1(\Omega)$ that

$$\int_{\Omega} \varepsilon(\bar{c} + t\bar{a}) \varepsilon_0 \nabla \psi(c + ta) \cdot \nabla \phi \, dV - \int_{\Omega} \varepsilon(\bar{c}) \varepsilon_0 \nabla \psi(c) \cdot \nabla \phi \, dV = t \sum_{i=1}^M \int_{\Omega} q_i a_i \phi \, dV.$$

With our notation $\Psi(c, a)$ and $\Psi(c, a; t)$, and the weak formulation for $\Psi(c, a)$ (cf. (3.18)), this leads to

$$\begin{aligned} & \int_{\Omega} \frac{\varepsilon(\bar{c} + t\bar{a}) - \varepsilon(\bar{c})}{t} \varepsilon_0 \nabla \psi(c + ta) \cdot \nabla \phi \, dV + \int_{\Omega} \varepsilon(\bar{c}) \varepsilon_0 \nabla [\Psi(c, a; t) - \Psi(c, a)] \cdot \nabla \phi \, dV \\ &= \sum_{i=1}^M \int_{\Omega} a_i \varepsilon'(\bar{c}) \varepsilon_0 \nabla \psi(c) \cdot \nabla \phi \, dV. \end{aligned}$$

Setting $\phi = f_t := \Psi(c, a; t) - \Psi(c, a) \in H_{\mathbb{D},0}^1(\Omega)$, we then obtain

$$\begin{aligned} \int_{\Omega} \varepsilon(\bar{c}) \varepsilon_0 |\nabla f_t|^2 \, dV &= \sum_{i=1}^M \int_{\Omega} a_i \varepsilon'(\bar{c}) \varepsilon_0 \nabla \psi(c) \cdot \nabla f_t \, dV \\ &\quad - \int_{\Omega} \frac{\varepsilon(\bar{c} + t\bar{a}) - \varepsilon(\bar{c})}{t} \varepsilon_0 \nabla \psi(c + ta) \cdot \nabla f_t \, dV \\ &= \sum_{i=1}^M \int_{\Omega} a_i \varepsilon'(\bar{c}) \varepsilon_0 [\nabla \psi(c) - \nabla \psi(c + ta)] \cdot \nabla f_t \, dV \end{aligned}$$

$$+ \int_{\Omega} \left[\sum_{i=1}^M a_i \varepsilon'(\bar{c}) - \frac{\varepsilon(\bar{c} + t\bar{a}) - \varepsilon(\bar{c})}{t} \right] \varepsilon_0 \nabla \psi(c + ta) \cdot \nabla f_t dV.$$

Since $\varepsilon'(\bar{c})$ is bounded in Ω and $\varepsilon(\bar{c}) \geq \varepsilon_{\min}$ in Ω , we thus have by the assumption on $\varepsilon = \varepsilon(\bar{c})$, the Cauchy–Schwarz inequality, and Lemma 3.2.2 that

$$\begin{aligned} \varepsilon_{\min} \varepsilon_0 \|\nabla f_t\|_{L^2(\Omega)} &\leq \left(\sum_{i=1}^M \|a_i\|_{L^\infty(\Omega)} \right) |\varepsilon'(0)| \varepsilon_0 \|\nabla \psi(c) - \nabla \psi(c + ta)\|_{L^2(\Omega)} \\ &\quad + \left\| \sum_{i=1}^M a_i \varepsilon'(\bar{c}) - \frac{\varepsilon(\bar{c} + t\bar{a}) - \varepsilon(\bar{c})}{t} \right\|_{L^\infty(\Omega)} \varepsilon_0 \|\nabla \psi(c + ta)\|_{L^2(\Omega)} \\ &\rightarrow 0 \quad \text{as } t \rightarrow 0. \end{aligned}$$

This and the Poincaré inequality for functions in $H_{D,0}^1(\Omega)$ imply the convergence $\Psi(c, a; t) \rightarrow \Psi(c, a)$ in $H^1(\Omega)$ as $t \rightarrow 0$. The convergence $\Psi_D(c, a; t) \rightarrow \Psi_D(c, a)$ in $H^1(\Omega)$ as $t \rightarrow 0$ can be proved similarly. \square

Proof of Theorem 3.3.1. We first consider $F_{\text{ent}}[c]$ defined in (3.11). By the boundedness of all a , b , and c , and Lebesgue’s Dominated Convergence Theorem, we have by (3.12) that

$$\begin{aligned} \delta^2 F_{\text{ent}}[c][a, b] &:= \lim_{t \rightarrow 0} \frac{\delta F_{\text{ent}}[c + ta][b] - \delta F_{\text{ent}}[c][b]}{t} \\ &= \lim_{t \rightarrow 0} \sum_{i=1}^M \int_{\Omega} b_i \frac{\beta^{-1} \log(\Lambda^3(c_i + ta_i)) - \beta^{-1} \log(\Lambda^3 c_i)}{t} dV \\ &= \sum_{i=1}^M \int_{\Omega} b_i \beta^{-1} \frac{d}{dt} \log(c_i + ta_i) \Big|_{t=0} dV \\ &= \sum_{i=1}^M \int_{\Omega} \frac{a_i b_i}{\beta c_i} dV. \end{aligned} \tag{3.21}$$

We now consider $F_{\text{pot}}[c]$ defined in (3.10). By (3.16) and using our notation $\Psi(c, a; t)$ and $\Psi_D(c, a; t)$ (cf. (3.20)), we have

$$\begin{aligned} &\frac{1}{t} \{\delta F_{\text{pot}}[c + ta][b] - \delta F_{\text{pot}}[c][b]\} \\ &= \sum_{i=1}^M \int_{\Omega} b_i q_i \Psi(c, a; t) dV - \frac{1}{2} \sum_{i=1}^M \int_{\Omega} b_i q_i \Psi_D(c, a; t) dV \end{aligned}$$

$$\begin{aligned}
& -\frac{1}{2} \sum_{i=1}^M \int_{\Omega} b_i \left[\frac{\varepsilon'(\bar{c} + t\bar{a}) - \varepsilon'(\bar{c})}{t} \right] \varepsilon_0 \nabla \psi(c + ta) \cdot \nabla [\psi(c + ta) - \psi_{\text{D}}(c + ta)] dV \\
& -\frac{1}{2} \sum_{i=1}^M \int_{\Omega} b_i \varepsilon'(\bar{c}) \varepsilon_0 \nabla \psi(c + ta) \cdot \nabla [\Psi(c, a; t) - \Psi_{\text{D}}(c, a; t)] dV \\
& -\frac{1}{2} \sum_{i=1}^M \int_{\Omega} b_i \varepsilon'(\bar{c}) \varepsilon_0 \nabla \Psi(c, a; t) \cdot \nabla [\psi(c) - \psi_{\text{D}}(c)] dV.
\end{aligned}$$

Consequently, since

$$\frac{\varepsilon'(\bar{c} + t\bar{a}) - \varepsilon'(\bar{c})}{t} \rightarrow \sum_{j=1}^M a_j \varepsilon''(\bar{c}) \quad \text{in } L^\infty(\Omega),$$

we have by Lemma 3.2.2 and Lemma 3.3.2, and by rearranging terms, that

$$\begin{aligned}
\delta^2 F_{\text{pot}}[c][a, b] & := \lim_{t \rightarrow 0} \frac{1}{t} \{ \delta F_{\text{pot}}[c + ta][b] - \delta F_{\text{pot}}[c][b] \} \\
& = \sum_{i=1}^M \int_{\Omega} b_i q_i \Psi(c, a) dV - \frac{1}{2} \sum_{i=1}^M \int_{\Omega} b_i q_i \Psi_{\text{D}}(c, a) dV \\
& \quad - \frac{1}{2} \int_{\Omega} \left(\sum_{i=1}^M b_i \right) \left(\sum_{j=1}^M a_j \right) \varepsilon''(\bar{c}) \varepsilon_0 \nabla \psi(c) \cdot \nabla [\psi(c) - \psi_{\text{D}}(c)] dV \\
& \quad - \frac{1}{2} \sum_{i=1}^M \int_{\Omega} b_i \varepsilon'(\bar{c}) \varepsilon_0 \nabla \psi(c) \cdot [\nabla \Psi(c, a) - \nabla \Psi_{\text{D}}(c, a)] dV \\
& \quad - \frac{1}{2} \sum_{i=1}^M \int_{\Omega} b_i \varepsilon'(\bar{c}) \varepsilon_0 \nabla \Psi(c, a) \cdot \nabla [\psi(c) - \psi_{\text{D}}(c)] dV \\
& = -\frac{1}{2} \int_{\Omega} \left(\sum_{i=1}^M b_i \right) \left(\sum_{j=1}^M a_j \right) \varepsilon''(\bar{c}) \varepsilon_0 \nabla \psi(c) \cdot \nabla [\psi(c) - \psi_{\text{D}}(c)] dV \\
& \quad + \sum_{i=1}^M \int_{\Omega} b_i q_i \Psi(c, a) dV - \frac{1}{2} \sum_{i=1}^M \int_{\Omega} b_i q_i \Psi_{\text{D}}(c, a) dV \\
& \quad - \sum_{i=1}^M \int_{\Omega} b_i \varepsilon'(\bar{c}) \varepsilon_0 \nabla \psi(c) \cdot \nabla \Psi(c, a) dV \\
& \quad + \frac{1}{2} \sum_{i=1}^M \int_{\Omega} b_i \varepsilon'(\bar{c}) \varepsilon_0 \nabla \psi(c) \cdot \Psi_{\text{D}}(c, a) dV \\
& \quad + \frac{1}{2} \sum_{i=1}^M \int_{\Omega} b_i \varepsilon'(\bar{c}) \varepsilon_0 \nabla \psi_{\text{D}}(c) \cdot \Psi(c, a) dV
\end{aligned}$$

$$\begin{aligned}
&= -\frac{1}{2} \int_{\Omega} \left(\sum_{i=1}^M b_i \right) \left(\sum_{j=1}^M a_j \right) \varepsilon''(\bar{c}) \varepsilon_0 \nabla \psi(c) \cdot \nabla [\psi(c) - \psi_D(c)] dV \\
&\quad + \sum_{i=1}^M \int_{\Omega} b_i [q_i \Psi(c, a) - \varepsilon'(\bar{c}) \varepsilon_0 \nabla \psi(c) \cdot \nabla \Psi(c, a)] dV \\
&\quad - \frac{1}{2} \sum_{i=1}^M \int_{\Omega} b_i [q_i \Psi_D(c, a) - \varepsilon'(\bar{c}) \varepsilon_0 \nabla \psi(c) \cdot \nabla \Psi_D(c, a)] dV \\
&\quad + \frac{1}{2} \sum_{i=1}^M \int_{\Omega} b_i \varepsilon'(\bar{c}) \varepsilon_0 \nabla \psi_D(c) \cdot \nabla \Psi(c, a) dV.
\end{aligned}$$

By the weak formulation for $\Psi(c, b)$ (cf. (3.18) with b replacing a) with $\phi = \Psi(c, a)$, the weak formulation for $\Psi(c, b)$ (cf. (3.18) with b replacing a) with $\phi = \Psi_D(c, a)$, and the weak formulation for $\Psi_D(c, b)$ (cf. (3.19) with b replacing a) with $\phi = \Psi(c, a)$, we therefore obtain

$$\begin{aligned}
\delta^2 F_{\text{pot}}[c][a, b] &= -\frac{1}{2} \int_{\Omega} \left(\sum_{i=1}^M b_i \right) \left(\sum_{j=1}^M a_j \right) \varepsilon''(\bar{c}) \varepsilon_0 \nabla \psi(c) \cdot \nabla [\psi(c) - \psi_D(c)] dV \\
&\quad + \int_{\Omega} \varepsilon(\bar{c}) \varepsilon_0 \nabla \Psi(c, b) \cdot \nabla \Psi(c, a) dV \\
&\quad - \frac{1}{2} \int_{\Omega} \varepsilon(\bar{c}) \varepsilon_0 \nabla \Psi(c, b) \cdot \nabla \Psi_D(c, a) dV \\
&\quad - \frac{1}{2} \int_{\Omega} \varepsilon(\bar{c}) \varepsilon_0 \nabla \Psi_D(c, b) \cdot \nabla \Psi(c, a) dV.
\end{aligned}$$

This and (3.21) imply the desired second variation. \square

3.4 Non-Convexity of the Free-Energy Functional

By Theorem 3.3.1, the second variation $\delta^2 F[c]$ is not necessarily positive definite, i.e., $\delta^2 F[c][a, a]$ may not be positive, as $\varepsilon''(\bar{c}) \geq 0$ by our assumption that is based on experimental data. This indicates that the free-energy functional (3.1) may be nonconvex. We investigate this non-convexity by examining the generalized Boltzmann distributions. If we assume $\psi_{\infty} = 0$ on Γ_D , then $\psi_D = 0$ in Ω , cf. (3.7), and hence the generalized Boltzmann distributions (3.17) become

$$c_i = c_i^{\infty} e^{-\beta q_i \psi} e^{\beta \varepsilon'(\bar{c}) \varepsilon_0 |\nabla \psi|^2 / 2}, \quad i = 1, \dots, M, \quad (3.22)$$

where $\psi = \psi(c)$. Summing over all i and using the notation $\bar{c} = \sum_{i=1}^M c_i$, we obtain

$$\bar{c} = \left(\sum_{i=1}^M c_i^\infty e^{-\beta q_i \psi} \right) e^{\beta \varepsilon'(\bar{c}) \varepsilon_0 |\nabla \psi|^2 / 2}.$$

Based on these considerations, we define for any given $s \in \mathbb{R}$ and $v \geq 0$

$$G(\bar{c}) = G_{s,v}(\bar{c}) = \left(\sum_{i=1}^M c_i^\infty e^{-\beta q_i s} \right) e^{\beta \varepsilon'(\bar{c}) \varepsilon_0 v^2 / 2} - \bar{c} \quad \forall \bar{c} \geq 0.$$

Notice that if $c = (c_1, \dots, c_M)$ satisfies the generalized Boltzmann distributions (3.22), $s = \psi(c)$, and $v = |\nabla \psi(c)|$, then $G(\bar{c}) = 0$ with $\bar{c} = \sum_{i=1}^M c_i$.

We now consider an ionic solution occupying the annulus region $10 < r = |x| < 60$ (in Å) with the charge density $\sigma = -0.02 \text{ e}/\text{Å}^2$ on $r = 10$. We assume there are two ionic species in the solution with $Z_1 = 1$, $Z_2 = -1$, $c_1^\infty = 0.1 \text{ M}$, and $c_2^\infty = 0.1 \text{ M}$. We choose $\varepsilon(\bar{c}) = 70e^{-0.22\bar{c}} + 10$ which we used to fit experimental data, cf. Figure 1.4. From our numerical computational results (cf. Section 3.5 for details), we fix a few selected values of ψ and $|\nabla \psi|$ near the charged surface $r = 10$, and then plot in Figure 3.2 (Left) the graph of function $G(\bar{c}) = G_{s,v}(\bar{c}) = G_{\psi,|\nabla \psi|}(\bar{c})$, where we use c instead of \bar{c} and $\phi = \beta e \psi$ instead of ψ . We observe that there are multiple solutions to the equation $G(c) = 0$ for some values of ϕ and $|\nabla \phi|$, indicating that the generalized Boltzmann distributions may not determine uniquely the concentrations through the electrostatic potential. In Figure 3.2 (Right), we plot zeros of $G(c) = 0$ vs. c . We see that there are three zeros when the electrostatic potential is large in magnitude.

We now construct two examples to show that the free-energy functional (3.1) is in general nonconvex. For simplicity, we take ε_0 to be the unity.

Example 1. Let $\sigma, \beta, \lambda, \mu \in \mathbb{R}$ with $\beta > 0$ and $\lambda > 0$. We consider the functional

$$F[c] = \int_0^1 \frac{1}{2} c \psi dx + \frac{1}{2} \sigma \psi(0) + \int_0^1 [\beta^{-1} c \log(\lambda c) - \mu c] dx \quad (3.23)$$

for functions $c = c(x) \geq 0$ with $x \in (0, 1)$, where the potential $\psi = \psi(x)$ is

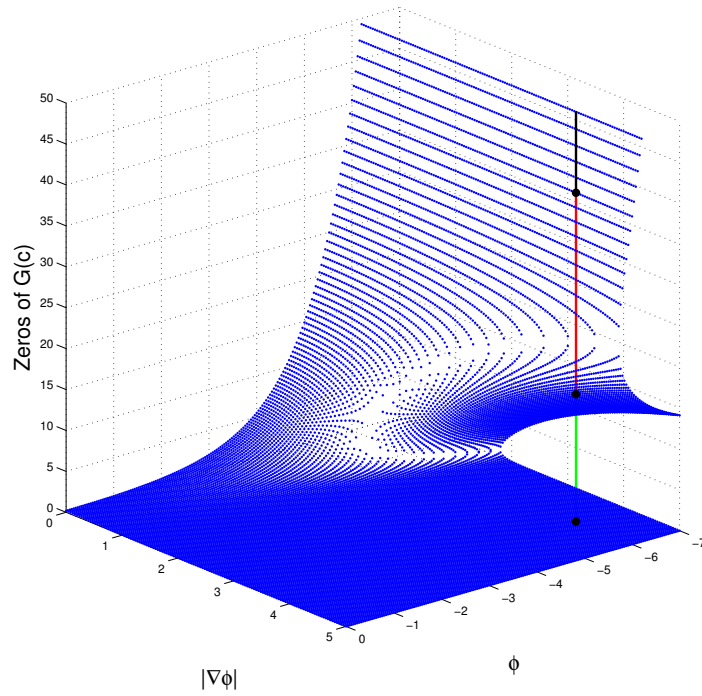
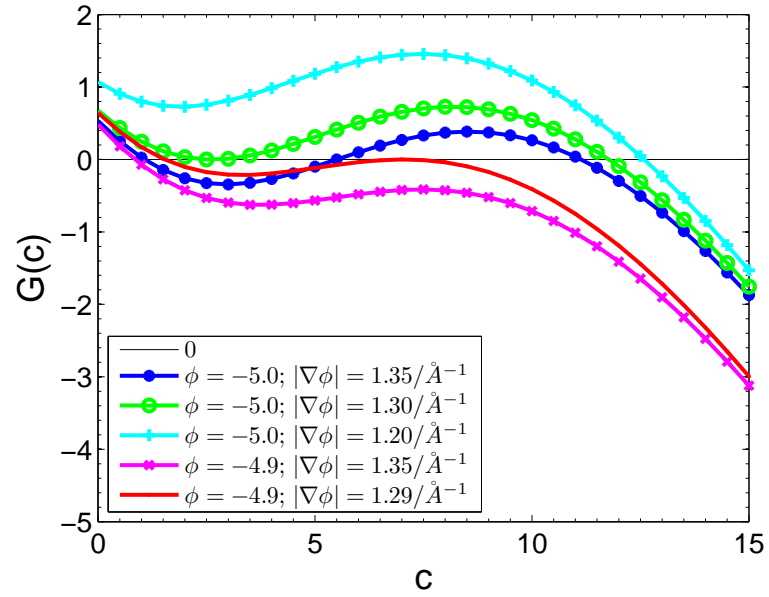


Figure 3.2: Top: $G(c)$ vs. c for different values of ϕ and $|\nabla\phi|$. Bottom: Zeros of $G(c)$ vs. ϕ and $|\nabla\phi|$. The three dots on the vertical line indicate the three zeros of $G(c)$.

determined by

$$\begin{cases} (\varepsilon(c(x))\psi'(x))' = -c(x), & x \in (0, 1). \\ \psi(1) = 0, \\ \varepsilon(c(0))\psi'(0) = -\sigma, \end{cases}$$

Here, $\varepsilon(c) = 70e^{-0.22c} + 10$, which was used to fit experimental data in Figure 1.4. This model can be viewed as reduced from a three-dimensional model with the ionic concentration and electrostatic potential only varying in the x -coordinate direction.

If c is a constant function, then we have by simple calculations that

$$\begin{aligned} \psi(x) &= -\frac{cx^2}{2\varepsilon(c)} - \frac{\sigma x}{\varepsilon(c)} + \frac{c}{2\varepsilon(c)} + \frac{\sigma}{\varepsilon(c)}, & x \in (0, 1), \\ F[c] &= \frac{c^2 + 3c\sigma + 3\sigma^2}{6\varepsilon(c)} + \beta^{-1}c \log\left(\frac{c}{c^\infty}\right), & c > 0, \end{aligned} \quad (3.24)$$

where $c^\infty = \lambda^{-1}e^{\beta\mu}$. The function $F[c]$, with $\sigma = -0.04$, $\beta^{-1} = 1$, and $c^\infty = 0.1$, is plotted in Figure 3.3. We find that it has two local minima at $c = 0$ and $c \approx 48.4$, and that it is nonconvex. Hence, the functional $F[c]$ defined in (3.23) is not convex in general.

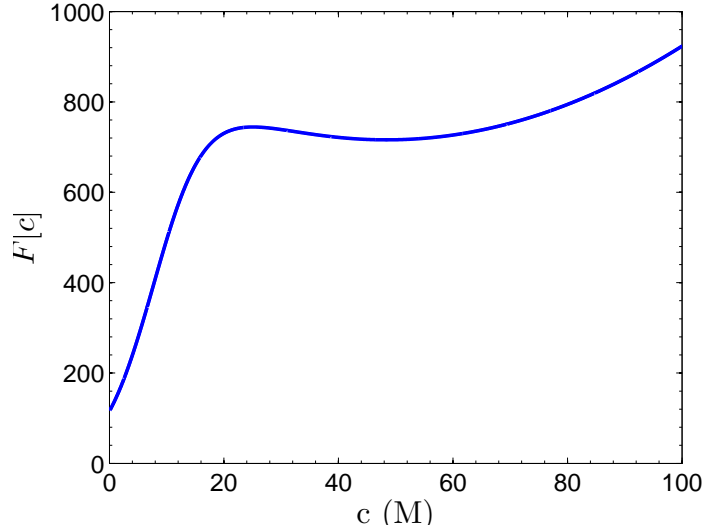


Figure 3.3: Graph of the function $F[c]$ defined in (3.24).

Example 2. We consider the free-energy functional

$$F[c] = \int_0^1 \left(\frac{1}{2} c \psi + c \log c - 2c \right) dx \quad (3.25)$$

for functions $c = c(x) \geq 0$ with $x \in (0, 1)$, where the potential $\psi = \psi(x)$ is determined by

$$\begin{cases} (\varepsilon(c(x))\psi'(x))' = -c(x), & x \in (0, 1). \\ \psi(0) = \psi(1) = 0, \end{cases}$$

The function $\varepsilon = \varepsilon(c)$ is defined by

$$\varepsilon(c) = \begin{cases} \frac{1025}{36} - \frac{50}{9}c & \text{if } 0 \leq c < 4, \\ \frac{25}{18}(c-6)^2 + \frac{25}{36} & \text{if } 4 \leq c < 6, \\ \frac{25}{36} & \text{if } 6 \leq c < \infty. \end{cases} \quad (3.26)$$

It can be verified that this is a C^1 -function, monotonically decreasing, convex, and bounded above and below by positive constants. See Figure 3.4 (Left) for a plot of this function.

For constant functions c , we have

$$\begin{aligned} \psi(x) &= -\frac{cx^2}{2\varepsilon(c)} + \frac{cx}{2\varepsilon(c)}, & x \in (0, 1), \\ F[c] &= \frac{c^2}{24\varepsilon(c)} + c \log(c) - 2c, & c > 0. \end{aligned} \quad (3.27)$$

Figure 3.4 (Right) is a plot of the function $F[c]$ defined in (3.27). We see clearly that this function $F[c]$ is not convex. Hence the functional $F[c]$ defined in (3.25) is not convex.

3.5 Numerical Study of a Model System

We minimize numerically the free-energy functional (3.1) and (3.3) with

$$\begin{aligned} \Omega &= \{x \in \mathbb{R}^3 : R_N < |x| < R_D\}, \\ \Gamma_N &= \{x \in \mathbb{R}^3 : |x| = R_N\}, \quad \Gamma_D = \{x \in \mathbb{R}^3 : |x| = R_D\}, \end{aligned}$$

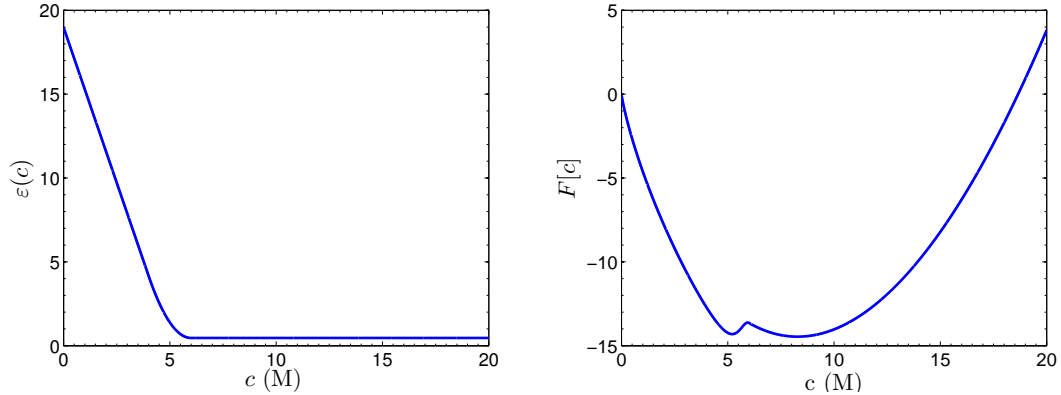


Figure 3.4: Left: Graph of the function $\varepsilon = \varepsilon(c)$ defined in (3.26). Right: Graph of the function $F[c]$ defined in (3.27).

where R_D and R_N are two given positive numbers such that $R_D < R_N$. We assume that $\rho_f = \rho_f(r)$ is a function of $r = |x|$, ψ_∞ is a constant, and σ is also a constant. By the radial symmetry, we assume the concentrations and potential are functions of $r = |x|$ and write $c = c(r)$ and $\psi = \psi(r)$. The free-energy functional (3.1) and the boundary-value problem of Poisson's equation (3.3) become now

$$F[c] = 4\pi \int_{R_N}^{R_D} \left\{ \frac{1}{2} \left(\rho_f + \sum_{i=1}^M q_i c_i \right) \psi + \sum_{i=1}^M \beta^{-1} c_i \left[\log \left(\frac{c_i}{c_i^\infty} \right) - 1 \right] \right\} r^2 dr + 2\pi\sigma R_N^2 \psi(R_N), \quad (3.28)$$

$$\left\{ \begin{array}{l} \varepsilon(\bar{c})\psi''(r) + \varepsilon'(\bar{c})\bar{c}'(r)\psi'(r) + \frac{2}{r}\varepsilon(\bar{c})\psi'(r) = -\frac{1}{\varepsilon_0} \left[\rho_f(r) + \sum_{i=1}^M q_i c_i(r) \right] \\ \text{for } R_N < r < R_D, \\ -\varepsilon(c(R_N))\varepsilon_0\psi'(R_N) = \sigma, \\ \psi(R_D) = \psi_\infty. \end{array} \right. \quad (3.29)$$

Here we use c_i^∞ instead of μ_i ($i = 1, \dots, M$) as input parameters. We have $\mu_i = \beta^{-1} \log(\Lambda^3 c_i^\infty)$ ($i = 1, \dots, M$). With our radially symmetric setting, we can easily observe and verify that the solution ψ_D to the boundary-value problem (3.6) is $\psi_D = \psi_\infty$, a constant. By Theorem 3.2.1, the first variations of the free-energy functional (3.28) in the coordinate directions are then given by

$$\delta_i F[c](r) = q_i \left[\psi(r) - \frac{1}{2}\psi_\infty \right] - \frac{1}{2}\varepsilon'(\bar{c}(r))\varepsilon_0\psi'(r) [\psi'(r) - \psi_\infty]$$

$$+ \beta^{-1} \log \left(\frac{c_i(r)}{c_i^\infty} \right), \quad R_N < r < R_D, \quad i = 1, \dots, M. \quad (3.30)$$

We employ a steepest descent method to minimize the free-energy functional (3.28). After initializing the concentrations $c = (c_1, \dots, c_M)$, we follow these steps:

Step 1. Solve Poisson's equation (3.29) to update the potential ψ .

Step 2. Compute the first variations $\delta_i F[c]$ ($i = 1, \dots, M$) by (3.30).

Step 3. Update the concentrations: $c_i \leftarrow c_i - \gamma d_i$ ($i = 1, \dots, M$), where $\gamma > 0$ is a pre-chosen parameter.

Step 4. Check if $\max_{1 \leq i \leq M} \|\delta_i F[c]\|_{L^\infty(R_N, R_D)} < \varepsilon_{\text{tol}}$ with a pre-chosen tolerance ε_{tol} . If not, go back to (1).

We choose the parameter γ in Step (3) to be very small to ensure that all $c_i > 0$ in each iteration. In case $c_i < 0$ for some i , we can change γ to a smaller value to update c_i . Note that we only find numerically local minimizers that are sometimes more interesting in terms of physical properties than global minimizers.

We now fix $R_N = 10 \text{ \AA}$ and $R_D = 60 \text{ \AA}$, and vary the surface charge density σ from -0.005 to -0.025 e/\AA^2 . As surface charges generally represent the main part of fixed charges, we set $\rho_f = 0$. Moreover, since we are mainly interested in the counterion concentrations and electrostatic potentials near the charged surface, we set $\psi_\infty = 0$. We use $k_B T$ as units of energy. We consider two systems.

System I: $M = 2$, $Z_1 = 1$, $Z_2 = -1$, $c_1^\infty = 0.1 \text{ M}$, and $c_2^\infty = 0.1 \text{ M}$.

System II: $M = 3$, $Z_1 = 2$, $Z_2 = 1$, $Z_3 = -2$, $c_1^\infty = 0.1 \text{ M}$, $c_2^\infty = 0.1 \text{ M}$, $c_3^\infty = 0.15 \text{ M}$.

In each of our numerical computations, we observe the decay of the free energy and the convergence of concentrations in our iterations. This indicates that our numerical method is reliable.

3.5.1 Comparison of different dielectric relations: counterion depletion

We compare equilibrium concentrations and electrostatic potentials corresponding to the following four different dielectric coefficient functions $\varepsilon = \varepsilon_i(\bar{c})$:

($\bar{c} \geq 0$):

$$\begin{aligned}\varepsilon_1(\bar{c}) &= 80; & \varepsilon_2(\bar{c}) &= 80 - 20\bar{c}; \\ \varepsilon_3(\bar{c}) &= \frac{80}{1 + 0.25\bar{c}}; & \varepsilon_4(\bar{c}) &= 70e^{-0.22\bar{c}} + 10.\end{aligned}\tag{3.31}$$

Note that all these functions are convex and monotonically decreasing with the maximum value 80 at $\bar{c} = 0$. In addition $\varepsilon_3(\infty) = 0$ and $\varepsilon_4(\infty) = 10$. The linear dependence $\varepsilon_2(\bar{c})$ is used in [BYAP11]. The form $\varepsilon_3(\bar{c})$ is proposed in [KD09]. We used $\varepsilon_4(\bar{c})$ to fit the experiment data in Figure 1.4.

We consider System I with the surface charge density $\sigma = -0.005 \text{ e}/\text{\AA}^2$. In Figure 3.5, we plot profiles of the equilibrium concentrations for both counterion and coion species for the four different dielectric coefficient defined in (3.31). The four concentration profiles for the species of coions nearly overlap and become one. It is the curve below all the other four for the counterion concentrations. The inset shows the graph of $\varepsilon_i(\bar{c}(r))$ ($1 \leq i \leq 4$) as a function of the radial variable r . We observe differences of the counterion concentrations in the vicinity of the charged surface, even at such a relatively low surface charge density. The counterion concentrations corresponding to $\varepsilon_2(\bar{c})$, $\varepsilon_3(\bar{c})$, and $\varepsilon_4(\bar{c})$ are smaller than that predicted by the classical PB theory that corresponds to $\varepsilon_1(\bar{c})$. Such counterion depletion is expected as explained in Introduction and as found in [BYAP11].

We now still consider System I but increase the surface charge density to $\sigma = -0.012 \text{ e}/\text{\AA}^2$. In Figure 3.6, we plot concentrations and potential similar to those in Figure 3.5. We see clearly that the counterion depletion near the charged surface is enhanced for the concentration-dependent dielectric coefficient $\varepsilon = \varepsilon_i(\bar{c})$ ($i = 2, 3, 4$). This is because that the increase of the surface charge leads to the increase of the electric field, which in turn decreases more the concentration by the factor $e^{\beta\varepsilon'(\bar{c})\varepsilon_0|\nabla\psi|^2/2}$ in the generalized Boltzmann distributions, since $\varepsilon'(\bar{c}) < 0$ and $|\nabla\psi|$ is larger. We find that, for the case of linear dependence $\varepsilon = \varepsilon_2(\bar{c})$, our numerical solution is quite sensitive. As the concentration becomes large, the dielectric coefficient can be very close to zero and even negative, leading to an unphysical situation that corresponds to the loss of ellipticity mathematically.

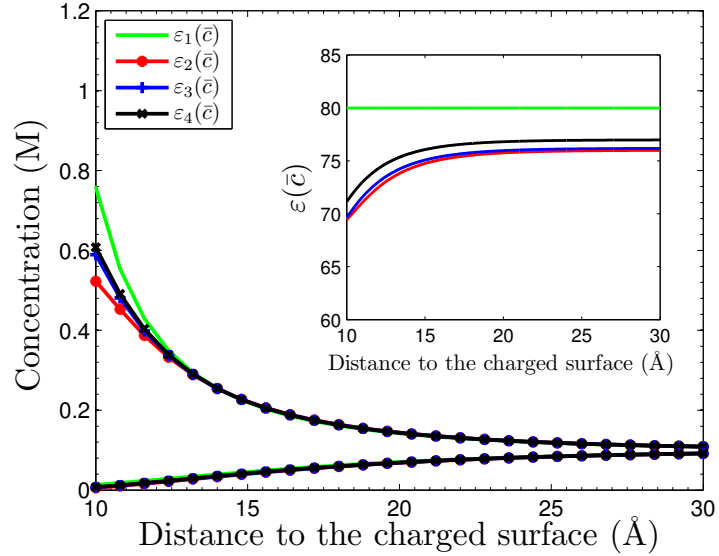


Figure 3.5: The concentrations vs. radial distance to the charged surface for System I with the surface charge density $\sigma = -0.005 \text{ e}/\text{\AA}^2$. Inset: the graph of function $\varepsilon_i(\bar{c}(r))$ for $i = 1, \dots, 4$.

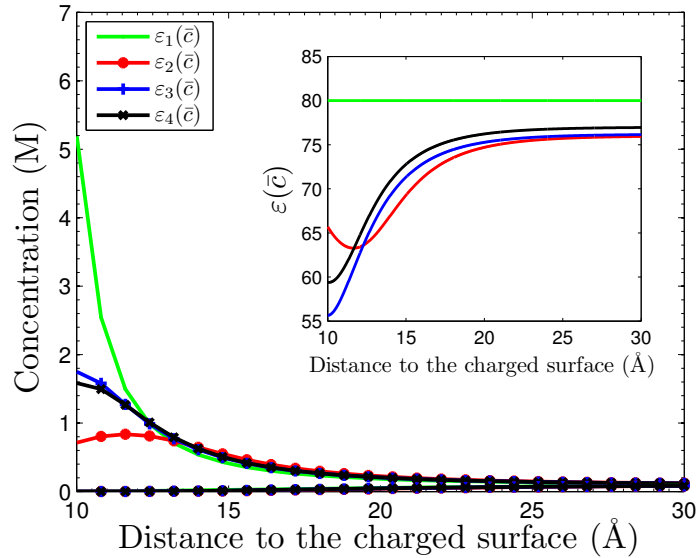


Figure 3.6: The concentrations vs. radial distance to the charged surface for System I with the surface charge density $\sigma = -0.012 \text{ e}/\text{\AA}^2$. Inset: the graph of function $\varepsilon_i(\bar{c}(r))$ for $i = 1, \dots, 4$.

3.5.2 Effect of surface charges and bulk concentrations: non-monotonicity of counterion concentrations

We now consider System I with $\varepsilon = \varepsilon_4(\bar{c})$ defined in (3.31). We compute the equilibrium concentration and electrostatic potential with the surface charge densities $\sigma = -0.01 \text{ e}/\text{\AA}^2$, $-0.015 \text{ e}/\text{\AA}^2$, $-0.02 \text{ e}/\text{\AA}^2$, and $-0.025 \text{ e}/\text{\AA}^2$, respectively, and plot our numerical results in Figure 3.7. The four counterion concentration profiles for the four different values of the surface charge density are indicated by the symbols. The four corresponding coion concentrations overlap and become one curve which is the lowest one. In Figure 3.7, we observe that the counterion concentration is non-monotonic for a large surface charge density. The dielectric function $\varepsilon(\bar{c}(r))$ is also non-monotonic. Moreover, for large surface charge densities, as the surface charge increases, the counterion concentration at the surface (i.e., at $r = R_N = 10 \text{ \AA}$) decreases, and the peak of the counterion concentration profile gets higher and moves further away from the surface. All these result from the competition between the surface-counterion attraction and the counterion depletion near the surface.

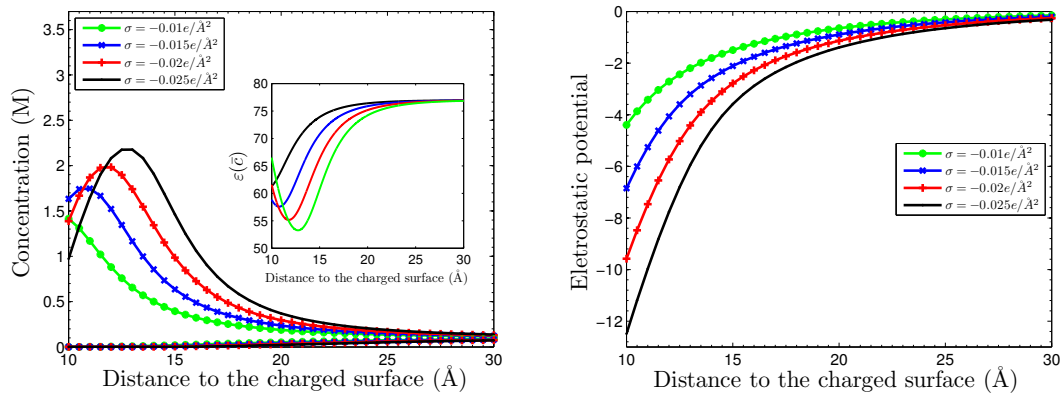


Figure 3.7: System I with $\varepsilon = \varepsilon_4(\bar{c})$. Left: The ionic concentrations vs. the radial distance to the charged surface. Right: The electrostatic potentials vs. the radial distance to the charged surface for different values of the surface charge density.

In Figure 3.8, we plot the counterion concentration at the charged surface and the maximum value of counterion concentration as functions of the surface charge density. For comparison, we also plot the results predicted by the classical

PB theory. We observe that the differences are significant for large surface charges: the counterion concentration at the charged surface predicted using $\varepsilon = \varepsilon_4(\bar{c})$ decreases but that predicted by the classical PB equation increases. Moreover, the maximum value of counterion concentration predicted with $\varepsilon = \varepsilon_4(\bar{c})$ increases as the surface charge density increases.

We also plot the electrostatic potential at the charged surface in Figure 3.8 (Right). As the surface charge density increases, the electrostatic potentials at the charged surface predicted by the classical PB are weaker than those predicted with $\varepsilon = \varepsilon_4(\bar{c})$. This is because that the screening effect with the ionic decrement is weaker.

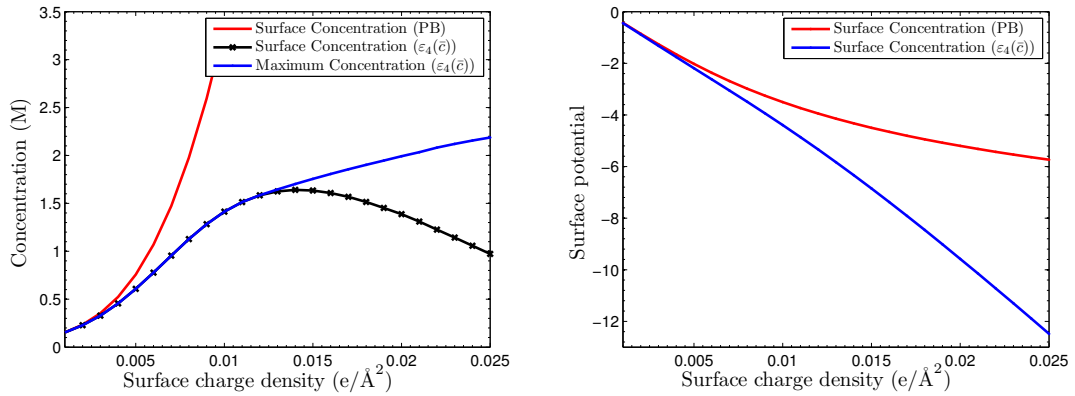


Figure 3.8: Left: The Counterion concentration at the charged surface and the maximum value of counterion concentration vs. the surface charge density. Right: The electrostatic potential at the charged surface vs. the surface charge density.

We now fix the surface charge density $\sigma = -0.012 e/\text{\AA}^2$ and vary the bulk concentrations c_i^∞ ($i = 1, 2$). From Figure 3.9 (Left), we observe that larger bulk concentrations lead to the stronger depletion effect. From Figure 3.9 (Right), we see that the counterion distribution is monotonic for low bulk concentrations and is non-monotonic after bulk concentrations exceed 0.2 M. Their differences increase as the bulk concentrations increase.

We now consider System II in which there are two species of counterions and one species of coions. In Figure 3.10, we plot concentration profiles for different values of surface charge density. We can again observe the ionic depletion for high surface charges.

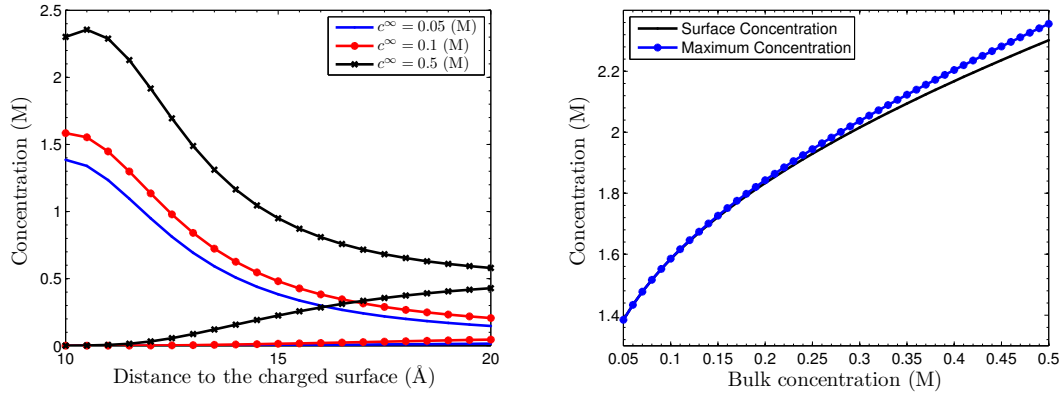


Figure 3.9: Left: Concentrations vs. radial distance to the charged surface with different ionic concentrations. Right: The counterion concentration at the charged surface and the maximal value of counterion concentration vs. bulk ionic concentration.

3.6 Remarks

In this chapter, we build up the theoretical foundation of the mean-field model with concentration dependent dielectric and Poisson electrostatics. The theory part include model setup, first and second variation, generalized Boltzmann distribution and non-convexity of the free-energy functional. Moreover, we perform a numerical computation in a model system and find unusual phenomena.

Our basic modeling assumption is that the dependence of the dielectric coefficient on the sum of individual ionic concentrations is qualitatively the same as that on the salt concentrations for which experimental data are available. Such dependence is expressed mathematically as a continuous, monotonically decreasing, and convex function.

Our free-energy functional (3.1) extends those in [Li09b, CDLM08, RR90, FB97], where the dielectric coefficient is independent of concentrations, and that in [BYAP11], where the dielectric coefficient depends linearly on the concentrations. It should be noted that a linear dependence $\varepsilon = \varepsilon_2(\bar{c})$ (cf. (3.31)) leads to the ill-posedness of Poisson's equation (cf. (3.3)). A nonlinear dependence of dielectric coefficient on concentrations is significant, as it can lead to the existence of multiple equilibrium concentrations. Our numerical results show interesting phenomena,

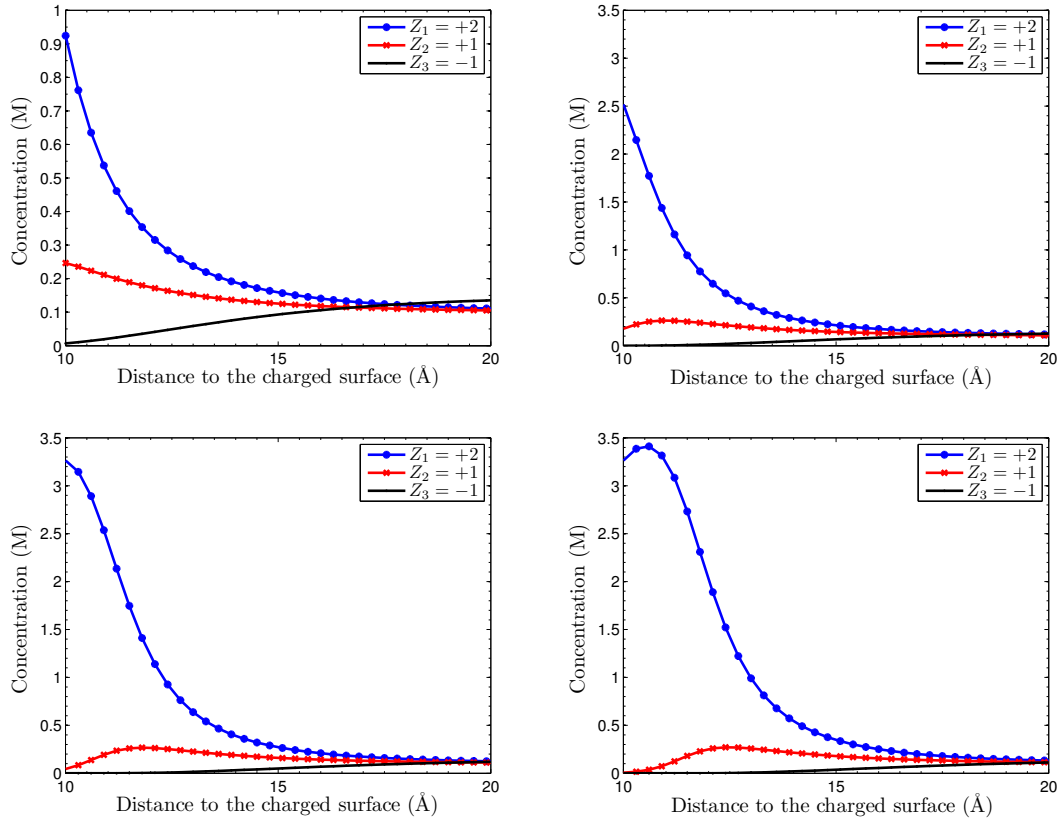


Figure 3.10: Ionic concentrations vs. radial distance to the charge surface with different values of surface charge density σ . Upper left: $\sigma = -0.005e/\text{\AA}^2$. Upper right: $\sigma = -0.01e/\text{\AA}^2$. Lower left: $\sigma = -0.015e/\text{\AA}^2$. Lower right: $\sigma = -0.02e/\text{\AA}^2$.

extending those found in [BYAP11, Fry11, KD09, LAO12, BYAHP09]. However, the nonlinear dependence leads to the lack of compactness needed in proving the existence of a minimizer by the usual argument of direct methods in the calculus of variations. To prove the existence, we will then need to construct carefully a free-energy-minimizing sequence that is weakly compact. The nonconvexity of the functional is different from that for the classical PB functional. It will be interesting to understand if such nonconvexity can be used to model the transition from weak to strong interactions in an ionic solution.

Our numerical algorithm is fairly general. The key of our algorithm is the self-consistency: In each step of relaxing the free-energy functional, we solve Poisson's equation with the concentration dependent dielectric coefficient. We

update the concentrations and electrostatic potential alternatively. If one simply uses the classical Boltzmann distributions for c_i 's in $\varepsilon = \varepsilon(\bar{c})$, one may not be able to capture the ionic depletion as shown in the recent work [LL14].

One of the ion-specific properties is the ionic size effect. In recent years, the PB-like mean-field models that account for ionic size effects have been developed [LLXZ13,BAO97,Tre08,Li09b,Li09a,ZWL11,WZXL12,BYAP11,Fry11,BYAHP09,LZ11]. Our experience is that a large (in terms of magnitude) surface charge density is needed to capture the ionic size effect in such models, while only a small charge density is needed to capture the ionic decrement near a charged surface. It will be therefore interesting to see the transition characterized by the surface charge density.

Another important issue that we have not addressed here is the Born solvation energy of ions [MX14,Wan10,XML14]. Additional equations may be needed to describe such energy. It is interesting to understand whether the inclusion of the Born solvation energy will also lead to the correction term in the generalized Boltzmann distributions. Finally, in terms of applications, how to apply our results to modeling charged macromolecules, such as proteins, in an aqueous environment is of great interest.

Acknowledgements

Chapter 3, in part is taken from the material as it appears in *Mean-field Theory and Computation of Electrostatics with Ionic concentration Dependent Dielectrics* by B. Li, J. Wen, and S. Zhou, accepted for publication in *Communications in Mathematical Sciences*.

Chapter 4

Phase-Field Model with Poisson–Boltzmann Electrostatics

4.1 Introduction

The structure, dynamics, and function of biomolecular systems are crucially influenced by the interaction between the biomolecules and their aqueous environment. Such interactions can be described efficiently by implicit-solvent models [TP94, CT99, RS99, FI04], in which the solvent molecules and ions are treated implicitly and their effects are coarse-grained; cf. Figure 4.1 for a schematic view of two different descriptions of a solvation system. In the left part, both the solute atoms (dark dots) and solvent molecules (grey dots) are degrees of freedom in the system. In the right part, the solvent molecules are coarse-grained and the solvent is treated as a continuum. The solvent region Ω_w and the solute region Ω_m are separated by the solute-solvent interface Γ , and the solute atoms are located $\mathbf{x}_1, \dots, \mathbf{x}_N$ inside Ω_m . In an implicit-solvent model, the effect of solvent is described through the interface separating the solutes and solvent, and the related macroscopic quantities, such as the surface tension and the bulk solvent density. These models are complementary to the more accurate but computationally expensive explicit-solvent models, such as molecular dynamics simulations, which often provide sampled statistical information rather than direct descriptions of

thermodynamics.

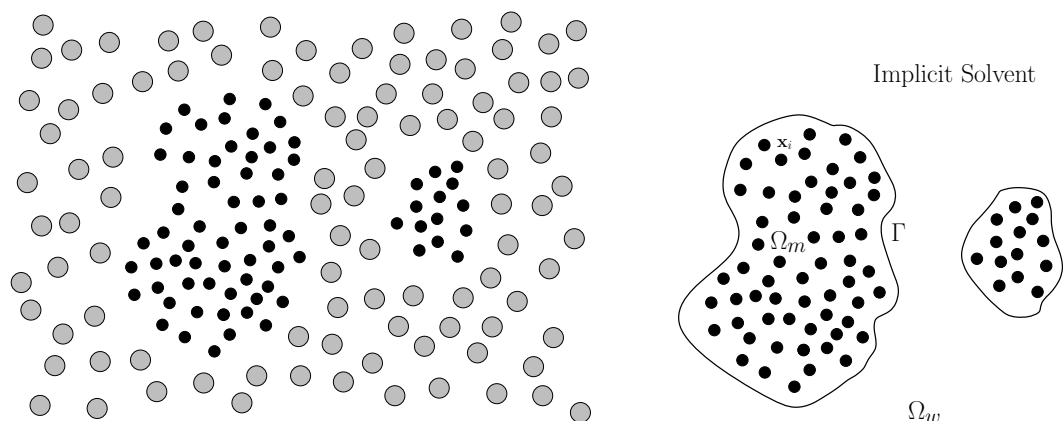


Figure 4.1: Schematic view of a solvation system. Left: a full atomistic model. Right: an implicit-solvent model. The solute-solvent interface Γ separates the solute region Ω_m from the solvent region Ω_w .

A large class of existing implicit-solvent models are based on various kinds of predefined solute-solvent interfaces, such as the van der Waals surface (vdWS), solvent-excluded surface (SES), or solvent-accessible surface (SAS) [LR71, Ric77, Con83, Ric84, Con92]. In these models, the solvation free energy is approximated by the sum of the interfacial energy and the electrostatic free energy determined by the Poisson–Boltzmann (PB) [DM90, FB97, GT08, Li09b, SH90a] or Generalized Born (GB) [BC00, STHH90, Bak05] theory in which the vdWS, SAS, or SES is used as a dielectric boundary. While such fixed-surface implicit-solvent approaches have been extensively used and successful in many cases, their accuracy and general applicability are still questionable. It is believed that one of the main issues here is the decoupling of surface tension, dispersion, and the polar part of the free energy. Moreover, an ad hoc definition of vdWS, SAS, or SES can often lead to inaccurate free-energy calculations. It is additionally well established by now that cavitation free energies do not scale with surface area for high curvatures [LCW99, Cha05, RHK06, WFB10], a fact of critical importance in the implicit-solvent modeling of hydrophobic interactions at molecular scales [BN80, Tan80, CB07, ZHMB04, BWZ09].

In recent years, a new class of implicit-solvent models—the variational implicit-solvent model (VISM)—have been developed [DSM06a, DSM06b]. Cou-

pled with the robust level-set numerical method, such models allow an efficient and quantitative description of molecular solvation [CDML07, CXD⁺09, CWS⁺09, SWC⁺09, CLW10, WCC⁺12]. Central in the VISM is a mean-field free-energy functional of all possible solute-solvent interfaces, or dielectric boundaries, that separate the continuum solvent from all solute atoms. In a simple setting, such a free-energy functional consists of surface energy, solute-solvent van der Waals interaction energy, and continuum electrostatic free energy. The minimization of the functional determines the solvation free energy and stable equilibrium solute-solvent interfaces. Extensive level-set numerical results with comparison with molecular dynamics (MD) simulations have demonstrated the success of this new approach to the solvation molecular systems in capturing the hydrophobic interaction, multiple equilibrium states of hydration, and fluctuation between such states [CDML07, CWS⁺09, SWC⁺09, WCC⁺12]. In general, stable equilibrium solute-solvent interfaces determined by the level-set VISM can be quite different from vdWS, SES, or SAS, particularly when it comes to the description of hydrophobic interactions [Cha05, BWZ09, WKBL11]. Perhaps the most significant feature of VISM is that its free-energy functional exhibits a complex energy landscape with multiple local minima corresponding to different equilibrium states.

Despite the initial success of the sharp-interface VISM [CDML07, CXD⁺09, WCC⁺12, ZCD⁺14, GLD⁺14], it remains challenging to include fluctuations into such a model, both around the solute-solvent interface and in the bulk solvent. Such fluctuations have strong influence in the transition between multiple equilibria and in sampling different states to accurately predict the free energies of underlying biomolecular systems. Therefore, in this part of my dissertation work, I develop a phase-field variational implicit-solvent model, as an alternative to the original sharp-interface model, to the solvation of charged molecules. The phase-field approach has been widely used in studying interface problems arising in many scientific areas, such as materials physics, complex fluids, biomembranes, and cell motility, cf. e.g., [AMW98, CL85, DLW04, Lan86, LRV09, SRL10] and the references therein. Moreover, It can also describe fluctuations [KR99, BRP05]

Central in the phase-field variational approach to the implicit solvation is

a mean-field free-energy functional of all possible phase fields. The functional couples all the surface energy, the solute-solvent van der Waals interactions, and the electrostatic interactions through a phase field. The approximation of the surface area in the free-energy functional is give by

$$\int \left[\frac{\xi}{2} |\nabla \phi|^2 + \frac{1}{\xi} W(\phi) \right] d\mathbf{x},$$

where $\xi > 0$ is a small parameter characterizing the width of transition layer and W is a properly chosen double-well potential. If a phase field ϕ has a low free energy, then the W -term forces the phase field ϕ to be close to the two wells of W except a thin transition layer, partitioning the underlying solvation region into the solute and solven regions, while the gradient term penalizes such partition. As the parameter ξ becomes smaller and smaller, the transition characterized by ϕ becomes a sharp interface; and the corresponding integral value becomes the interfacial area [Mod87, Ste88, LZ13]. This well established mathematical theory is the foundation of the phase-filed approach. The electrostatic part of the free energy is described through the electrostatic potential that solves the PB equation with a phase-field dependent dielectric coefficient.

Given the atomic coordinates and point charges of solute atoms, the effective surface tension of the solute-solvent interface, the bulk solvent density, the dielectric coefficients, and some effective Lennard-Jones parameters, one can minimize the free-energy functional to obtain the minimum free energies as well as the free-energy minimizing optimal phase fields that determine the stable equilibrium conformations of an underlying biomolecular system.

Much of my work is devoted to the design, implement, and test of accurate and efficient numerical methods for solving the gradient-flow partial differential equations of relaxing the phase-field free-energy functional. These equations include a time-dependent diffusion equation for the phase field, where the time presents the optimization step rather than the time of real dynamics, and the phase-field version of the PB equation. I use semi-implicit schemes for the time discretization. In each time step, I use the finite difference method to solve the linear system of equations. I test the convergence of my numerical schemes using a one-particle system which results a radially symmetric, one-dimensional problem.

The rest of the chapter is organized as follows: In Section 4.2, I present my phase-field variational implicit-solvent model for molecular solvation, and some of its mathematical properties. In Section 4.3, I describe my numerical methods for solving the systems of partial differential equations resulting from the gradient-flow of the phase-field free-energy functional. I also present a convergence test for such methods. Finally, in Section 4.4, I make several remarks regarding my studies.

4.2 A Variational Formulation

We consider a molecular solvation system that occupies a finite region Ω in \mathbb{R}^3 ; cf. the right part of Figure 4.1. The system consists of solute atoms located at $\mathbf{x}_1, \dots, \mathbf{x}_N$ in Ω , carrying charges Q_1, \dots, Q_N , respectively, together with the solvent that is treated as a continuum. Let $\xi > 0$ be a small parameter with unit in length. In the framework of variational implicit-solvent description, we consider the following free-energy functional of any possible phase field, also called an order parameter, $\phi = \phi(\mathbf{x})$ ($\mathbf{x} \in \Omega$):

$$F_\xi[\phi] = P \int_{\Omega} \phi^2 d\mathbf{x} + \gamma_0 \int_{\Omega} \left[\frac{\xi}{2} |\nabla \phi|^2 + \frac{1}{\xi} W(\phi) \right] d\mathbf{x} + \rho_w \int_{\Omega} (\phi - 1)^2 U d\mathbf{x} + F_{\text{ele}}[\phi]. \quad (4.1)$$

The minimization of this free-energy functional leads to an optimal phase field ϕ that partitions the solvation region into the solute region and the solvent region. Moreover, the minimum value of the free-energy functional provides a good approximation of the free energy of an underlying molecular system.

In the first term of the free energy (4.1), P is the difference between the pressure inside and outside solute molecules. For a field ϕ with a low free energy, the integral in the first term of $F_\xi[\phi]$ is the volume of the solute region defined by $\phi \approx 1$. Therefore, the first term describes the volumetric contribution of the immersion of a solute molecule into the solvent.

The second term of the free energy (4.1) is the effective surface energy of the solute-solvent interface, where γ_0 is the macroscopic surface tension for a flat solute-solvent interface. The function $W = W(\phi)$ is a double-well potential, given

precisely by

$$W(\phi) = 18\phi^2(1 - \phi)^2,$$

where the factor 18 is chosen so that as $\xi \rightarrow 0$ the integral converges to the surface area. If $\xi > 0$ is very small, then the W -term forces a phase field ϕ with lower free energy to be close to 1 or 0 except a thin transition layer. The gradient term penalizes such partition. It has been proved mathematically that the integral in the γ_0 -term converges to the surface area of an effective solute-solvent interface as $\xi \rightarrow 0$ [LZ13].

The third term of the free-energy functional (4.1) describes the solute-solvent interaction that includes both the short-distance repulsion due to the excluded volume effect and the long-distance attraction. Here, ρ_w is the bulk solvent density. The potential $U = U(\mathbf{x})$ is the sum of pairwise interactions that is often given by

$$U(\mathbf{x}) = \sum_{i=1}^N U_{\text{LJ}}^{(i)}(|\mathbf{x} - \mathbf{x}_i|), \quad (4.2)$$

where $U_{\text{LJ}}^{(i)}$ being the Lennard-Jones potential for the interaction of the i th solute particle at \mathbf{x}_i and a solvent molecule or ion located at \mathbf{x} .

Finally, the last term in (4.1) is the electrostatic free energy this is uniquely determined by the phase field ϕ . It is given by [CDLM08]

$$F_{\text{ele}}[\phi] = \frac{1}{2} \sum_{i=1}^N Q_i \psi_{\text{reac}}(\mathbf{x}_i) + \int_{\Omega} (\phi - 1)^2 \left[\frac{1}{2} \psi V'(\psi) - V(\psi) \right] d\mathbf{x}. \quad (4.3)$$

Here ψ_{reac} is the reaction field, defined by

$$\psi_{\text{reac}} = \psi - \psi_{\text{vac}}.$$

The function $\psi_{\text{vac}} = \psi_{\text{vac}}(\mathbf{x})$ is the electrostatic potential in the reference state, given by

$$\psi_{\text{vac}}(\mathbf{x}) = \sum_{i=1}^N \frac{Q_i}{4\pi\epsilon_m\epsilon_0|\mathbf{x} - \mathbf{x}_i|}.$$

This is the unique solution to

$$-\epsilon_m\epsilon_0\Delta\psi_{\text{vac}} = \rho_f,$$

together with the boundary condition $\psi_{\text{vac}}(\infty) = 0$, where ε_m is the relative permittivity of the underlying charged molecule, and ε_0 is the vacuum permittivity. The fixed charge density ρ_f composed of all point charges Q_1, \dots, Q_N at $\mathbf{x}_1, \dots, \mathbf{x}_N$ is defined as

$$\rho_f(\mathbf{x}) = \sum_{i=1}^N Q_i \delta(\mathbf{x} - \mathbf{x}_i). \quad (4.4)$$

The function $\psi = \psi(\mathbf{x})$ is the electrostatic potential. It is the unique solution to the PB equation in the phase-field formulation

$$-\nabla \cdot \varepsilon(\phi) \nabla \psi + (\phi - 1)^2 V'(\psi) = \rho_f \quad \text{in } \Omega, \quad (4.5)$$

together with some boundary conditions. This equation is equivalent to

$$-\nabla \cdot \varepsilon(\phi) \nabla \psi_{\text{reac}} + (\phi - 1)^2 V'(\psi_{\text{reac}} + \psi_{\text{vac}}) = \nabla \cdot [\varepsilon(\phi) - \varepsilon_m \varepsilon_0] \nabla \psi_{\text{vac}} \quad \text{in } \Omega. \quad (4.6)$$

Note that $\varepsilon(\phi)$ is a phase-field version of the dielectric coefficient which satisfy following condition:

- (1) $\varepsilon(0) = \varepsilon_0 \varepsilon_w$ and $\varepsilon(1) = \varepsilon_0 \varepsilon_m$;
- (2) $\varepsilon'(0) = \varepsilon'(1) = 0$;
- (3) $\varepsilon = \varepsilon(\phi)$ is monotonically decreasing at $\phi \in [0, 1]$.

Notice the second condition is very crucial in deriving the first variation of $F_\xi[\phi]$. In computation, we approximate $\varepsilon(\phi)$ defined by

$$\varepsilon(\phi) = \frac{1}{2} \varepsilon_0 (\varepsilon_m - \varepsilon_w) \left(1 + \tanh \left(\frac{2\phi - 1}{s_\varepsilon} \right) \right) + \varepsilon_w$$

Here s_ε is a small number, we choose 0.1 in computation. In this setup, $\varepsilon(1) \approx \varepsilon_0 \varepsilon_m$ and $\varepsilon(0) \approx \varepsilon_0 \varepsilon_w$, also $\varepsilon'(0) = \varepsilon'(1) \approx 0$ (cf. Figure 4.2).

The function $V = V(\psi)$ in (4.3) and (4.5) is determined by the Boltzmann distributions of the ionic concentrations through the electrostatic potential ψ . More precisely, $-V'(\psi)$ is the ionic charge density, i.e.,

$$-V'(\psi(\mathbf{x})) = \sum_{j=1}^M q_j c_j(\mathbf{x}),$$

where $q_j = z_j e$ with z_j the valence of an ion of the j th ionic species and e the elementary charge, and $c_j = c_j(\mathbf{x})$ is the local concentration at \mathbf{x} of the j th ionic

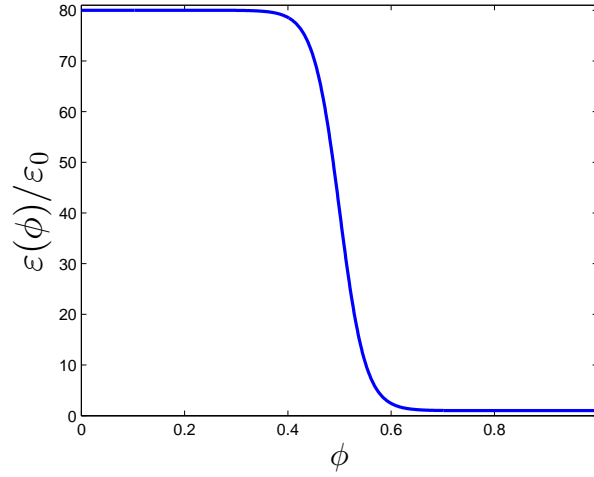


Figure 4.2: A phase-field version of the dielectric coefficient (relative permittivity $\varepsilon(\phi)/\varepsilon_0$), which takes value ε_w at solvent region and ε_m at solute region.

species. For the classical PB equation, the function $V = V(\psi)$ is given by

$$V(\psi) = \beta^{-1} \sum_{j=1}^M c_j^\infty (e^{-\beta q_j \psi} - 1),$$

where $\beta = (k_B T)^{-1}$ with k_B the Boltzmann constant and T the temperature, and c_j^∞ is the bulk concentration of the j th ionic species. For the linearized Poisson–Boltzmann equation, we have

$$V(\psi) = \frac{1}{2} \kappa^2 \varepsilon_w \varepsilon_0 \psi^2, \quad (4.7)$$

where κ is the inverse Debye screening length, defined by

$$\kappa^2 = \frac{\beta}{\varepsilon_w \varepsilon_0} \sum_{j=1}^M c_j^\infty q_j^2,$$

and the function V is now simplified as

Note that the term $(\phi - 1)^2$ in front of $V(\psi)$ in (4.3) and in front of $V'(\psi)$ in (4.5). This means that for a molecular system of low free energy, the ionic charges are only in the solvent region defined by $\phi \approx 0$.

We can now rewrite $F_{\text{ele}}[\phi]$ into

$$F_{\text{ele}}[\phi] = \frac{1}{2} \sum_{i=1}^N Q_i (\psi - \psi_{\text{vac}})(\mathbf{x}_i) - \frac{1}{2} \int_{\Omega} (\phi - 1)^2 \psi V'(\psi) d\mathbf{x}$$

$$+ \int_{\Omega} (\phi - 1)^2 [\psi V'(\psi) - V(\psi)] d\mathbf{x}.$$

The sum of the first two terms, when ψ_{vac} is removed and the self-interactions are also removed, is exactly the electrostatic potential energy of the solvated state. The last term corresponds to the entropic contribution; cf. [CDLM08, ZCD⁺14].

To find stable equilibrium conformations of a molecular system, we minimize the free-energy functional (4.1). To do so, we begin with an initial phase field $\phi_0 = \phi_0(\mathbf{x})$ and then solve numerically the partial differential equations of the steepest descent of the free-energy functional (4.1):

$$\partial_t \phi = -\delta_{\phi} F_{\xi}[\phi],$$

together with the PB equation (4.6), where ∂_t denotes the partial derivative with respect to t and δ_{ϕ} is the variational derivative with respect to ϕ .

We now calculate the variational derivative $\delta_{\phi} F_{\xi}[\phi]$. We first rewrite the electrostatic free energy (4.3). Multiplying both sides of (4.5) by ψ and integrating them over Ω using the integration by parts, we obtain with appropriate boundary conditions that

$$\int_{\Omega} [\varepsilon(\phi) |\nabla \psi|^2 + (\phi - 1)^2 \psi V'(\psi)] d\mathbf{x} = \langle \rho_f, \psi \rangle,$$

where the right-hand side denotes the $\sum_{i=1}^N Q_i \psi(x_i)$, excluding self interactions. This and (4.3) implies that

$$F_{\text{ele}}[\phi] = C_{\text{vac}} + \langle \rho_f, \psi \rangle - \int_{\Omega} \frac{\varepsilon(\phi)}{2} |\nabla \psi|^2 d\mathbf{x} - \int_{\Omega} (\phi - 1)^2 V(\psi) d\mathbf{x}, \quad (4.8)$$

where $C_{\text{vac}} = -\langle \rho_f, \psi_{\text{vac}} \rangle / 2$ is a constant independent of ϕ . Notice that the electrostatic potential ψ depends on the phase field ϕ through the PB equation (4.5). By the definition of the free-energy functional $F_{\xi}[\phi]$ and the new form (4.8) of the electrostatic free energy $F_{\text{ele}}[\phi]$, and employing the integration by parts, we have

$$\begin{aligned} \delta_{\phi} F_{\xi}[\phi] \delta \phi &= 2P \int_{\Omega} \phi \delta \phi d\mathbf{x} + \gamma_0 \int_{\Omega} \left[\xi \nabla \phi \cdot \nabla \delta \phi + \frac{1}{\xi} W'(\phi) \delta \phi \right] d\mathbf{x} \\ &\quad + 2\rho_w \int_{\Omega} (\phi - 1) U \delta \phi d\mathbf{x} \\ &\quad + \langle \rho_f, \delta_{\phi} \psi \rangle - \int_{\Omega} \left[\frac{\varepsilon'(\phi)}{2} \delta \phi |\nabla \psi|^2 + \varepsilon(\phi) \nabla \psi \cdot \nabla \delta_{\phi} \psi \right] d\mathbf{x} \end{aligned}$$

$$\begin{aligned}
& + 2(\phi - 1)\delta\phi V(\psi) + (\phi - 1)^2 V'(\psi)\delta_\phi\psi \Big] d\mathbf{x} \\
= & \int_{\Omega} \left[2P\phi - \gamma_0\xi\Delta\phi + \frac{\gamma_0}{\xi}W'(\phi) + 2\rho_w(\phi - 1)U \right] \delta\phi d\mathbf{x} \\
& + \int_{\Omega} \left[-\frac{\varepsilon'(\phi)}{2}|\nabla\psi|^2 - 2(\phi - 1)V(\psi) \right] \delta\phi d\mathbf{x} \\
& + \langle \rho_f, \delta_\phi\psi \rangle + \int_{\Omega} [\nabla \cdot \varepsilon(\phi)\nabla\psi - (\phi - 1)^2 V'(\psi)] \delta_\phi\psi d\mathbf{x} \\
= & \int_{\Omega} \left[2P\phi - \gamma_0\xi\Delta\phi + \frac{\gamma_0}{\xi}W'(\phi) + 2\rho_w(\phi - 1)U \right. \\
& \left. - \frac{\varepsilon'(\phi)}{2}|\nabla\psi|^2 - 2(\phi - 1)V(\psi) \right] \delta\phi d\mathbf{x},
\end{aligned}$$

where in the last step we used the weak form of the PB equation (4.5). Consequently,

$$\delta_\phi F_\xi[\phi] = 2P\phi - \gamma_0\xi\Delta\phi + \frac{\gamma_0}{\xi}W'(\phi) + 2\rho_w(\phi - 1)U - \frac{\varepsilon'(\phi)}{2}|\nabla\psi|^2 - 2(\phi - 1)V(\psi).$$

To summarize, we shall solve numerically the following system of gradient-flow partial differential equations of the free-energy functional for the functions $\phi = \phi(\mathbf{x}, t)$ and $\psi = \psi(\mathbf{x}, t)$:

$$\begin{aligned}
\partial_t\phi = & -2P\phi + \gamma_0 \left[\xi\Delta\phi - \frac{1}{\xi}W'(\phi) \right] - 2\rho_w(\phi - 1)U \\
& + \frac{\varepsilon'(\phi)}{2}|\nabla\psi|^2 + 2(\phi - 1)V(\psi), \tag{4.9}
\end{aligned}$$

$$-\nabla \cdot \varepsilon(\phi)\nabla\psi_{\text{reac}} + (\phi - 1)^2 V'(\psi_{\text{reac}} + \psi_{\text{vac}}) = \nabla \cdot [\varepsilon(\phi) - \varepsilon_m\varepsilon_0] \nabla\psi_{\text{vac}}, \tag{4.10}$$

with $\psi = \psi_{\text{reac}} + \psi_{\text{vac}}$, together with appropriate boundary conditions for both ϕ and ψ , and some initial conditions for ϕ

4.3 Numerical Methods

4.3.1 Discretization

We choose our computational box to be $\Omega = (-L, L)^3$ and cover it by $N \times N \times N$ uniform grids. All the grid points are labeled by (i, j, k) . We also choose a time step $\Delta t > 0$ and set $t_n = n\Delta t$ for $n = 1, 2, \dots$. For a given function

$u = u(\mathbf{x}, t)$, we denote by $u^n(\mathbf{x})$ an approximation of $u(\mathbf{x}, t_n)$ and by $u_{i,j,k}^n$ an approximation of $u(\mathbf{x}_{i,j,k}, t_n)$ at the grid point $\mathbf{x}_{i,j,k}$ and time t_n .

The system of equations (4.9) and (4.10) can now be discretized as

$$\begin{aligned} \frac{\phi^{n+1} - \phi^n}{\Delta t} &= -2P\phi^{n+1} + \gamma_0\xi\Delta\phi^{n+1} - A(\phi^n) + B(\phi^n, \psi^n), \\ -\nabla \cdot \varepsilon(\phi^{n+1})\nabla\psi_{\text{reac}}^{n+1} + (\phi^{n+1} - 1)^2V'(\psi^{n+1}) &= \nabla \cdot [\varepsilon(\phi^{n+1}) - \varepsilon_m\varepsilon_0] \nabla\psi_{\text{vac}}, \end{aligned}$$

where $\psi^{n+1} = \psi_{\text{reac}}^{n+1} + \psi_{\text{vac}}$. Since the function V from (4.7) is quadratic (as we use the linearized PB equation) and V' is linear, we may rewrite the second equation as

$$\begin{aligned} -\nabla \cdot \varepsilon(\phi^{n+1})\nabla\psi_{\text{reac}}^{n+1} + (\phi^{n+1} - 1)^2V'(\psi_{\text{reac}}^{n+1}) \\ = \nabla \cdot [\varepsilon(\phi^{n+1}) - \varepsilon_m\varepsilon_0] \nabla\psi_{\text{vac}} - (\phi^{n+1} - 1)^2V'(\psi_{\text{vac}}) \end{aligned}$$

After regrouping, we have

$$(1 + 2\Delta tP)\phi^{(n+1)} - (\Delta t\gamma_0\xi)\Delta\phi^{n+1} = \phi^{(n)} + \Delta t[-A(\phi^n) + B(\phi^n, \psi^n)], \quad (4.11)$$

$$-\nabla \cdot \varepsilon(\phi^{n+1})\nabla\psi_{\text{reac}}^{n+1} + (\phi^{n+1} - 1)^2V'(\psi_{\text{reac}}^{n+1}) = C(\phi^{n+1}, \psi_{\text{vac}}), \quad (4.12)$$

where

$$\begin{aligned} A(\phi) &= \frac{\gamma_0}{\xi}W'(\phi) + 2\rho_w(\phi - 1)U, \\ B(\phi, \psi) &= \frac{\varepsilon'(\phi)}{2}|\nabla\psi|^2 + 2(\phi - 1)V(\psi), \\ C(\phi, \psi_{\text{vac}}) &= \nabla \cdot [\varepsilon(\phi) - \varepsilon_m\varepsilon_0] \nabla\psi_{\text{vac}} - (\phi - 1)^2V'(\psi_{\text{vac}}). \end{aligned}$$

Once ϕ^n and ψ^n are known, we can obtain ϕ^{n+1} by solving (4.11) together with the Dirichlet boundary conditions of $\phi = 0$. Since we have now ϕ^{n+1} and ψ^n , we can then get ψ^{n+1} by solving (4.12) together with the Dirichlet boundary conditions of ψ_{reac}^{n+1} approximated by the Yukawa-field approximation [CCL11]

$$\begin{aligned} \psi_{\text{reac}}^{n+1} &= \psi^{n+1} - \psi_{\text{vac}}^{n+1} \\ &= \sum_{i=1}^N \frac{Q_i}{4\pi\varepsilon_w\varepsilon_0(1 + \kappa R_i)} \cdot \frac{e^{-\kappa(|\mathbf{x} - \mathbf{x}_i| - R_i)}}{|\mathbf{x} - \mathbf{x}_i|} - \sum_{i=1}^N \frac{Q_i}{4\pi\varepsilon_m\varepsilon_0|\mathbf{x} - \mathbf{x}_i|}, \end{aligned}$$

where $|\mathbf{x} - \mathbf{x}_i|$ is the distance from the point on the boundary to the center of solute, and R_i is the a fitting parameter. In general, we will approximate $e^{\kappa R_i}$ as $1 + \kappa R_i$, thus by Taylor's expansion

$$\psi_{\text{reac}}^{n+1} = \sum_{i=1}^N \frac{Q_i e^{-\kappa|\mathbf{x}-\mathbf{x}_i|}}{4\pi\varepsilon_w\varepsilon_0|\mathbf{x}-\mathbf{x}_i|} - \sum_{i=1}^N \frac{Q_i}{4\pi\varepsilon_m\varepsilon_0|\mathbf{x}-\mathbf{x}_i|}$$

on boundary of the box.

For the equation of ψ_{reac} , note that the term $\nabla\psi_{\text{vac}}$ on the right-hand side of (4.12) goes to infinity when \mathbf{x} approaches \mathbf{x}_i . In order to stabilize the numerical iteration, we force $\phi = 1$ in the neighborhood of each \mathbf{x}_i at each time step.

4.3.2 Algorithm

Step 1. Input all the parameters: P ; γ_0 , ρ_w , the atomic positions \mathbf{x}_i , and point charges Q_i of solute atoms, and the LJ parameters ε_i and σ_i ($i = 1, \dots, N$); the vacuum and relative permittivities ε_0 and $\varepsilon_m, \varepsilon_w$, and the phase-field parameter ξ . Discretize uniformly a computational box $\Omega = (-L, L)^3$ containing $\mathbf{x}_1, \dots, \mathbf{x}_N$ into $N \times N \times N$ parts with the grid size $h = 2L/N$ at least one fifth of ξ . Generate an initial phase field ϕ^0 , usually by

$$\phi^0 = \tanh \left[\frac{\text{dis}(\mathbf{x}, \cup_i B(\mathbf{x}_i, r_i))}{\xi} \right] \quad (4.13)$$

where $B(\mathbf{x}_i, r_i)$ represents a ball centered at \mathbf{x}_i with radius r_i . Then we solve ψ_{reac}^0 by equation (4.6)

Step 2. Use the finite difference method to solve the equation(4.11) to obtain ϕ^{n+1} . And then similarly solve the equation (4.12) to obtain ψ^{n+1} .

Step 3. Compute the free energy (4.1).

Step 4. Check if a steady state is reached. We compare $(\phi^n, \psi_{\text{reac}}^n)$ with $(\phi^{n+1}, \psi_{\text{reac}}^{n+1})$ and see if

$$\|\phi^{n+1} - \phi^n\|_{L^2} + \|\psi_{\text{reac}}^{n+1} - \psi_{\text{reac}}^n\|_{L^2} \leq 10^{-5}.$$

After the time iteration, we take $\phi_\xi = \phi^{n+1}$, $\psi_{\text{reac}} = \psi_{\text{reac}}^{n+1}$ as our solution, and the zero level set of ϕ_ξ is treated as the solute-solvent interface. If not, set $n := n + 1$, and go back to Step 2.

Notice that different initial phase fields may lead to different steady-state phase fields that are local minima of the free-energy functional (4.1). To distinguish classes of local minima, due to drying and wetting structures that are of importance in molecular solvation, we have designed two classes of initial phase fields. One is a “tight wrap”, a surface that tightly wraps all the points $\mathbf{x}_1, \dots, \mathbf{x}_N$. The other is a “loose wrap”, a surface that loosely contains all the points $\mathbf{x}_1, \dots, \mathbf{x}_N$. Different initial phase fields can be obtained by choose different values of r_i in (4.13).

4.3.3 Convergence test

Let us consider a single point charge Q at origin immersed in an ionic solution. This one-particle system is radially symmetric. In the sharp-interface version of variational implicit-solvent model, the free-energy functional of this one-particle system can be expressed as a one-variable function of the radius of sphere centered at the origin [WCC+12]:

$$G[R] = \frac{4}{3}\pi P R^3 + 4\pi\gamma_0 R^2 + 16\pi\rho_w\epsilon \left(\frac{\sigma^{12}}{9R^9} - \frac{\sigma^6}{3R^3} \right) + \frac{Q^2}{8\pi\epsilon_0 R} \left(\frac{1}{\epsilon_w} - \frac{1}{\epsilon_m} \right). \quad (4.14)$$

where κ is a parameter of the ionic strength. This simple one-dimensional function can be minimized numerically with a very high accuracy. If we take $P = 0$, $\gamma_0 = 0.175 k_B T / \text{\AA}^2$, $\rho_w = 0.0333 \text{\AA}^{-3}$, $\epsilon = 0.3 k_B T$ and $\sigma = 3.5 \text{\AA}$, then the solute-solvent interface radius $R_0 = 3.0540$ and the corresponding total energy $G[R_0] = 17.8668$.

In the phase-field model for this one-particle system, all phase fields are one-variable functions $\phi = \phi(r)$. The free-energy functional (4.1), together with (4.3), and the PB equation become

$$\begin{aligned} F_\xi[\phi] = & 4\pi P \int_0^\infty [\phi(r)]^2 r^2 dr + 4\pi\gamma_0 \int_0^\infty \left[\frac{\xi}{2} |\phi'(r)|^2 + \frac{1}{\xi} W(\phi(r)) \right] r^2 dr \quad (4.15) \\ & + 4\pi\rho_w \int_0^\infty (\phi - 1)^2 U_{LJ}(r) r^2 dr \\ & + 4\pi \int_0^\infty \left\{ -\frac{\epsilon(\phi(r))}{2} |\psi'(r)|^2 + \rho_f(r)\psi(r) - [\phi(r) - 1]^2 V(\psi(r)) \right\} r^2 dr, \\ & - \nabla \cdot \epsilon(\phi) \nabla \psi + (\phi - 1)^2 V'(\psi) = \rho_f. \end{aligned}$$

By numerically minimizing the equation (4.15) with different values of ξ , we display in Table 1, 2, and 3 the results of our diffuse interface calculations and those based on the exact formula (4.14) when $Q = 0$, $Q = 0.1$, and $Q = 0.5$, also $\kappa = 0.01$. For the diffuse interface model, $\xi = 0.5, 0.25, 0.125$. R_ξ represents the corresponding radius of the solute-solvent interface; E_{surf} and E_{elec} are the corresponding surface energy and electrostatic potential energy. In the last column, $\xi = 0.00$ represents the result of sharp interface model. This table clearly indicates the convergence of the diffuse interface model into sharp interface model for $Q = 0$, $Q = 0.1$ and $Q = 0.5$.

Table 4.1: The comparison between the diffuse interface model and sharp interface model for a solute-solvent system with a single one atom centered at the origin, where $Q = 0$ and $\kappa = 0.01$.

ξ	0.5	0.25	0.125	0.00
R_ξ	3.0029	3.0210	3.0349	3.0540
E_{surf}	19.8616	20.0853	20.2623	20.5106
E_{elec}	0.0000	0.0000	0.0000	0.0000

Table 4.2: The comparison between the diffuse interface model and sharp interface model for a solute-solvent system with a single one atom centered at the origin, where $Q = 0.1$ and $\kappa = 0.01$.

ξ	0.5	0.25	0.125	0.00
R_ξ	2.9985	3.0181	3.0304	3.0497
E_{surf}	19.8050	20.0469	20.2014	20.4538
E_{elec}	-0.9269	-0.9152	-0.9086	-0.9000

In Figure 4.3, Figure 4.4 and Figure 4.5, we can visually see that the interface location approximated by $\phi = 0.5$ is converging to the sharp interface location for $Q = 0$, $Q = 0.1$, and $Q = 0.5$. Thus we can confirm the correctness of our model and numerical method.

According our 1D results, we find the strong influence of electrostatic in surface problem. The electrostatic potential energy is always pushing the surface and tend to shrink the surface area. In Figure 4.6, we find out that the radius of

Table 4.3: The comparison between the diffuse interface model and sharp interface model for a solute-solvent system with a single one atom centered at the origin, where $Q = 0.5$ and $\kappa = 0.01$.

ξ	0.5	0.25	0.125	0.00
R_ξ	2.9000	2.9218	2.9373	2.9599
E_{surf}	18.5721	18.8130	18.9904	19.2664
E_{elec}	-23.9864	-23.6589	-23.4362	-23.1817

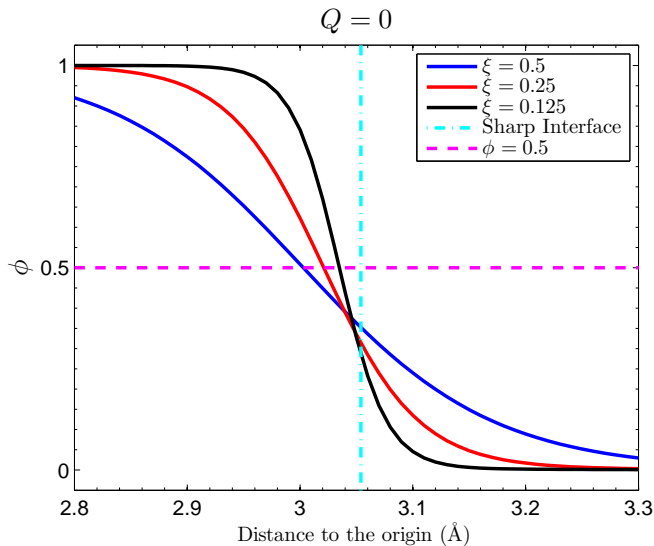


Figure 4.3: The interface of $\phi = 0.5$ is converging to the sharp interface when $Q = 0$.

the ion is decreasing when it carries larger charge.

4.4 Remarks

In this chapter, we incorporate the PB electrostatic into a phase-field variational implicit-solvent model. Related details are also studied carefully to set up the numerical scheme. We also perform numerical experiment for a spherical ion interface problem.

The free-energy framework is similar to the modified mean-field theory discussed in Chapters 2 and 3. This indicates that using variational approach provides more flexibility than classical theory. Moreover, the first variation can be rigor-

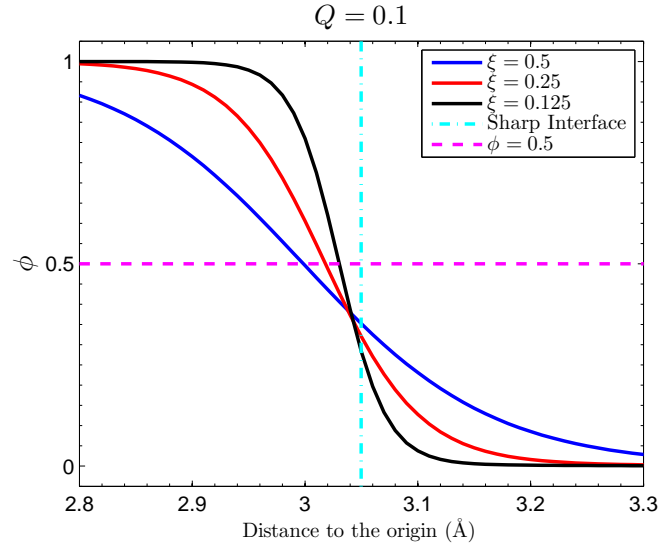


Figure 4.4: The interface of $\phi = 0.5$ is converging to the sharp interface when $Q = 0.1$.

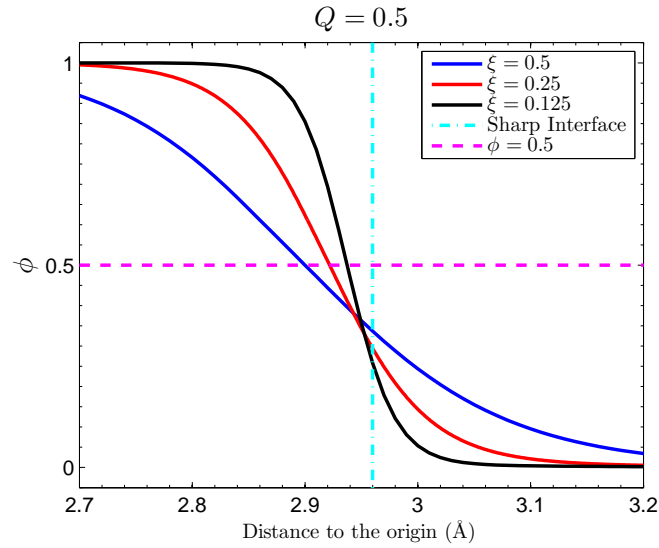


Figure 4.5: The interface of $\phi = 0.5$ is converging to the sharp interface when $Q = 0.5$.

ously derived by the lemmas proved in Chapter 3. The theoretical tools studied in Chapter 3 have potential to be extended in other similar model.

Zhao *et al.* [KZC⁺13] have investigated a phase-field model with Coulomb-field approximation (CFA). Our methodology is similar to their work. But the PB electrostatics leads to additional challenges in the problem. The reasons are as

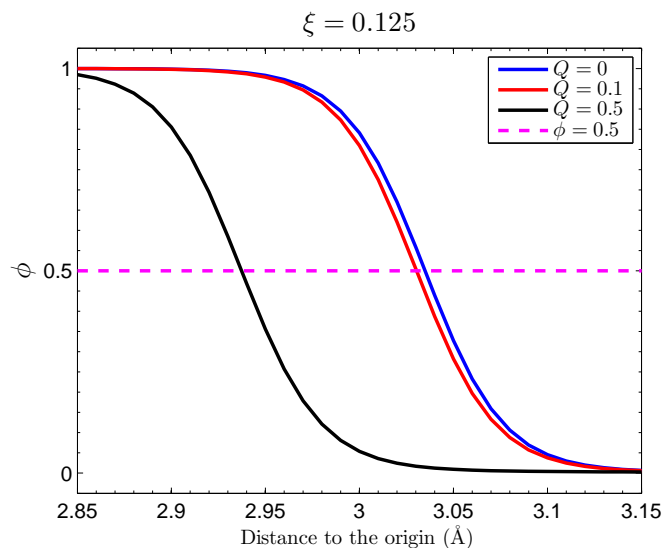


Figure 4.6: The radius of ion is decreasing when it carries larger charge. Here $\xi = 0.5$.

follows: First, the CFA does not cover the whole region, thus the dielectric function will be much straightforward; Second, the CFA does not include a coupled equation, which will significantly simplify the computation. One idea to use the advantage of the CFA is to set the result of the CFA as the initial of our minimization problem. We can expect lower computational cost to minimize the energy functional by using a CFA initial.

It would be really interesting and challenging to implement the 3D computation and capture the multiple states of the interface using the PB electrostatics. We expect it would be investigated in near future.

Acknowledgements

Chapter 4, in part, is taken from material as it appears in *A Self-Consistent Diffused-Interface Approach to Implicit Solvation of Charged Molecules with Poisson-Boltzmann Electrostatics* by J. Wen, Y. Zhao, H. Sun, and B. Li, which is being prepared for submission.

Chapter 5

Conclusions and Discussions

5.1 Summary

In this dissertation, I study mainly mean-field theories and use Monte Carlo (MC) simulation to improve our understanding of the observed phenomena of charged system. I investigate two modified mean-field models in detail and incorporate the Poisson–Boltzmann (PB) electrostatics into a phase-field model.

In Chapter 2, I use a mean-field theory and MC simulations to study the competition of multiple counterions of different valences and different sizes in binding to the surface of a spherical colloidal particle. In the mean-field approach, I minimize a semi-phenomenological electrostatic free-energy functional of ionic concentrations constrained by Poisson’s equation. The different ionic sizes are described through the entropic contributions of ions and solvent molecules. The constrained free-energy minimization is realized numerically by an augmented Lagrange multiplier method. I also use an unrestricted primitive model and canonical ensemble MC simulations with the Metropolis criterion to predict the ionic distributions around the charged surface. Both methods correctly predict the key factor, valence-to-volume ratio, in the competition between different species of ions near the highly charged surface. While simulations have captured the charge inversion for ionic systems with salt, the mean-field theory, however, fails in predicting the charge inversion, since it does not include the ion-ion correlation.

In Chapter 3, I study a variational problem of minimizing a mean-field

electrostatic free-energy functional to investigate how the ionic concentration dependent dielectric response can affect the equilibrium properties of electrostatic interactions of an ionic solution near a charged surface. I have rigorously derived the first and second variations of the free-energy functional. From the generalized Boltzmann distributions, one can see that the ionic depletion can occur due to the high concentration low permittivity relation. The formula of the second variation of the functional indicates the functional can be nonconvex. I have indeed shown that it is so for some model systems. I have also developed a numerical method and performed computations with a three-dimensional, radially symmetric geometry for a system with a single counterion species or a system with two multi-valence counterion species. I have demonstrated that the increase of the surface charge density will lead to the non-monotonicity of concentration profiles. These results confirm experimental findings and also indicate that the classical PB theory does not capture the ionic depletion and other properties.

In Chapter 4, I have introduced the PB electrostatic free energy into the phase-field variational implicit-solvent model. The first variation of the functional can be deduced by the lemmas in Chapter 3 using similar techniques. I have designed the proper numerical schemes to find the minimizing phase field function. The key point is the dielectric function, which is specifically designed based on the first variation of the functional. I have chosen semi-implicit scheme in order to have a larger time step. I have also studied a spherical model system numerically. By minimizing the energy, I have found the surface location $\phi = 0.5$. Our result shows the convergence clearly, and each part of the free-energy functional is approaching analytical value as well. I have observed that stronger charge cause the smaller ionic radius, this indicates the importance of electrostatic interaction in determining the shape of charged object.

5.2 Discussion and Future Work

I have studied two modified mean-field model based on Poisson–Boltzmann theory with ion specific properties and self consistent environment parameter. Ac-

According to the numerical studies, both models have shown richer properties of the ionic concentration profile in charged system than the classical theory. One is also confirmed by designed Monte Carlo simulation.

In a variational approach, the ion specific properties can be incorporated into the mean-field theory. The studies of mean-field model with ionic size effect and concentration dependent dielectric have proven the advantage of this approach. Moreover, the variational energy minimizing framework is more flexible and helpful to improve the mean-field theory and apply in various systems for finding and studying the equilibriums. This is clearly demonstrated by the study of in phase-field model with PB description. More importantly, the energy minimization framework is simple and efficient and easy to implement, since the problem is reduced to solving one or two partial differential equations.

Although the modified theories provide much more insights of the charged system, some details might be still missing compared with particle-like methods. Thus, a multiscale model of mean-field theory and molecular simulation may be extremely effective for complex biological systems.

There are several future works based on my dissertation. First, it is desirable to apply the efficient theory and methods to large-scale modeling of biomolecular systems in which nonuniform ionic size effects can be sometimes very important. On the theoretical development, it is also necessary to derive from statistical mechanics theory the mean-field, electrostatic free-energy functional that includes the nonuniform ionic size effect.

Second, it is very challenging to perform Monte Carlo simulations for a system with concentration dependent dielectric response. Recently, Fahrenberger *et al.* [FXH14] have developed a Monte Carlo simulation method in space dependent dielectric system using Harmonic interpolation method. The result is confirmed with Maxwell equations molecular dynamics. The setup could be helpful to design simulation in our system. It is one of the future interests, and the goal is to verify my observation by simulation.

Regarding the phase-field work, several further theoretical studies have been made by Li and Liu [LL15], they have shown that while phase field parameter

$\xi \rightarrow 0$, the surface $\phi = 0.5$ converge to the sharp interface in this model using asymptotic analysis. I also plan to apply the model to real 3D system with protein. Furthermore, it is very interesting to add fluctuations into the phase-field model with Poisson–Boltzmann electrostatics.

Lastly, some detailed mathematical treatments of the variational approach developed in Chapter 3 still remains challenging. New analysis concepts and tools are needed.

Bibliography

- [AAN09] Z. Abbas, E. Ahlberg, and S. Nordholm. Monte Carlo simulations of salt solutions: exploring the validity of primitive models. *J. Phys. Chem. B*, 113:5905–5916, 2009.
- [ABH05] D. Antypov, M. C. Barbosa, and C. Holm. Incorporation of excluded-volume correlations into Poisson–Boltzmann theory. *Phys. Rev. E*, 71:061106, 2005.
- [ACI⁺09] R. E. Amaro, X. Cheng, I. Ivanov, D. Xu, and J. A. McCammon. Characterizing loop dynamics and ligand recognition in human- and avian-type influenza neuraminidases via generalized Born molecular dynamics and end-point free energy calculations. *J. Am. Chem. Soc.*, 131:4702–4709, 2009.
- [Ada75] R. Adams. *Sobolev Spaces*. Academic Press, New York, 1975.
- [AGV06] C. Avendaño and A. Gil-Villegas. Monte Carlo simulations of primitive models for ionic systems using the Wolf method. *Molecular Phys.*, 104:1475–1486, 2006.
- [AMW98] D. M. Anderson, G. B. McFadden, and A. A. Wheeler. Diffuse-interface methods in fluid mechanics. *Ann. Rev. Fluid Mech.*, 30:139–165, 1998.
- [And95] D. Andelman. Electrostatic properties of membranes: The Poisson–Boltzmann theory. In R. Lipowsky and E. Sackmann, editors, *Handbook of Biological Physics*, volume 1, pages 603–642. Elsevier, 1995.
- [Bak05] N. A. Baker. Improving implicit solvent simulations: a Poisson-centric view. *Curr. Opin. Struct. Biol.*, 15:137–143, 2005.
- [BAO97] I. Borukhov, D. Andelman, and H. Orland. Steric effects in electrolytes: A modified Poisson–Boltzmann equation. *Phys. Rev. Lett.*, 79:435–438, 1997.

- [BAO00] I. Borukhov, D. Andelman, and H. Orland. Adsorption of large ions from an electrolyte solution: A modified Poisson–Boltzmann equation. *Electrochimica Acta*, 46:221–229, 2000.
- [BAR80] M. L. Bleam, C. F. Anderson, and M. T. J. Record. Relative binding affinities of monovalent cations for double-stranded DNA. *Proc. Natl. Acad. Sci. USA.*, 77:3085–3089, 1980.
- [BC00] D. Bashford and D. A. Case. Generalized Born models of macromolecular solvation effects. *Ann. Rev. Phys. Chem.*, 51:129–152, 2000.
- [BD12] A. H. Boschitsch and P. V. Danilov. Formulation of a new and simple nonuniform size-modified Poisson–Boltzmann description. *J. Comput. Chem.*, 33:1152–1164, 2012.
- [Ber82] D. P. Bertsekas. *Constrained Optimization and Lagrange Multiplier Method*. Academic Press, New York, 1982.
- [BHB94] R. Buchner, G. T. Hefter, and J. Barthel. Dielectric relaxation of aqueous NaF and KF solutions. *J. Chem. Soc. Faraday Trans.*, 90:2475–2479, 1994.
- [BHM99] R. Buchner, G. T. Hefter, and P. M. May. Dielectric relaxation of aqueous NaCl solutions. *J. Phys. Chem. A*, 103:1–9, 1999.
- [Bik42] J. J. Bikerman. Structure and capacity of the electrical double layer. *Philos. Mag.*, 33:384–397, 1942.
- [BKM05] T. Biben, K. Kassner, and C. Misbah. Phase-field approach to three-dimensional vesicle dynamics. *Phys. Rev. E*, 72:041921, 2005.
- [BKN⁺05] H. Boroudjerdi, Y.-W. Kim, A. Naji, R. R. Netz, X. Schlagberger, and A. Serr. Statics and dynamics of strongly charged soft matter. *Phys. Rep.*, 416:129–199, 2005.
- [BKSA09] M. Z. Bazant, M. S. Kilic, B. D. Storey, and A. Ajdari. Towards an understanding of induced-charge electrokinetics at large applied voltages in concentrated solutions. *Adv. Colloid Interface Sci.*, 152:48–88, 2009.
- [BN80] A. Ben-Naim. *Hydrophobic Interactions*. Plenum Press, 1980.
- [BRP05] R. Benítez and L. Ramírez-Piscina. Sharp-interface projection of a fluctuating phase-field model. *Phys. Rev. E*, 71:061603, 2005.

- [BSD09] M. Baptista, R. Schmitz, and B. Dünweg. Simple and robust solver for the Poisson–Boltzmann equation. *Phys. Rev. E*, 80:016705, 2009.
- [BSK11] M. Bazant, B. D. Storey, and A. A. Kornyshev. Double-layer in ionic liquid: Overscreening versus crowding. *Phys. Rev. Lett.*, 106:046102, 2011.
- [BTC⁺07] Y. Bai, K. Travers, V. B. Chu, J. Lipfert, S. Doniach, and D. Herschlag. Quantitative and comprehensive decomposition of the ion atmosphere around nucleic acids. *J. Amer. Chem. Soc.*, 129:14981–14988, 2007.
- [BV92] M. Bešter and V. Vlachy. Monte Carlo study of mixed electrolytes in the primitive model. *J. Chem. Phys.*, 96:7656–7661, 1992.
- [BWBK02] W. J. Boettinger, J. A. Warren, C. Beckermann, and A. Karma. Phase-field simulation of solidification. *Annu. Rev. Materials Res.*, 32:163–194, 2002.
- [BWZ09] B. J. Berne, J. D. Weeks, and R. Zhou. Dewetting and hydrophobic interaction in physical and biological systems. *Annu. Rev. Phys. Chem.*, 60:85–103, 2009.
- [BYAHP09] D. Ben-Yaakov, D. Andelman, D. Harries, and R. Podgornik. Beyond standard Poisson–Boltzmann theory: Ion-specific interactions in aqueous solutions. *J. Phys.: Condens. Matter*, 21:424106, 2009.
- [BYAP11] D. Ben-Yaakov, D. Andelman, and R. Podgornik. Dielectric decrement as a source of ion-specific effects. *J. Chem. Phys.*, 134:074705, 2011.
- [CB07] J. Chen and C. L. Brooks III. Critical importance of length-scale dependence in implicit modeling of hydrophobic interactions. *J. Amer. Chem. Soc.*, 129:2444, 2007.
- [CBL⁺07] V. B. Chu, Y. Bai, J. Lipfert, D. Herschlag, and S. Doniach. Evaluation of ion binding to DNA duplexes using a size-modified Poisson–Boltzmann theory. *Biophys. J.*, 93:3202–3209, 2007.
- [CCL11] H.-B. Cheng, L.-T. Cheng, and B. Li. Yukawa-field approximation of electrostatic free energy and dielectric boundary force. *Nonlinearity*, 24:3215–3235, 2011.

- [CDLM08] J. Che, J. Dzubiella, B. Li, and J. A. McCammon. Electrostatic free energy and its variations in implicit solvent models. *J. Phys. Chem. B*, 112:3058–3069, 2008.
- [CDML07] L.-T. Cheng, J. Dzubiella, J. A. McCammon, and B. Li. Application of the level-set method to the implicit solvation of nonpolar molecules. *J. Chem. Phys.*, 127:084503, 2007.
- [Cha13] D. L. Chapman. A contribution to the theory of electrocapillarity. *Philos. Mag.*, 25:475–481, 1913.
- [Cha05] D. Chandler. Interfaces and the driving force of hydrophobic assembly. *Nature*, 437:640–647, 2005.
- [Che02] L.-Q. Chen. Phase-field models of microstructure evolution. *Annu. Rev. Materials Res.*, 32:113–140, 2002.
- [CL85] J. B. Collins and H. Levine. Diffuse interface model of diffusion-limited crystal growth. *Phys. Rev. B*, 31:6119–6122, 1985.
- [CLW10] L.-T. Cheng, B. Li, and Z. Wang. Level-set minimization of potential controlled Hadwiger valuations for molecular solvation. *J. Comput. Phys.*, 229:8497–8510, 2010.
- [Con83] M. L. Connolly. Analytical molecular surface calculation. *J. Appl. Cryst.*, 16:548–558, 1983.
- [Con92] M. L. Connolly. The molecular surface package. *J. Mol. Graphics*, 11:139–141, 1992.
- [Con99] B. E. Conway. *Electrochemical Supercapacitors: Scientific Fundamentals and Technological Applications*. Kluwer Academic/Plenum Publishers, New York, 1999.
- [CT99] C. J. Cramer and D. G. Truhlar. Implicit solvation models: Equilibria, structure, spectra, and dynamics. *Chem. Rev.*, 99:2161–2200, 1999.
- [CWS⁺09] L.-T. Cheng, Z. Wang, P. Setny, J. Dzubiella, B. Li, and J. A. McCammon. Interfaces and hydrophobic interactions in receptor-ligand systems: A level-set variational implicit solvent approach. *J. Chem. Phys.*, 131:144102, 2009.
- [CXD⁺09] L.-T. Cheng, Y. Xie, J. Dzubiella, J. A. McCammon, J. Che, and B. Li. Coupling the level-set method with molecular mechanics for variational implicit solvation of nonpolar molecules. *J. Chem. Theory Comput.*, 5:257–266, 2009.

- [DDP12] V. Démery, D. S. Dean, and R. Podgornik. Electrostatic interactions mediated by polarizable counterions: Weak and strong coupling limits. *J. Chem. Phys.*, 137:174903, 2012.
- [DH23] P. Debye and E. Hückel. The theory of electrolytes. I. Lowering of freezing point and related phenomena. *Phys. Zeitschr.*, 24:185–206, 1923.
- [Dil90] K. A. Dill. Dominant forces in protein folding. *Biochemistry*, 29:7133–7155, 1990.
- [DLRW05] Q. Du, C. Liu, R. Ryham, and X. Wang. A phase field formulation of the Willmore problem. *Nonlinearity*, 18:1249–1267, 2005.
- [DLW04] Q. Du, C. Liu, and X. Wang. A phase field approach in the numerical study of the elastic bending energy for vesicle membranes. *J. Comput. Phys.*, 198:450–468, 2004.
- [DM90] M. E. Davis and J. A. McCammon. Electrostatics in biomolecular structure and dynamics. *Chem. Rev.*, 90:509–521, 1990.
- [DN84] P. Drude and W. Nernst. Über Elektrostriktion durch freie Ionen. *Z. Phys. Chem.*, 15:79–85, 1984.
- [DSM06a] J. Dzubiella, J. M. J. Swanson, and J. A. McCammon. Coupling hydrophobicity, dispersion, and electrostatics in continuum solvent models. *Phys. Rev. Lett.*, 96:087802, 2006.
- [DSM06b] J. Dzubiella, J. M. J. Swanson, and J. A. McCammon. Coupling nonpolar and polar solvation free energies in implicit solvent models. *J. Chem. Phys.*, 124:084905, 2006.
- [EHL10] B. Eisenberg, Y.-K. Hyon, and C. Liu. Energy variational analysis of ions in water and channels: Field theory for primitive models of complex ionic fluids. *J. Chem. Phys.*, 133:104104, 2010.
- [Eis11] B. Eisenberg. Crowded charges in ion channels. In S. A. Rice and A. R. Dinner, editors, *Adv. Chem. Phys.*, volume 148, pages 77–223, 2011.
- [Emm03] H. Emmerich. *The Diffuse Interface Approach in Materials Science: Thermodynamic Concepts and Applications of Phase-Field Models*. Springer, Berlin and Heidelberg, 2003.
- [Eva10] L. C. Evans. *Partial Differential Equations*, volume 19 of *Graduate Studies in Mathematics*. Amer. Math. Soc., 2nd edition, 2010.

- [EW54] M. Eigen and E. Wicke. The thermodynamics of electrolytes at higher concentration. *J. Phys. Chem.*, 58:702–714, 1954.
- [FB97] F. Fogolari and J. M. Briggs. On the variational approach to Poisson–Boltzmann free energies. *Chem. Phys. Lett.*, 281:135–139, 1997.
- [FBM02] F. Fogolari, A. Brigo, and H. Molinari. The Poisson–Boltzmann equation for biomolecular electrostatics: A tool for structural biology. *J. Mol. Recognit.*, 15:377–392, 2002.
- [FI04] M. Feig and C. L. Brooks III. Recent advances in the development and applications of implicit solvent models in biomolecule simulations. *Current Opinion in Structure Biology*, 14:217–224, 2004.
- [Fix79] F. Fixman. The Poisson–Boltzmann equation and its application to polyelectrolytes. *J. Chem. Phys.*, 70:4995–5005, 1979.
- [FPP⁺10] R. H. French, V. A. Parsegian, R. Podgornik, R. F. Rajter, A. Jagota, J. Luo, D. Asthagiri, M. K. Chaudhury, Y.-M. Chiang, S. Granick, S. Kalinin, M. Kardar, R. Kjellander, D. C. Langreth, J. Lewis, S. Lustig, D. Wesolowski, J. S. Wettlaufer, W.-Y. Ching, M. Finnis, F. Houlihan, O. A. von Lilienfeld, C. J. van Oss, and T. Zemb. Long range interactions in nanoscale science. *Rev. Mod. Phys.*, 82(2):1887–1944, 2010.
- [Fry11] D. Frydel. Polarizable Poisson–Boltzmann equation: The study of polarizability effects on the structure of a double layer. *J. Chem. Phys.*, 134:234704, 2011.
- [FS02] D. Frenkel and B. Smit. *Understanding molecular simulation: From algorithms to applications*. Academic Press, New York, 2002.
- [FXH14] Florian Fahrenberger, Zhenli Xu, and Christian Holm. Simulation of electric double layers around charged colloids in aqueous solution of variable permittivity. *J. Chem. Phys.*, 141:064902, 2014.
- [GGGTd11] G. I. Guerrero-Garcia, E. Gonzalez-Tovar, and M. O. de la Cruz. Entropic effects in the electric double layer of model colloids with size-asymmetric monovalent ions. *J. Chem. Phys.*, 135:054701, 2011.

- [GGHW65] G. H. Gilmer, W. Gilmore, J. Huang, and W. W. Webb. Diffuse interface in a critical fluid mixture. *Phys. Rev. Lett.*, 14:491–494, 1965.
- [Gla03] K. Glasner. A diffuse interface approach to Hele-Shaw flow. *Nonlinearity*, 16:49–66, 2003.
- [GLD⁺14] Z. Guo, B. Li, J. Dzubiella, L.-T. Cheng, J. A. McCammon, and J. Che. Heterogeneous hydration of p53/MDM2 complex. *J. Chem. Theory Comput.*, 10:1302–1313, 2014.
- [GNS02] A. Y. Grosberg, T. T. Nguyen, and B. I. Shklovskii. Colloquium: The physics of charge inversion in chemical and biological systems. *Rev. Mod. Phys.*, 74:329–345, 2002.
- [Gou10] G. Gouy. Constitution of the electric charge at the surface of an electrolyte. *J. Phys.*, 9:457–468, 1910.
- [GT98] D. Gilbarg and N. S. Trudinger. *Elliptic Partial Differential Equations of Second Order*. Springer-Verlag, 2nd edition, 1998.
- [GT08] P. Grochowski and J. Trylska. Continuum molecular electrostatics, salt effects and counterion binding—A review of the Poisson-Boltzmann model and its modifications. *Biopolymers*, 89:93–113, 2008.
- [Has73] J. B. Hasted. *Aqueous Dielectrics*. Chapman and Hall, London, 1973.
- [Hil01] B. Hille. *Ion Channels of Excitable Membranes*. Sinauer Associates, 3rd edition, 2001.
- [HPP10] J. J. Howard, J. S. Perkyns, and B. M. Pettitt. The behavior of ions near a charged wall—dependence on ion size, concentration, and surface charge. *J. Phys. Chem. B*, 114:6074–6083, 2010.
- [HRC48] J. B. Hasted, D. M. Riston, and C. H. Collie. Dielectric properties of aqueous ionic solutions. Parts I and II. *J. Chem. Phys.*, 16:1–21, 1948.
- [Jac99] J. D. Jackson. *Classical Electrodynamics*. Wiley, New York, 3rd edition, 1999.
- [KBA07a] M. S. Kilic, M. Z. Bazant, and A. Ajdari. Steric effects in the dynamics of electrolytes at large applied voltages. I. Double-layer charging. *Phys. Rev. E*, 75:021502, 2007.

- [KBA07b] M. S. Kilic, M. Z. Bazant, and A. Ajdari. Steric effects in the dynamics of electrolytes at large applied voltages. II. Modified Poisson–Nernst–Planck equations. *Phys. Rev. E*, 75:021503, 2007.
- [KD09] I. Kalcher and J. Dzubiella. Structure-thermodynamics relation of electrolyte solutions. *J. Chem. Phys.*, 130:134507, 2009.
- [Kie37] J. Kielland. Individual activity coefficients of ions in aqueous solutions. *J. Am. Chem. Soc.*, 59:1675–1678, 1937.
- [KII96] V. Kralj-Iglič and A. Iglič. A simple statistical mechanical approach to the free energy of the electric double layer including the excluded volume effect. *J. Phys. II (France)*, 6:477–491, 1996.
- [KKL01] A. Karma, D. Kessler, and H. Levine. Phase-field model of mode III dynamic fracture. *Phys. Rev. Lett.*, 87:045501, 2001.
- [Kor07] A. A. Kornyshev. Double-layer in ionic liquids: Paradigm change? *J. Phys. Chem. B*, 111:5545–5557, 2007.
- [KR99] A. Karma and W. J. Rappel. Phase-field model of dendritic side-branching with thermal noise. *Phys. Rev. E*, 60:3614–3625, 1999.
- [KSD11] I. Kalcher, J. C. F. Schulz, and J. Dzubiella. Electrolytes in a nanometer slab-confinement: Ion-specific structure and solvation forces. *J. Chem. Phys.*, 133:164511, 2011.
- [KZC⁺13] Y. Kwan, Y. Zhao, J. Che, B. Li, and J. A. McCammon. Phase-field approach to implicit solvation of biomolecules with coulomb-field approximation. *J. Chem. Phys.*, 139:024111, 2013.
- [Lan86] J. S. Langer. Models of pattern formation in first-order phase transitions. In G. Grinstein and G. Mazenko, editors, *Directions in Condensed Matter Physics*. World Scientific, 1986.
- [LAO12] A. Levy, D. Andelman, and H. Orland. Dielectric constant of ionic solutions: A field-theory approach. *Phys. Rev. Lett.*, 108:227801, 2012.
- [Lat21] R. T. Lattey. The dielectric constants of electrolytic solutions. *Philos. Mag.*, 41:829–848, 1921.
- [LCW99] K. Lum, D. Chandler, and J. D. Weeks. Hydrophobicity at small and large length scales. *J. Phys. Chem. B*, 103:4570–4577, 1999.
- [Lev02] Y. Levin. Electrostatic corrections: From plasma to biology. *Rep. Prog. Phys.*, 65:1577–1632, 2002.

- [Li09a] B. Li. Continuum electrostatics for ionic solutions with nonuniform ionic sizes. *Nonlinearity*, 22:811–833, 2009.
- [Li09b] B. Li. Minimization of electrostatic free energy and the Poisson–Boltzmann equation for molecular solvation with implicit solvent. *SIAM J. Math. Anal.*, 40:2536–2566, 2009.
- [LL14] H. Li and B. Lu. An ionic concentration and size dependent dielectric permittivity Poisson–Boltzmann model for biomolecular solvation studies. *J. Chem. Phys.*, 141:024115, 2014.
- [LL15] B. Li and Y. Liu. Diffused solute-solvent interface with poisson-boltzmann electrostatics: Free-energy variation and sharp-interface limit. *SIAM J. Applied Math*, 2015.
- [LLP93] L. D. Landau, E. M. Lifshitz, and L. P. Pitaevski. *Electrodynamics of Continuous Media*. Butterworth-Heinemann, 2nd edition, 1993.
- [LLSD09] D. Lambert, D. Leipply, R. Shiman, and D. E. Draper. The influence of monovalent cation size on the stability of RNA tertiary structures. *J. Mol Biol.*, 390:791–804, 2009.
- [LLXZ13] B. Li, P. Liu, Z. Xu, and S. Zhou. Ionic size effects: generalized boltzmann distributions, counterion stratification, and modified debye length. *Nonlinearity*, 26:2899–2922, 2013.
- [LO06] Y. Levy and J. N. Onuchic. Water mediation in protein folding and molecular recognition. *Annu. Rev. Biophys. Biomol. Struct.*, 35:389–415, 2006.
- [LR71] B. Lee and F. M. Richards. The interpretation of protein structures: Estimation of static accessibility. *J. Mol. Biol.*, 55:379–400, 1971.
- [LRV09] J. S. Lowengrub, A. Rätz, and A. Voigt. Phase-field modeling of the dynamics of multicomponent vesicles: Spinodal decomposition, coarsening, budding, and fission. *Phys. Rev. E*, 79:031926, 2009.
- [LZ98] A. K. Lyashchenko and A. Yu. Zasesky. Complex dielectric permittivity and relaxation parameters of concentrated aqueous electrolyte solutions in millimeter and centimeter wavelength ranges. *J. Molecular Liquids*, 77:61–75, 1998.

- [LZ11] B. Lu and Y. Zhou. Poisson–Nernst–Planck equations for simulating biomolecular diffusion-reaction processes II: Size effects on ionic distributions and diffusion-reaction rates. *Biophys. J.*, 100:2475–2485, 2011.
- [LZ13] B. Li and Y. Zhao. Variational implicit solvation with solute molecular mechanics: From diffuse-interface to sharp-interface models. *SIAM J. Applied Math.*, 73:1–23, 2013.
- [LZHM08] B. Z. Lu, Y. C. Zhou, M. J. Holst, and J. A. McCammon. Recent progress in numerical methods for the Poisson–Boltzmann equation in biophysical applications. *Commun. Comput. Phys.*, 3:973–1009, 2008.
- [McC09] J. A. McCammon. Darwinian biophysics: Electrostatics and evolution in the kinetics of molecular binding. *Proc. Nat. Acad. Sci. USA*, 106:7683–7684, 2009.
- [Mod87] L. Modica. The gradient theory of phase transitions and the minimal interface criterion. *Arch. Rational Mech. Anal.*, 98:123–142, 1987.
- [MR02] A. C. Maggs and V. Rossetto. Local simulation algorithms for Coulomb interactions. *Phys. Rev. Lett.*, 88:196402, 2002.
- [MRR⁺53] N. Metropolis, A. W. Rosenbluth, M. N. Rosenbluth, A. H. Teller, and E. Teller. Equation of state calculations by fast computing machines. *J. Chem. Phys.*, 21:1087–1092, 1953.
- [MX14] M. Ma and Z. Xu. Self-consistent field model for strong electrostatic correlations and inhomogeneous dielectric media. *J. Chem. Phys.*, 141:244903, 2014.
- [NHK97] K. Nörtemann, J. Hilland, and U. Kaatze. Dielectric properties of aqueous NaCl solutions at microwave frequencies. *J. Phys. Chem. A*, 101:6864–6869, 1997.
- [NW99] J. Nocedal and S. Wright. *Numerical Optimization*. Springer-Verlag, New York, 1999.
- [ODRY09] O. I. Obolensky, T. P. Doerr, R. Ray, and Y.-K. Yu. Rigorous treatment of electrostatics for spatially varying dielectrics based on energy minimization. *Phys. Rev. E*, 79:041907, 2009.
- [QPGTMM⁺03] M. Quesada-Pérez, E. González-Tovar, A. Martín-Molina, M. Lozada-Cassou, and R. Hidalgo-Álvarez. Overcharging in colloids: Beyond the Poisson–Boltzmann approach. *Chem. Phys. Chem.*, 4:234–248, 2003.

- [QPMMHÁ04] M. Quesada-Pérez, A. Martín-Molina, and R. Hidalgo-Álvarez. Simulation of electric double layers with multivalent counterions: Ion size effect. *J. Chem. Phys.*, 121:8618–8626, 2004.
- [RDZ⁺14] R. Renou, M. Ding, H. Zhu, A. Szymczyk, P. Malfreyt, and A. Ghoufi. Concentration dependence of the dielectric permittivity, structure, and dynamics of aqueous NaCl solutions: Comparison between the Drude oscillator and electronic continuum models. *J. Phys. Chem. B*, 118:3931–3940, 2014.
- [RHK06] R. Roth, Y. Harano, and M. Kinoshita. Morphometric approach to the solvation free energy of complex molecules. *Phys. Rev. Lett.*, 97:078101, 2006.
- [Ric77] F. M. Richards. Areas, volumes, packing, and protein structure. *Annu. Rev. Biophys. Bioeng.*, 6:151–176, 1977.
- [Ric84] T. J. Richmond. Solvent accessible surface area and excluded volume in proteins. Analytical equations for overlapping spheres and implications for the hydrophobic effect. *J. Mol. Biol.*, 178:63–89, 1984.
- [RR90] E. S. Reiner and C. J. Radke. Variational approach to the electrostatic free energy in charged colloidal suspensions: General theory for open systems. *J. Chem. Soc. Faraday Trans.*, 86:3901–3912, 1990.
- [RS99] B. Roux and T. Simonson. Implicit solvent models. *Biophys. Chem.*, 78:1–20, 1999.
- [SBHF10] A. R. J. Silalahi, A. H. Boschitsch, R. C. Harris, and M. O. Fenley. Comparing the predictions of the nonlinear Poisson–Boltzmann equation and the ion size-modified Poisson–Boltzmann equation for a low-dielectric charged spherical cavity in an aqueous salt solution. *J. Chem. Theory Comput.*, 6:3631–3639, 2010.
- [Sch27] C. C. Schmidt. The dielectric constants of four electrolytes as given by the Carman electrometer method. *Phys. Rev.*, 30:925–930, 1927.
- [SGM10] J. Sala, E. Guàdia, and J. Marti. Effects of concentration on structure, dielectric, and dynamic properties of aqueous NaCl solutions using a polarizable model. *J. Chem. Phys.*, 132:214505, 2010.

- [SH90a] K. A. Sharp and B. Honig. Calculating total electrostatic energies with the nonlinear Poisson–Boltzmann equation. *J. Phys. Chem.*, 94:7684–7692, 1990.
- [SH90b] K. A. Sharp and B. Honig. Electrostatic interactions in macromolecules: Theory and applications. *Annu. Rev. Biophys. Biophys. Chem.*, 19:301–332, 1990.
- [SNH00] F. B. Sheinerman, R. Norel, and B. Honig. Electrostatic aspects of protein-protein interactions. *Curr. Opin. Struct. Biology*, 10:153–159, 2000.
- [SRL10] D. Shao, W.-J. Rappel, and H. Levine. Computational model for cell morphodynamics. *Phys. Rev. Lett.*, 105:108104, 2010.
- [Ste88] P. Sternberg. The effect of a singular perturbation on nonconvex variational problems. *Arch. Rational Mech. Anal.*, 101:209–260, 1988.
- [STHH90] W. C. Still, A. Tempczyk, R. C. Hawley, and T. Hendrickson. Semianalytical treatment of solvation for molecular mechanics and dynamics. *J. Amer. Chem. Soc.*, 112:6127–6129, 1990.
- [SWC⁺09] P. Setny, Z. Wang, L.-T. Cheng, B. Li, J. A. McCammon, and J. Dzubiella. Dewetting-controlled binding of ligands to hydrophobic pockets. *Phys. Rev. Lett.*, 103:187801, 2009.
- [Tan80] C. Tanford. *The Hydrophobic Effect: Formation of Micells and Biological Membranes*. John Wiley & Sons, 1980.
- [TCC06] M. Tang, W. C. Carter, and R. M. Cannon. Diffuse interface model for structural transitions of grain boundaries. *Phys. Rev. B*, 73:024102, 2006.
- [TP94] J. Tomasi and M. Persico. Molecular interactions in solution: An overview of methods based on continuous distributions of the solvent. *Chem. Rev.*, 94:2027–2094, 1994.
- [Tre08] G. Tresset. Generalized Poisson–Fermi formalism for investigating size correlation effects with multiple ions. *Phys. Rev. E*, 78:061506, 2008.
- [TSYT05] P. Taboada-Serrano, S. Yiacoumi, and C. Tsouris. Behavior of mixtures of symmetric and asymmetric electrolytes near discretely charged planar surfaces: A Monte Carlo study. *J. Chem. Phys.*, 123:054703, 2005.

- [TVTWO6] A. Tulpar, P. R. Van Tassel, and J. Y. Walz. Structuring of macroions confined between like-charged surfaces. *Langmuir*, 22(6):2876–2883, 2006.
- [VBG07] M. Valiskó, D. Boda, and D. Gillespie. Selective adsorption of ions with different diameter and valence and highly charged interfaces. *J. Phys. Chem. C*, 111:15575–15585, 2007.
- [VC80] J. P. Valleau and L. K. Cohen. Primitive model electrolytes. I. Grand canonical Monte Carlo computations. *J. Chem. Phys.*, 72:5935–5941, 1980.
- [VvdVM01] M. Verschueren, F. N. van de Vosse, and H. E. H. Meijer. Diffuse-interface modeling of thermocapillary flow instabilities in a Hele-Shaw cell. *J. Fluid Mech.*, 434:153–166, 2001.
- [Wan10] Z.-G. Wang. Fluctuation in electrolyte solutions: The self energy. *Phys. Rev. E*, 81:021501, 2010.
- [WCC⁺12] Z. Wang, J. Che, L.-T. Cheng, J. Dzubiella, B. Li, and J. A. McCammon. Level-set variational implicit-solvent modeling of biomolecules with the Coulomb-field approximation. *J. Chem. Theory Comput.*, 8:386–397, 2012.
- [WCS92] Y.-Z. Wei, P. Chiang, and S. Sridhar. Ion size effects on the dynamic and static dielectric properties of aqueous alkali solutions. *J. Chem. Phys.*, 96:4569–4573, 1992.
- [WFB10] L. Wang, R. A. Friesner, and B. J. Berne. Hydrophobic interactions in model enclosures from small to large length scales: Non-additivity in explicit and implicit solvent models. *Faraday Disc.*, 146:247–262, 2010.
- [WKBL11] J. Wang, S. Kudesia, D. Bratko, and A. Luzar. Computational probe of cavitation events in protein systems. *Phys. Chem. Chem. Phys.*, 13:19902–19910, 2011.
- [WS90] Y. Wei and S. Sridhar. Dielectric spectroscopy up to 20 GHz of LiCl/H₂O solutions. *J. Chem. Phys.*, 92:923–926, 1990.
- [WYGL05] K. Wang, Y.-X. Yu, G.-H. Gao, and G.-S. Luo. Density-functional theory and Monte Carlo simulation study on the electric double layer around DNA in mixed-size counterion systems. *J. Chem. Phys.*, 123:234904, 2005.

- [WZXL12] J. Wen, S. Zhou, Z. Xu, and B. Li. Competitive adsorption and ordered packing of counterions near highly charged surfaces: From mean-field theory to Monte Carlo simulations. *Phys. Rev. E*, 85:041406, 2012.
- [XML14] Z. Xu, M. Ma, and P. Liu. Self-energy modified Poisson–Nernst–Planck equations: WKB approximation and finite-difference approaches. *Phys. Rev. E*, 90:013307, 2014.
- [YFLS04] P. Yue, J. J. Feng, C. Liu, and J. Shen. A diffuse-interface method for simulating two-phase flows of complex fluids. *J. Fluid Mech.*, 515:293–317, 2004.
- [ZCD⁺14] S. Zhou, L.-T. Cheng, J. Dzubiella, B. Li, and J. A. McCammon. Variational implicit solvation with Poisson–Boltzmann theory. *J. Chem. Theory Comput.*, 10(4):1454–1467, 2014.
- [ZHMB04] R. Zhou, X. Huang, C. J. Margulis, and B. J. Berne. Hydrophobic collapse in multidomain protein folding. *Science*, 305:1605–1609, 2004.
- [ZWL11] S. Zhou, Z. Wang, and B. Li. Mean-field description of ionic size effects with non-uniform ionic sizes: A numerical approach. *Phys. Rev. E*, 84:021901, 2011.